Crack-based evaluation of deep concrete members with FRP bars

Auteur : Ernens, Glenn
Promoteur(s) : Mihaylov, Boyan
Faculté : Faculté des Sciences appliquées
Diplôme : Master en ingénieur civil des constructions, à finalité spécialisée en "civil engineering"
Année académique : 2021-2022
URI/URL : http://hdl.handle.net/2268.2/14595

University of Liège
School of Engineering and Computer Science

Crack-based evaluation of deep concrete members reinforced with FRP bars

Master's thesis carried out to obtain the degree of Master of Science in Civil Engineering

By Glenn Ernens

Supervisor
Boyan Mihaylov

Jury Members
Boyan Mihaylov
Jean-Marc Franssen
Jean-Pierre Jaspart
Giorgio Proestos

Academic year 2021-2022

Abstract

Conventional steel-reinforced concrete deep beams are typically known for their high shear strength and stiffness. To avoid corrosion-related deterioration problems, fiber-reinforced polymers (FRPs) reinforcement bars have been used as non-corrosive substitute for steel. However, tests on deep beams reinforced with internal FRP reinforcement have shown that such members can exhibit different failure modes than the ones observed in conventional deep beams. Moreover, these failure modes may limit the shear capacity making the technical solution less feasible. This study proposes to develop a kinematics-based model capable of predicting the complete shear behavior of FRP-reinforced deep beams without web reinforcement. The approach includes modelling features for three different failure modes, accounting for the effects of FRP reinforcement on the observed behavior of deep beams. The crack-based 2PKT for FRP-reinforced deep beams is applied to tests from the literature resulting in an average experimental-to-predicted strength ratio of 1.06 and a coefficient of variation of 8.5%. Furthermore, the developed kinematics-based model is able to adequately predict the failure mode, as well as global and local deformations along critical cracks.

Acknowledgement

This master's thesis is carried out to obtain the degree of Master of Science in Civil Engineering at the University of Liège. Prior to the study, I would like to thank everyone who helped me to accomplish this work.

First, I would like to express my deepest gratitude to my supervisor, Professor Boyan Mihaylov, for his support, advice and guidance throughout this thesis. His great passion for concrete structures easily convinced me to choose one of his master's thesis subjects, but, it was his undeniable capability of being an excellent professor and researcher which helped me to successfully complete this work.

I am also thankful to Alexandru Trandafir who was always available to help me and to provide feedback and helpful comments during the research and the writing phase. His wide-ranging knowledge about concrete surprised me many times. I have learned a lot from his way of thinking and tackling problems.

Many thanks to my teachers and colleagues who were there for me during the last two years.

Last but not least, I am thankful to Stien, my parents, my brother and my friends for being morally supportive and encouraging me throughout my studies.

Contents

List of Figures

List of Tables

1 Introduction

1.1 Concrete deep beams

Concrete deep beams, typically recognized by their small shear span-to-depth ratio ($a/d \leq 2.5$), have a high stiffness and shear strength. Therefore, this type of concrete element is very useful at places where high loads need to be resisted such as in transfer girders or foundation elements. Transfer girders are used in many buildings, because they give the opportunity to create a large free space without the need of columns as shown in Fig. 1.1. The advantage of deep beams to carry heavy loads immediately implies a potential risk: a failure of one deep beam can have local consequences, but, in worst case, it can even lead to a global collapse of the building. This is why research on the behavior of these concrete elements is very important.

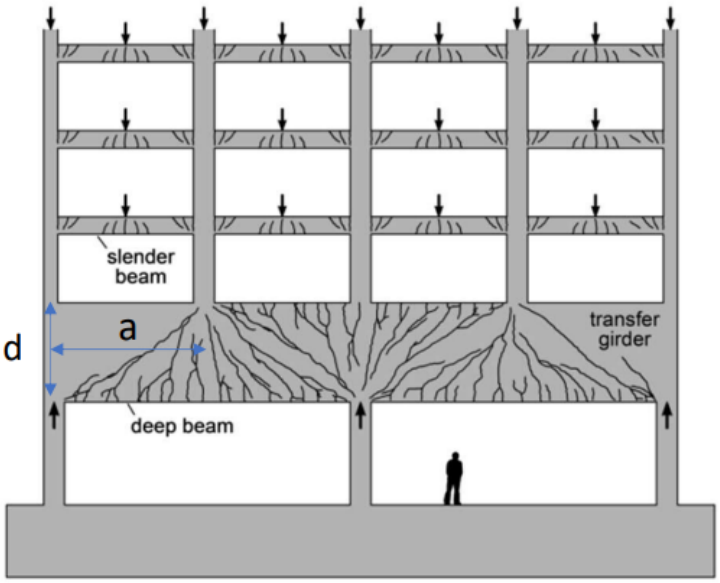

Figure 1.1: Deep transfer girders used to create a column-free area (adapted from [1])

In contrast with slender beams ($a/d > 2.5$), deep beams do not obey the hypothesis demonstrated by Hooke in 1678 [2] which states that plane sections before loading remain plane during loading due to linear distribution of the strains. This implies that deep beams do not longer carry shear like slender beams and, therefore, can not be assessed based on the classical beam theory. The behavior of deep beams can be described by arch action where compressive stresses flow in the concrete from loading plates directly to the supports [3]. Due to the fact that concrete has a very high compression capacity, deep beams can resist much higher shear forces in comparison to slender beams. This flow of compressive stresses can be compared with an arch inside the deep beam. To obtain equilibrium, the legs of the arch are kept together by a tie with a constant tensile force along the shear span. The role of the tie is fulfilled by the longitudinal flexural reinforcement of the deep beam. Because of this particular behavior, the ACI [4] and CSA [5] code recommend to use strut-and-tie models (STMs) for the design of deep beams. Nevertheless that this model has proven to be very powerful to calculate all kinds of reinforced concrete elements, it is not always capable to take into account the subtle influence of some parameters which influence the shear capacity of deep beams. Research has shown that the shear capacity of a deep beam can not only increase by decreasing the a/d ratio or by increasing the concrete strength, but the capacity depends also on the randomness of the crack geometry and, especially, the path of the diagonal shear crack. A difference in capacity, even up to 60%,

has been observed for nominally identical deep beams where the only difference was the crack geometry [1, 6, 7]. That is why the use of a model which uses the crack as an input, to predict the shear strength and failure mode with less scatter, is desired.

Generally, reinforced concrete members, such as deep beams, are associated with conventional steel reinforcement. During the last century, many reinforced concrete structures have been built and a considerable amount of research programs have been dedicated to this subject to understand the behavior of such structures. Both in practice as in research, there is observed that one of the major problems of steel reinforcement is its susceptibility to corrosion and all kind of damaging consequences that are related to it, especially in environments with a high risk of corrosion. To solve this problem, different kind of solutions have been researched. One of them, is to replace the conventional steel reinforcement by a non-corrosive reinforcement bar made out of fiber-reinforced polymers (FRPs) as shown in Fig. 1.2. This new material is characterized by its high tensile strength, but low stiffness in comparison to steel. However, the most critical parameter of FRP is settled in its behavior: brittle-elastic. Unlike steel reinforcement, the FRP bars can not yield and will not attribute plasticity to the reinforced concrete element, which results in a very different behavior and so a different modelling approach. Despite the fact that this type of reinforcement has already been used and is still used as a possible substitute for steel in risky environments, there is a lack of rules which comes together with a lack of research, especially for FRP-reinforced deep beams.

Figure 1.2: FRP bars [8]

In the structural design codes, the classic strut-and-tie model is still suggested to calculate FRP-reinforced deep beams. As mentioned earlier, one of the weaknesses of this model is that it does not include the crack geometry. Another important deficiency of the STM is that it does not take into account the different behavior of FRP-reinforced deep beams. In test programs, there has been observed that very large crack widths, up to 7 mm, had developed in deep beams reinforced with FRP bars due to the low stiffness of this type of reinforcement. More importantly, other failure modes had occurred in comparison to steel-reinforced deep beams [9] as shown in Fig. 1.3. The consequence of exhibiting another failure mode was a decrease of the shear capacity. Currently, these failure modes are not taken into account in any existing model.

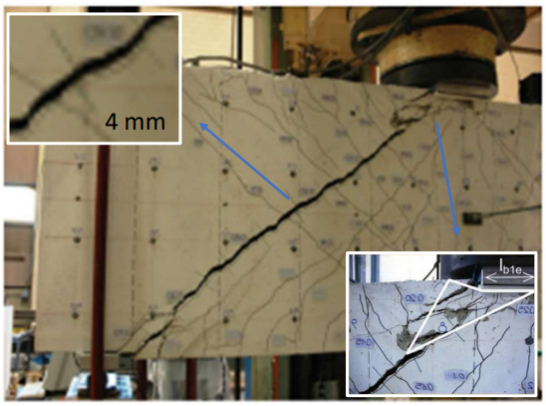

(a) Failure in a steel-reinforced deep beam [1]

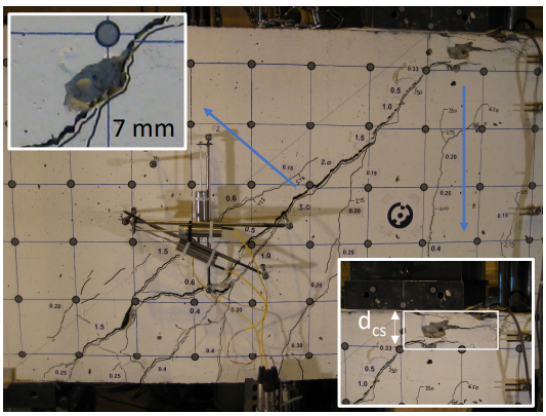

(b) Failure in a FRP-reinforced deep beam (courtesy by Andermatt and Lubell, University of Alberta)

Figure 1.3: Similar deep beams which exhibit a different failure mode and different crack widths

1.2 Research motivation

Deep beams are widely used in the construction domain. These steel-reinforced concrete elements have already been researched extensively in multiple research programs throughout the past. However, the predicted shear capacity of a steel-reinforced deep beam shows varying results depending on the model that has been used [10]. In the last decade, a new kinematics-based model, the two-parameter kinematic theory (2PKT) [11], has been developed by Mihaylov et al. which showed accurate and consistent predictions. Afterwards, this model was even extended by Trandafir et al. [12] by introducing the crack geometry as an input parameter to evaluate the capacity of an existing deep beam. However, this model is only applicable for conventional steel-reinforced deep beams.

In the past, there have been detected a lot of problems in reinforced concrete elements due to corrosion of the steel bars. To solve this problem, the steel reinforcement was replaced by non-corrosive FRP bars. Even up to this day, FRP bars are still used as a replacement for steel in deep beams. However, the behavior of these bars is not perfectly similar to the behavior of steel bars. Only a few research programs have been performed to test the behavior of FRP-reinforced deep beams. There has been seen that a different behavior and different failure modes than in steel-reinforced deep beams could occur.

It can be stated that the development of a model is necessary to have a better understanding of the behavior and the exhibiting failure modes, and to obtain improved predictions of the shear capacity of FRP-reinforced deep beams. This study proposes to develop such a model. The model is founded on the crack-based 2PKT [12], but is modified and extended to be applicable for FRP-reinforced deep beams. In other words, the approach includes modelling features for three different failure modes, accounting for the effects of FRP reinforcement on the observed behavior of deep beams.

1.3 Objectives and Scope

The objective of this master's thesis is to develop a model, based on the crack-based 2PKT [12], to assess the complete behavior and the failure mode of FRP-reinforced concrete deep beams.

The main goal of this study is to extend and modify an existing model for conventional steel-

reinforced deep beams and make it applicable for FRP-reinforced deep beams. Such members exhibit different failure modes compared to conventional deep beams, and therefore enhanced modelling approaches are deemed necessary to account for different failure modes observed in FRP-reinforced deep beams. These models need to be implemented within the existing kinematics-based framework such that the extended model can be used not only to correctly predict the failure mode and shear strength, but also to calculate the full load-displacement response, including strains in the FRP reinforcement and local deformations along critical cracks. The developed model is validated by comparing predictions with experimental results of sixteen different tests on FRP-reinforced deep beams found in the literature. Furthermore, in-depth investigations related to the effects of test variables on the shear behavior of FRP-reinforced deep beams, as well as evaluation of different modelling assumptions, are conducted in this thesis. Only deep beams with internal FRP reinforcement and without web reinforcement are considered and used to develop the model.

The objectives of the study are summarized as follows:

- to analyse test data and transform them into useful knowledge about the behavior of FRP-reinforced deep beams;
- to extend the existing crack-based 2PKT to account for the behavior of FRP reinforcement;
- to model observed failure modes that are not considered currently in the kinematic framework;
- to validate the predicted shear behavior of FRP-reinforced deep beams in terms of both strength and deformations, at local and global level;
- to investigate the effects of test variables on the shear behavior of FRP-reinforced deep beams.

1.4 Thesis outline

This thesis presents five chapters with the introduction included.

Chapter 2 contains a literature study which introduces and further discusses the essential topics of this study: deep beams, FRP reinforcement, existing test data and existing models.

Chapter 3 is divided into three main sections which corresponds to the three observed failure modes. The first failure mode is based on the original crack-based 2PKT and presents the following steps: the crack tracking methodology, the kinematics of the model, the mechanisms of shear resistance and the solution procedure. The second and third section describe the modelling of the two other failure modes.

Chapter 4 presents and discusses the results. In first instance, the predictions are compared to the experimental results for each specimen. Next, a comparison is made between specimens to analyse the effect of different test variables. This chapter finishes with a summary table of the strength predictions for all specimens.

The final chapter formulates a conclusion and recommendations for future work.

2 Literature review

2.1 Deep beams reinforced with fiber-reinforced polymers (FRPs) bars

In the past, numerous research programs have focused on the shear behavior of reinforced concrete beams. There are two important parameters which will define how to approach the analysis: the first important is the shear span-to-depth ratio a/d which will define if the concrete element is treated like a slender beam ($a/d > 2.5$) or a deep beam ($a/d \leq 2.5$) [13]. As can be seen in Fig. 2.1, when the a/d ratio decreases below 2.5, the shear stress at failure will increase rapidly which indicates that the shear behavior is changing. The second parameter to distinguish is the presence or absence of web reinforcement.

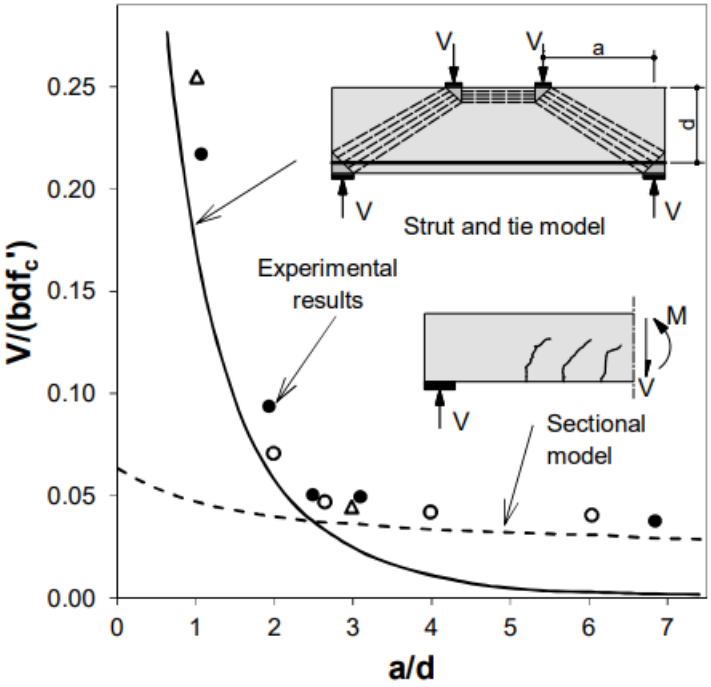

Figure 2.1: Effect of member slenderness on the shear strength of beams [14]

Deep beams transfer shear forces to their supports through compressive stresses rather than shear stresses. The cracking of a deep beam happens in three phases: firstly, an elastic behavior of the deep beam is observed without any cracking. Then, almost vertical flexural cracks develop at the bottom side of the beam from the center to the supports. Finally, diagonal cracks are formed from the support to the loading plate. These diagonal cracks eliminate the principal tensile stresses required for beam action and will lead to a redistribution of internal stresses so that the beam starts to behave like a tied arch. The changing behavior during the loading of a FRP-reinforced deep beam can be seen on a load-displacement response as shown in Fig. 2.2. There can be seen that these three stages of cracking can be associated with different stiffness levels of a deep beam. First they behave very stiff in the elastic region until the flexural cracks are developed. The formation of these cracks leads to a loss of stiffness. In the following stage the diagonal cracks are formed which comes together with a transition of beam action to arch action behavior. This transition is associated with a slight increase of the stiffness, but can not be easily distinguished.

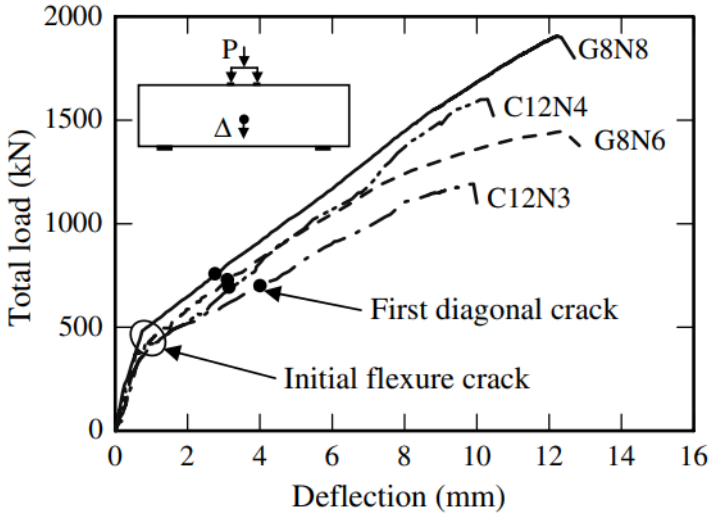

Figure 2.2: Load-deflection response of FRP-reinforced deep beams [15]

2.2 Fiber-reinforced polymers as reinforcement

Since the early days of conventional steel-reinforced concrete a lot of research has been performed to obtain a very good understanding of its behavior. This research did not only discover the many advantages of reinforced concrete, but also its limitations. One of the big issues of steel reinforcement is that it is susceptible to corrosion which leads to undesired behavior of the constructive elements. Particularly, in environments where the risk that corrosion occurs is very high, there is a certain interest to use a non-corrosive substitute for the steel reinforcement. One of these possible substitutes are fiber-reinforced polymers.

It is only since the 1980s that the first significant studies on FRP were performed in Europe [16]. This composite material consists of longitudinal fibers embedded in a resin matrix and has some interesting characteristics like being non-corrosive, lightweight (one-fourth the weight of steel), non-magnetic and non-conductive [4]. It was firstly invented to repair and strengthen existing structures, but during time, it was also used as structural reinforcement. This means that the fibers can be used internally as a replacement for the steel bars, but they can also be added externally to reinforce the member.

Generally, FRP reinforcement exhibits a high tensile strength in the direction of the fibers, up to five to six times higher than conventional steel, but it behaves linear elastic. This implies that there is a brittle failure without any yielding. Furthermore, FRP reinforcement has a stiffness up to six times lower than steel, which has a direct effect on crack widths and deflections.

FRP reinforcement is in fact a collective name for different types of fibers such as: glass (GFRP), carbon (CFRP), aramid (AFRP) and basalt (BFRP). The behavior of the two types considered in this study, GFRP and CFRP, are compared with steel in Fig. 2.3. There can be seen that CFRP reaches a higher tensile strength in comparison to GFRP and steel. The common types of CFRP have a tensile strength of 1500 MPa in comparison to 800 MPa for GFRP and around 450 MPa for steel. Furthermore, CFRP is stiffer than GFRP, but not as stiff as steel. The modulus of elasticity for CFRP is usually around 150 GPa in comparison to 40 GPa for GFRP and 200 GPa for steel. Therefore, it may seem obvious to prefer the use of CFRP instead of GFRP. However, according to literature, CFRP is three times more expensive than GFRP [17]. Although, to obtain the same axial stiffness in a concrete element, the cost by

using CFRP is more comparable to cost by using GFRP [17].

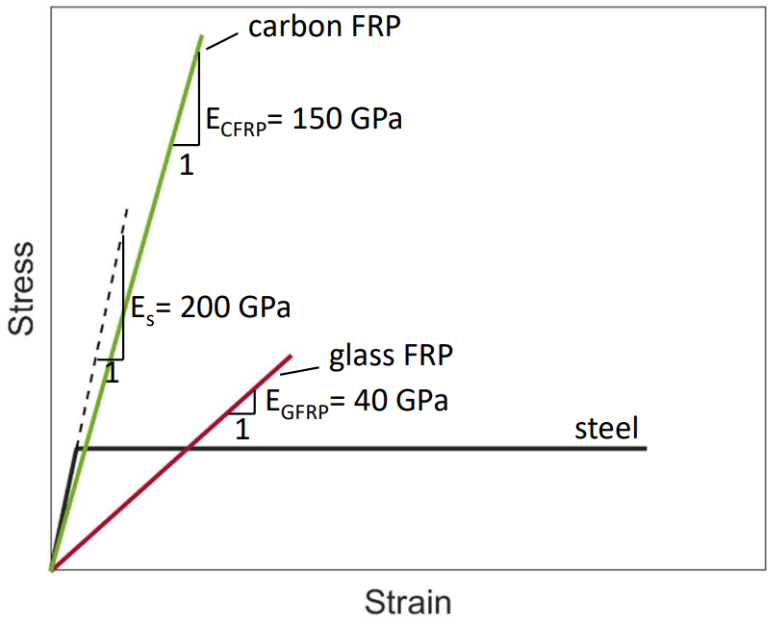

Figure 2.3: Stress-strain relationships for different types of FRP reinforcement and steel

Besides the brittle-elastic behavior, FRP reinforcement experiences another drawback: creep rupture. This failure mode occurs due to increasing deformation under constant load. The likeliness of this phenomenon to happen depends on the type of FRP reinforcement that is used. While carbon fibers are the least susceptible, the more commonly used glass fibers are the most susceptible due to their lower modulus of elasticity E_{GFRP} [18]. Design codes prevent the risk of creep rupture by limiting the allowable stress in the FRP reinforcement. The sustainable stress for GFRP is limited to $0.2f_{FRP,u}$ (ACI 440.1R-06) [4] or $0.3f_{FRP,u}$ (CSA S806-02) [5].

Finally, bonding of the FRP reinforcement to concrete is achieved trough friction or mechanical interlock. Friction is obtained by sand coating the bar, while mechanical interlock is gained via wraps placed around the bars in different directions. Research suggests that the bonding of FRP bars to concrete is less effective compared to conventional steel bars [19]. From the pull-out tests performed by Baena et al. [20], the ratio between the average bond stress for similar sized steel and FRP bars can be determined. The area under the curve in Fig. 2.4 is divided by the maximal slip to obtain the average bond stress τ_{avg}. In normal strength concrete (NSC), the ratio is equal to $\tau_{FRP}/\tau_{steel} = 0.92$, while in high strength concrete (HSC), the ratio is equal to $\tau_{FRP}/\tau_{steel} = 0.44$. These results confirm that FRP bars have a smaller average bond strength than steel bars.

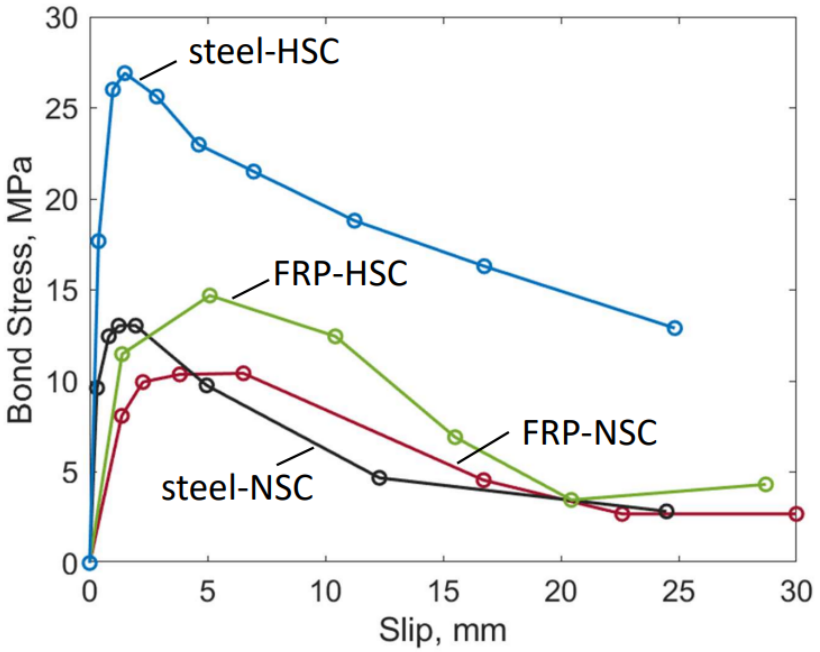

Figure 2.4: Bond stress development during a pull-out test on FRP and steel bars in normal-strength concrete and high-strength concrete (based on tests [20])

2.3 Existing tests on FRP-reinforced deep beams

Due to the scope and the purpose of this thesis, the overview only consists out of large test specimens without transverse reinforcement. Furthermore, the availability of test data and pictures of the specimens, especially of the cracks, formed essential requirements to be considered in this study. The definitions of the geometrical parameters are shown in Fig. 2.5.

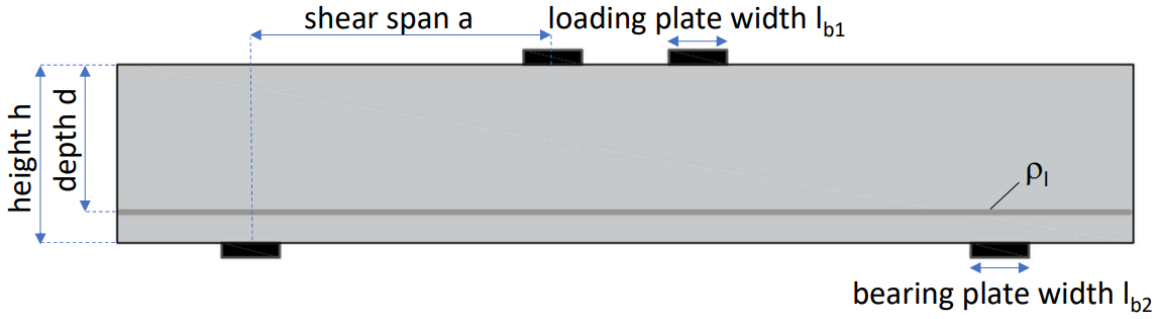

Figure 2.5: Definition of geometrical parameters in deep beams

2.3.1 Tests by Andermatt and Lubell (2010)

Andermatt and Lubell presented the experimental results of twelve GFRP-reinforced concrete deep beams without web reinforcement [9]. The main variables in the testing program were the height h, the shear span-to-depth ratio a/d, the reinforcement ratio ρ_l and the concrete strength $f_c^{'}$. The A-test series had a height of approximately 310 mm, the B-test series a height of 610 mm and the C-series a height of 1000 mm. The a/d ratio varied from 1.07 to 2.06 and the reinforcement ratio from 1.47 to 2.13. There were nine normal strength concrete specimens with a concrete strength between 40 and 51 MPa. The remaining three high strength concrete

specimens had a concrete strength ranging from 65 to 68 MPa. The GFRP bars, with diameters of 19, 22 and 25 mm, were sand-coated and contained surface deformations produced from wrapping groups of fibers diagonally in opposite directions, as a diamond shaped pattern. All the deep beams were tested in four-point bending using displacement control.

Andermatt and Lubell [8] observed excessive maximum crack widths equal to 0.7 mm at the equivalent service load. More than half of all specimens did not meet the ACI 440.1R-06 crack width criterion for structures not subjected to aggressive environments. Those who did meet the criterion had large a/d, large ρ_l or small h. The crack widths at the last loading stage prior to failure ranged from 1.25 to 7.0 mm and increased even more after failure. According to the authors, for some specimens, the cracks were wide enough to see through the beam [8].

The authors described the crack development as follows [8]: the first flexural cracks appeared near mid-span at the bottom side of the specimens between 14 and 35% of the failure load. Then, the flexural cracks developed closer to the bearing plates and started to incline which eventually formed the diagonal critical crack. This formation was still at equivalent service-load condition with an average load of around 45% of the failure load. Only specimen A4H exhibited this crack formation in a later stage around 85% of the failure load. There must be said that this specimen has the largest a/d ratio of 2.1, is made of high strength concrete, and featured the smallest depth of the test series. If this specimen is excluded, the average load where the diagonal crack appeared, decreases to almost 40% of the failure load. The crack development is presented in Fig. 2.6.

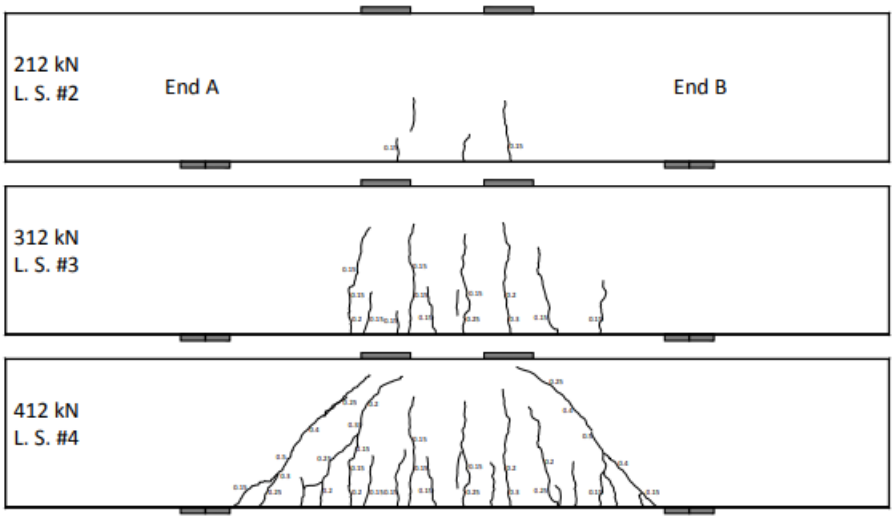

Figure 2.6: Typical initial crack development in specimen B4N [8]

After this diagonal crack was formed, some differentiating behavior was observed. For most of the specimens, the critical inclined crack extended from the inside of the bearing plate towards the loading plate, but for some of these specimens the angle of the crack reduced suddenly near the loading plate and became more and more horizontal as can be seen in Fig. 2.7a. In the zone between the top of the beam and the horizontal crack, concrete crushing was observed. In other specimens, the crack was curved in a S-shape and extended above the diagonal line between the loading plate and the bearing plate, which eventually led to the formation of a tensile splitting crack formed at the top of the shear span as can be seen in Fig. 2.7b.

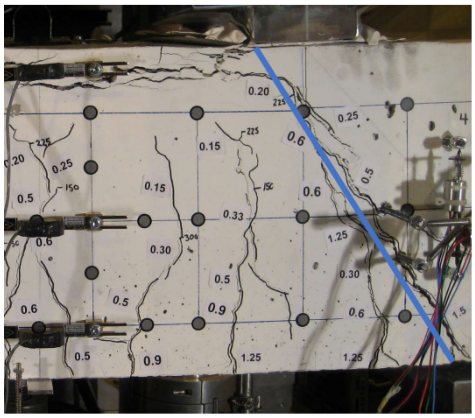

(a) Horizontal crack propagation under the loading plate in specimen A1N

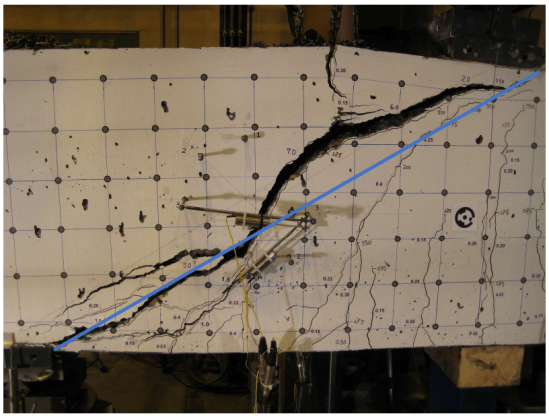

(b) Vertical crack development at top side of specimen B6H

Figure 2.7: Different crack propagation in FRP-reinforced deep beams (courtesy by Andermatt and Lubell, University of Alberta)

2.3.2 Tests by Farghaly and Benmokrane (2013)

In the research of Farghaly and Benmokrane, a testing program of four large-scale FRP-reinforced deep beams without web reinforcement was conducted [15]. The only variables were the type of FRP reinforcement and the reinforcement ratio ρ_l. The first two specimens were reinforced with sand-coated GFRP, where the first specimen had bars of diameter 19 mm and the second specimen had bars of diameter 25 mm. The second pair of specimens were provided with sand-coated CFRP. The first specimen had bars with diameter 9 mm and the second one bars with diameter 12 mm. All specimens had the same geometry and were made of normal strength concrete. Furthermore, a top reinforcement was foreseen, but no details were provided. All deep beams were tested in four-point bending using load control.

Farghaly and Benmokrane [15] observed no excessive crack widths. The maximum crack widths at failure were around 3.0 mm which are in the same order of magnitude as crack widths in conventional steel-reinforced deep beams [1]. However, they concluded that the reinforcement ratio had a clear effect on the crack widths. By increasing the reinforcement ratio by 80%, the crack widths decreased by 43% for GFRP and 51% for CFRP at the same load level. Nevertheless, at failure, all beams exhibited similar crack widths.

According to the authors, the crack development was as followed [15]: the few initial flexural cracks developed at an early load stage of around 23 to 30% of the failure load. Then, in the shear spans, the cracks started to incline towards the central part of the beam and the main diagonal cracks were formed as can be seen in Fig. 2.8. This phenomenon happened at around 40 to 57% of the failure load. There was observed that the critical cracks propagated for all specimens from the inside edge of the bearing plate to the loading plate until a brittle failure occurred, induced by diagonal concrete crushing above the top zone of the crack.

Figure 2.8: Diagonal crack propagation in specimen G8N6 [15]

2.3.3 Observed failure modes

The deep beams reinforced with FRP bars exhibited differentiating behavior. Three different failure modes have been observed in a total of sixteen test specimens of Andermatt and Lubell [8], and Farghaly and Benmokrane [15] as presented in Fig. 2.9.

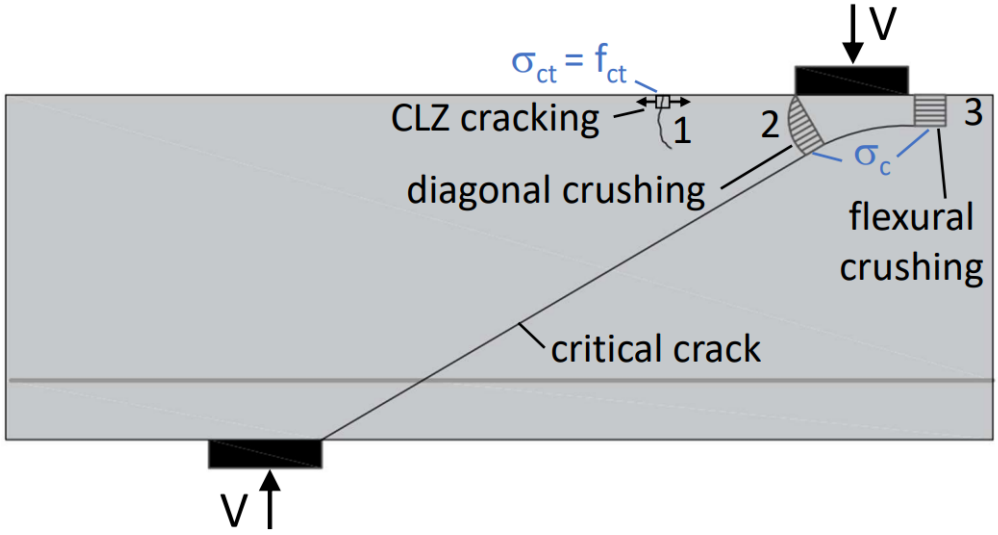

Figure 2.9: Three observed failure modes in FRP-reinforced deep beams

1. Cracking of the critical loading zone

Failure mode 1 shown in Fig. 2.9 is only observed in specimen B6H of Andermatt and Lubell [8]. Here, the diagonal crack extended above the diagonal causing an S-shaped crack, which approached the top zone in a flatter way. This resulted in the formation of a vertical crack from the top side of the beam towards beam axis. To address the modelling part, this failure mode will be captured by means of cracking of the critical loading zone (CLZ). The critical loading zone is located at the top side of the beam near the loading plate. The definition of this zone will be further discussed in Chapter 3.

2. Crushing of the critical loading zone under diagonal stresses

All specimens of Farghaly and Benmokrane [15] exhibited failure mode 2 shown in Fig. 2.9. The

crack propagated from the inner edge of the bearing plate to the outer edge of the loading plate. The brittle failure mode was induced by opening of the diagonal crack with diagonal crushing of concrete in the critical loading zone. This behavior is similar to deep beams reinforced with conventional steel reinforcement.

3. Shear-induced flexural crushing

In the majority of specimens of Andermatt and Lubell [8], failure mode 3 shown in Fig. 2.9 has been observed. The crack propagated from the inner edge of the bearing plate towards the inner edge of the loading plate, but in the vicinity of the critical loading zone, the crack angle suddenly reduced and in some cases it became horizontal beneath the loading plate. Concrete crushing was observed in the region between the top side of the specimen and the (almost) horizontal crack.

2.3.4 Summary tests database

Table 1: Database of FRP-reinforced deep beam tests

References	Beam name	a/d	b (mm)	h (mm)	a (mm)	l_{b1} (mm)	V/P	E_{FRP} (GPa)	ρ_l (%)	Number of bars	$f_{FRP,u}$ (MPa)	a_g (mm)	$f_c^{'}$ (MPa)	$V_{\exp}$ (kN)
Andermatt and Lubell (2010)	A1N	1.07	310	306	276	100	1	41.1	1.49	3	709	14	40.2	407.0
	A2N	1.44	310	310	376	100	1	41.1	1.47	3	709	14	45.4	235.5
	A3N	2.02	310	310	527	100	1	41.1	1.47	3	709	14	41.3	121.5
	A4H	2.02	310	310	527	100	1	41.1	1.47	3	709	14	64.6	96.0
	B1N	1.08	300	608	545	200	1	37.9	1.70	8	765	14	40.5	636.5
	B2N	1.48	300	606	743	200	1	37.9	1.71	8	765	14	39.9	399.5
	B3N	2.07	300	607	1040	200	1	37.9	1.71	8	765	14	41.2	215.5
	B4N	1.48	300	606	736	200	1	41.1	2.13	8	709	14	40.7	415.0
	B5H	1.48	300	607	736	200	1	41.1	2.12	8	709	14	66.4	531.0
	B6H	2.06	300	610	1040	200	1	37.9	1.70	8	765	14	68.5	188.0
	C1N	1.1	301	1003	974	330	1	42.3	1.58	8	938	14	51.6	1134.5
	C2N	1.49	304	1005	1329	330	1	42.3	1.56	8	938	14	50.7	662.0
Farghaly and Benmokrane (2013)	G8N6	1.14	300	1200	1250	130	1	47.6	0.69	8	790	20*	49.3	723.5
	G8N8	1.15	300	1200	1250	130	1	51.9	1.24	8	750	20*	49.3	953.0
	C12N3	1.13	300	1200	1250	130	1	120.0	0.26	12	1596	20*	38.7	595.5
	C12N4	1.13	304	1200	1250	130	1	144.0	0.46	12	1899	20*	38.7	800.5

*Assumption

2.4 Existing models

There are several models available to predict the shear behavior of slender beams and only a few are suitable for deep beams. These models were not all developed for the same purposes, and, therefore, there are some major differences between them regarding the approach, the assumptions and the complexity.

In the following sections, different models suitable for deep beams are presented. First, one of the most used models to evaluate the strength of a deep beam is introduced: the strut-and-tie model (STM). This section is followed by a rather new model: the two-parameter kinematic theory (2PKT). This model predicts the complete load-deformation response, accounting for kinematics. Finally, a finite elements analysis is presented which is used to enhance the understanding of the structural response of deep beams.

2.4.1 Strut-and-tie model (STM)

The strut-and-tie model is particularly used for regions where Hooke's principle of plane-sections-remain-plane is no longer applicable. In other words, regions where non-linear strain distribution occurs. Many refer to such regions as D-regions which stands for disturbed or discontinuous region. It is defined as a region and not as an element, because one single member or structure can be constituted out of both B-regions and D-regions as demonstrated in Fig. 2.10. However, this is not mandatory, because in deep beams only a D-region is observed. Nevertheless, there can be concluded that in almost every reinforced concrete structure D-regions are present. Therefore, the STM has a very large application field, because it can be used in any D-region.

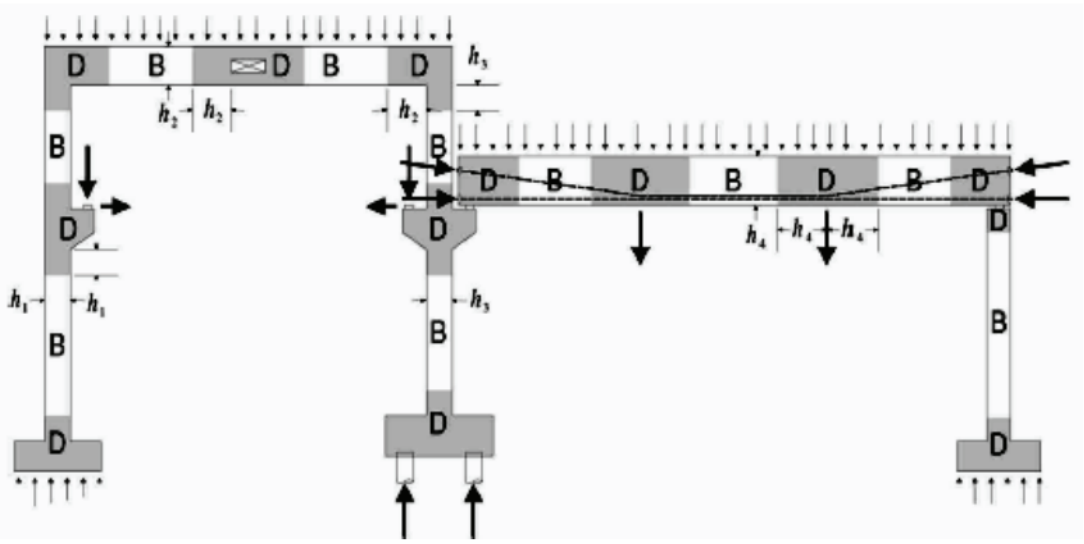

Figure 2.10: Localization of B- and D-regions in concrete structures [21]

Strut-and-tie modelling is based on the lower bound theory of plasticity which implies that the predicted capacity will be lower than the experimental capacity. Generally, it is a conservative approach. As the name of the model suggest, the STM is mainly based on the usage of compression and tension bars as illustrated in Fig. 2.11. The struts and ties come together in the so called nodes. The struts are used to represent the compressive stress field in concrete after cracking, while the ties are introduced to represent the tensile force in the reinforcement. Furthermore, the forces are assumed to be constant in all bars.

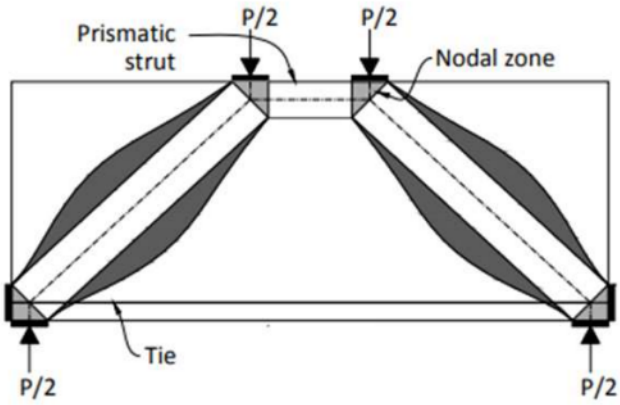

Figure 2.11: Strut-and-tie model for a deep beam in four-point bending (adapted from [8])

The design of the three types of elements, struts, ties and nodes, is performed separately. This means that each element is designed to resist the applied forces. Although the design is rather simple, straightforward and performed well in the past, STM has its limitations. One of the limitations of strut-and-tie modelling, is that the model is based on ductility, whereas, deep beams may exhibit brittle failures. Moreover, FRP reinforcement bars behave, by definition, brittle-elastic. Another limitation of STM regards the following: as seen in research, the capacity of a deep beam does not only depend on its geometrical and material properties. Also the randomness of the crack geometry can influence the capacity [12]. This crack geometry can not been taken into account in the STM.

STMs were used by Andermatt and Lubell [8] to predict the shear capacity of their FRP-reinforced deep beam tests. They used the CSA A23.3-04 for general concrete structures [22] and the ACI 318-08 to predict the shear capacity of the twelve specimens. Modifications needed to be done to take into account the FRP reinforcement. In 2014, Farghaly and Benmokrane performed a new test serie of FRP-reinforced deep beams [15]. They approached their experimental results with the CSA S806-12 for FRP-reinforced concrete structures, which uses almost the same equations as CSA A23.3-04 for general concrete structures, and the ACI 318-08. A summary of the results is presented in Table 2.

In general, there can be concluded that the CSA model underestimated the capacities, while the ACI 318-08 overpredicted them. Furthermore, the coefficients of variation (COVs) are for both models almost 20% higher in the tests of Andermatt and Lubell with respect to the tests of Farghaly and Benmokrane. This suggests that the predictions were not very consistent.

Besides the inconsistent results, these STMs do not always predict the right failure mode. As discussed in Section 2.3.1, most of the specimens of Andermatt and Lubell [8] exhibited failures in the top zone of the beams, in the region of the loading plate, as seen in Fig. 2.12. In contrary, the authors reported that the STMs predict in the majority of cases problems along the diagonal concrete strut [8]. This difference in behavior has not been taken into account by the different strut-and-tie models. This can be partially explained by the fact that STM are suited for plastic materials and not for brittle ones like FRP bars. Furthermore, some type of FRP reinforcement can exhibit creep problems, which is a deformation problem as discussed in Section 2.2, but STMs are strength-based models and not deformation-based.

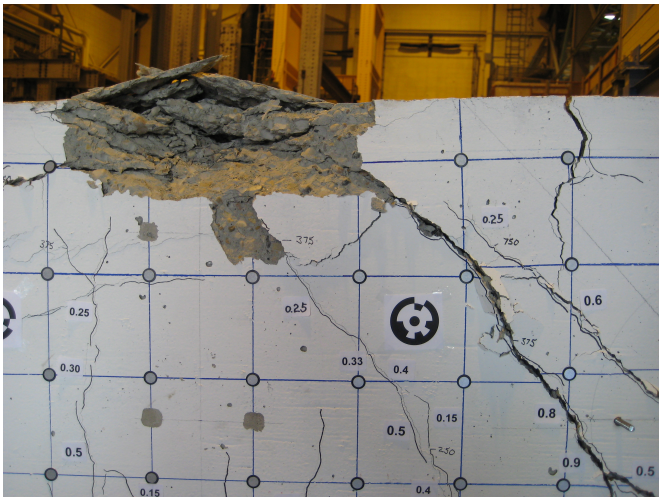

Figure 2.12: Crushing of concrete in the top zone of a deep beam, specimen B1N (courtesy by Andermatt and Lubell, University of Alberta)

2.4.2 Two-parameter kinematic theory (2PKT)

The 2PKT, originally developed for deep beams reinforced with steel bars [11], is a kinematic model with only two degrees of freedom (DOFs). Complex deformation patterns of diagonally-cracked point-loaded deep beams subjected to single curvature can be reproduced by only using first principles such as equilibrium equations, compatibility of deformations and constitutive relationships for the different mechanisms of shear resistance. These deformation patterns include deflections, crack widths and slips, and complete displacement fields.

The model assumes that the critical diagonal crack extends from the inner edge of the bearing plate towards the loading plate. All concrete above this crack is considered as one rigid block, while below the crack the concrete is represented by a fan of rigid radial struts. Both sides of the crack are connected by the critical loading zone (positioned beneath the loading plate), by the bottom longitudinal reinforcement and by the stirrups.

The two degrees of freedom of the kinematic model, represented in Fig. 2.13, are defined by the motion of the rigid block with respect to the loading plate: a rotation around the tip of the crack and a vertical translation. The first one is the average strain in the bottom longitudinal reinforcement $\varepsilon_{t,avg}$ and the latter is the vertical displacement Δ_c in the critical loading zone (CLZ). By introducing these two DOFs, there can be seen that vertical lines below the crack will remain vertical, while vertical lines above the crack will rotate and, hence, this model also takes into account that plane sections do not remain plane in deep beams.

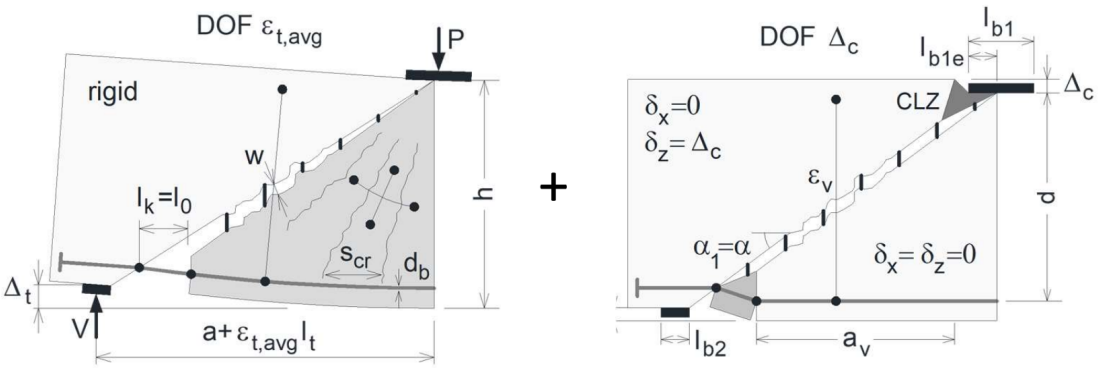

Figure 2.13: Degrees of freedom in the kinematic model [11]

The shear capacity prediction of the 2PKT is obtained by finding an equality between the vertical sum of four shear mechanisms and the shear force resulting from a moment equilibrium induced by the tensile force in the reinforcement. The solution is found by controlling and varying one DOF, Δ_c, and calculating the other DOF, $\varepsilon_{t,avg}$, until equilibrium is satisfied.

This theory was used in the past by Mihaylov to study the behavior of FRP-reinforced deep beams [23]. According to the author, the initial predictions overestimated the experimental capacities due to an overestimation of a shear mechanism related to the critical loading zone. This was caused by effects of the usage of FRP reinforcement which was not explicitly accounted for in the model. This resulted in the introduction of a factor k in the model which took into account the difference in behavior and decreased the contribution of the critical loading zone, and, thus, decreased the predicted shear capacity. However, this factor k was derived in a semi-empirical manner based on the experimental shear capacity and, thus, did not have an explicit physical meaning. The average experimental-to-predicted ratio for thirty-nine tests was equal to 1.06 with a COV of 18% [23]. To compare the average ratio and COV for the STMs and 2PKT, only the predictions for similar test series are presented in Table 2.

In general, there can be concluded that the modified 2PKT shows good predictions on average for the tests of Andermatt and Lubell [8], but in a inconsistent way. The tests of Farghaly and Benmokrane are underestimated by 16% on average.

These results were obtained after the introduction of the factor k, which improved the results, and, as discusses before, did not have a direct physical meaning. Another issue of the model is that it uses a straight crack which means that it does not include the measured crack pattern as an input parameter. Other research already suggested to do so, because a difference in capacity was observed for similar beams with only a difference in the developed crack geometry.

From Table 2, there can be concluded that no matter which model is used, the specimens of Andermatt and Lubell [8] are not predicted in a consistent way. This implies that the behavior of some of their specimens is different from the model predictions. Further, the tests of Farghaly and Benmokrane [15] are consistently underpredicted with the CSA model and the 2PKT. Also the ACI-STM has an average prediction 28% higher for the tests of Farghaly and Benmokrane [15] in comparison to the tests of Andermatt and Lubell [8].

From the results of the STM and the 2PKT, there can be concluded that some tests exhibit very different failures which is not taken into account by the models. Other tests seems to be behave like the model predictions, but the results are conservative. This difference in behavior can be taken into account by using the crack geometry as an input parameter. This had not

been done in the STMs and the original 2PKT.

This was done by Trandafir et al. [12], who extended the original 2PKT by introducing the crack geometry as an input parameter in the model. Therefore, the model can be used to assess the state of existing deep beams. Not only is the model capable of capturing the difference in shear response for nominally identical members with different crack geometries, but it also predicted the interlock stress distribution along the critical cracks. A full response is obtained for the capacity and the displacements. Therefore, the crack-based 2PKT has proven to be a useful model to approach deep beams. However, it still needs some adjustments to be applicable to FRP-reinforced deep beams and to maintain a rational modelling basis.

2.4.3 Finite element analysis

Finite element analysis is a collective name for a wide range of different models. Every model is based on different assumptions and uses different type of elements. However, finite element analysis can be described in a general way. Enem et al. [24] stated that the finite element method is a powerful and general analytical tool for studying the behavior or reinforced concrete deep beams. It can offer solutions for linear and nonlinear behavior of deep beams.

Metwally [25] performed a finite element study on the specimens of Andermatt and Lubell [8]. By using an existing software, he generated linear and nonlinear finite element models (FEM) to simulate numerically the response of these deep beams. The model is based on two components: solid elements to represent the concrete deep beams and the loading and bearing plates, and, truss elements to represent the FRP longitudinal reinforcement. The results of his analysis are shown in Table 2.

Table 2: Summary of strength comparisons of existing models [8, 15, 23, 25]

	STM				2PKT		FEM	
	CSA A23.3-04		ACI 318-08					
Test program	V_e/V_p	COV	V_e/V_p	COV	V_e/V_p	COV	V_e/V_p	COV
Andermatt and Lubell	1.03	20%	0.60	34%	1.00	13%	1.01	5%
Farghaly and Benmokrane	1.07*	1%*	0.88	15%	1.16	6%	/**	/**

V_e/V_p = experimental to predicted shear ratio
*Instead of CSA A23.3-04, CSA S806-12 for FRP-reinforced members was used
**Tests were not modelled

The capacities are very well predicted with the finite element analysis, and, in a consistent way. There must be noted that the mesh of the model seems big and therefore, may possibly not take into account some internal mechanical interactions. Although, there is no doubt that, by using finite element analysis, the response of deep beams with FRP reinforcement is well simulated. However, it comes with a cost: the STM can be calculated very fast and even by hand, and, the crack-based 2PKT only needs a measurement of a crack and limited knowledge about the model. However, the finite element analysis is much more complex, needs a certain expertise to understand and reproduce the model, and is more time consuming.

3 Crack-based 2PKT for FRP-reinforced deep beams

3.1 Introduction

In research programs, it has been observed that deep beams reinforced with FRP reinforcement do not always behave like conventional deep beams. Not only do they have very large crack widths (up to 7.0 mm), but they also exhibit different failure modes. In total, three different failure modes have been observed in tests: crushing of the critical loading zone under diagonal stresses, cracking of the critical loading zone and shear induced flexural crushing. The goal of the model is to predict the right failure mode and corresponding capacity by only using first principles such as equilibrium equations, compatibility of deformations and constitutive relationships. Moreover, not only the final capacity, but the full response is predicted which means that all displacements are calculated as a function of the load. These displacements are the strain in the FRP bar, the crack widths and the deflections at mid shear span. These predicted results can be compared to experimental measurements.

The model is based on the crack-based 2PKT from Trandafir et al. [12]. This means that the crack geometry is digitized and used as an input parameter in the 2PKT. The 2PKT is based on only two DOFs: the average strain in the FRP bottom reinforcement $\varepsilon_{t,avg}$ and the vertical displacement of the critical loading zone Δ_c. However, in the new model the horizontal displacement of the critical loading zone Δ_{cx} will be introduced as a third DOF. This new DOF is by definition an independant deformation, but it is estimated as a function of DOF Δ_c which is further discussed in the following sections. Furthermore, the effects of the use of FRP reinforcement is implemented in the new model, because FRP bars behave in a brittle-elastic way and have a very low stiffness in comparison to steel which will lead to larger deformations and, therefore, larger crack widths. There is also observed that the average bond stress of FRP reinforcement in concrete is lower than the average bond stress of steel which leads to a higher anchorage length and, therefore, a larger crack spacing. Out of the three observed failure modes, the crack-based 2PKT only takes into account the failure mode due to crushing of the critical loading zone (refer to failure mode 1 in Section 2.3.3). Therefore, the model will be extended by introducing the two other observed failure modes: cracking of the critical loading zone and shear-induced flexural crushing (refer to respectively failure mode 2 and failure mode 3 in Section 2.3.3). These two failure modes will be implemented inside the crack-based 2PKT model. This means that the full response, regarding the capacity and the corresponding displacements, is calculated by the crack-based 2PKT until the minimum capacity of the three capacities, corresponding to the three failure modes, is reached.

An additional mini model was created to compare the experimental results with the predicted results. The original crack-based 2PKT was developed for deep beams in three point bending, and, therefore, the experimental deflections of the test specimens in four-point bending need to be modified to equivalent deflections in three-point bending to be able to compare predicted and experimental results. In practice, this means that the deflection due to the pure bending region need to be subtracted from the total deflection measured at mid span during the test such that the modified deflection can be compared with the predicted one.

Some parts of the original model will not be reused, because the scope of the study is on FRP-reinforced deep beams without web reinforcement. This means that one of the four shear mechanisms, the shear contribution of stirrups, will not be taken into account anymore because there is no web reinforcement present in the tests.

3.2 Crack tracking and discretization

The crack geometry can be directly measured on in-service deep beams or on test specimens. Although deep beams did not fail, the critical cracks can already be determined, because the cracks in deep beams propagate at relatively low load levels [9, 15]. The crack is discretized into smaller crack segments by using a grid. As shown by Trandafir et al. [12], the grid size should not be chosen smaller than the maximum size of coarse aggregates in the concrete a_g. Otherwise, some segments of the crack will have very steep angles which results in large shear stresses and, by so, in a larger shear force as shown in Fig. 3.1. Furthermore, for very small grid sizes, the crack segments will take into account the micro-roughness of a crack which is already embedded in the constitutive model of the contact density model (CDM) [26]. This will be further discussed in Section 3.4.2. Therefore, to obtain a general approach, the critical diagonal crack is firstly discretized by line segments on a grid of 5x5 mm. Afterwards, these line segments are redefined such that the length of a segment is approximately equal to a_g. Finally, each crack segment i is defined by its angle with respect to the horizontal axis $\alpha_{cr,i}$ and its coordinates x_i and y_i.

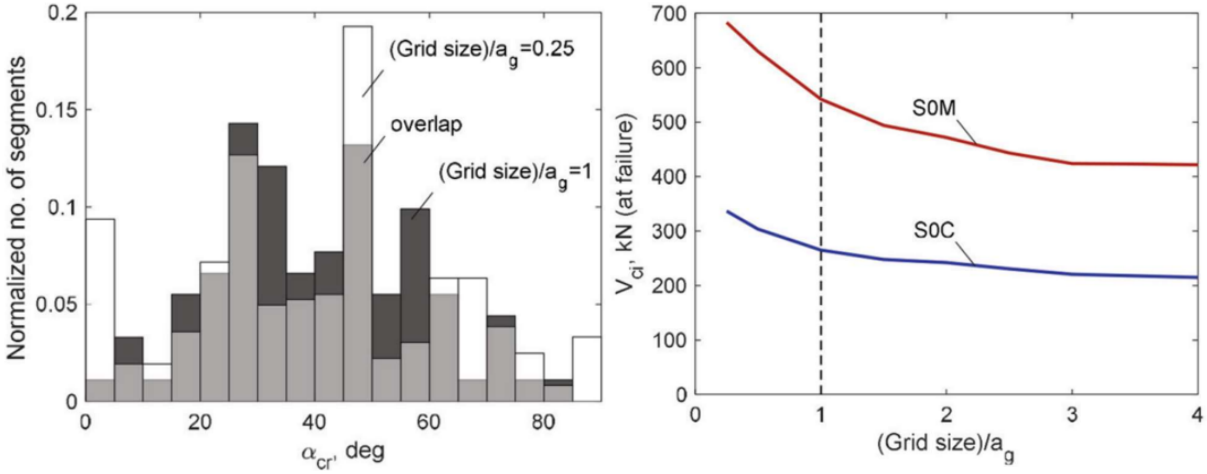

(a) Crack angle distribution for different grid sizes (b) Variation of aggregate interlock shear force as a function of the orthogonal grid size

Figure 3.1: Influence of the size of the grid on the shear force [12]

3.3 Kinematics of deep beams

The new model is built on three degrees of freedom to model the complete deformed shape of deep beams. The three degrees of freedom are the average strain in the bottom longitudinal FRP reinforcement $\varepsilon_{t,avg}$, the vertical displacement Δ_c in the critical loading zone (CLZ) and the horizontal displacement Δ_{cx} in the CLZ. The original 2PKT made use of only two degrees of freedom, but Mihaylov introduced a third DOF [27], Δ_{cx}, which had proven to be very effective to capture the complete load-deflection response.

As seen in Fig. 3.2, the introduced crack geometry divides the deep beam into two. All concrete above this crack is considered as one rigid block, while below the crack the concrete is represented by a fan of rigid radial struts. Both sides of the crack are connected by a critical loading zone (positioned beneath the loading plate) and the bottom longitudinal FRP reinforcement. The three degrees of freedom of the kinematic model are defined by the motion of this rigid block with respect to the loading plate: a rotation around the tip of the crack, a vertical translation and a horizontal deformation engaging a rotation around point O as seen in Fig.

3.2. This can be described more in detail as the elongation of the bottom reinforcement results in a rotation of the radial struts around the loading point and so in increasing horizontal displacements. So, DOF $\varepsilon_{t,avg}$ leads to linearly increasing horizontal displacements. Next, DOF Δ_c results in a constant horizontal and vertical displacement along the crack. Finally, the horizontal deformation of the CLZ expressed by DOF Δ_{cx} leads to an increasing vertical displacement, but a decreasing horizontal displacement.

It can be concluded that the horizontal and the vertical displacement of every crack segment can be determined from the kinematics. Therefore, the deflection of the beam, which is measured at the support, is also known, because it is related to the vertical displacement. While the vertical displacement and deflection depend on all three DOFs, the horizontal displacement only depends on $\varepsilon_{t,avg}$ and Δ_{cx}. These orthogonal displacements are easy to derive in function of the DOFs, however, it is of more interest to know the local crack width w and the local crack slip s from every segment to determine the tangential and normal stresses for every segment. Therefore, these orthogonal displacements are projected based on the local angle of each crack segment to obtain the local crack width w_i and the local crack slip s_i. This is further explained in Section 3.4.2.

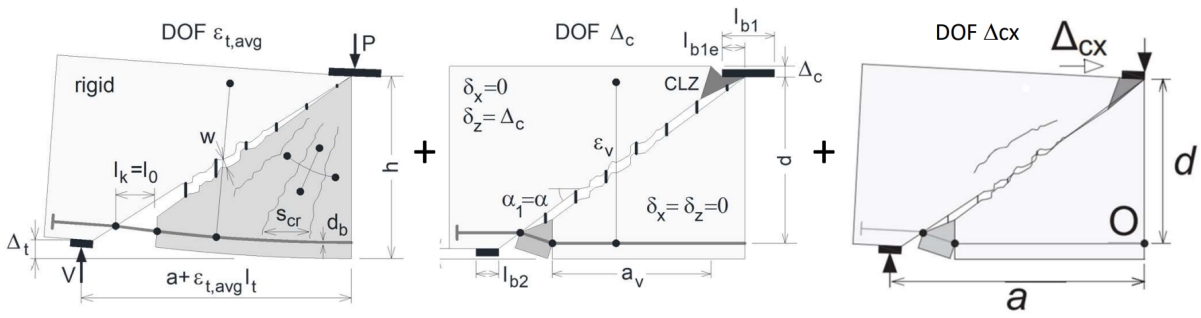

Figure 3.2: Kinematic model for FRP-reinforced deep beams (adapted from [11] and [27])

3.4 Mechanisms of shear resistance

The shear resistance of a deep beam without web reinforcement is composed of three mechanisms: shear force resisted by the CLZ (V_{CLZ}), aggregate interlock along the critical crack (V_{ci}) and dowel action of the longitudinal reinforcement (V_d). As shown in Fig. 3.3, the shear strength is determined as the vertical sum of the three forces.

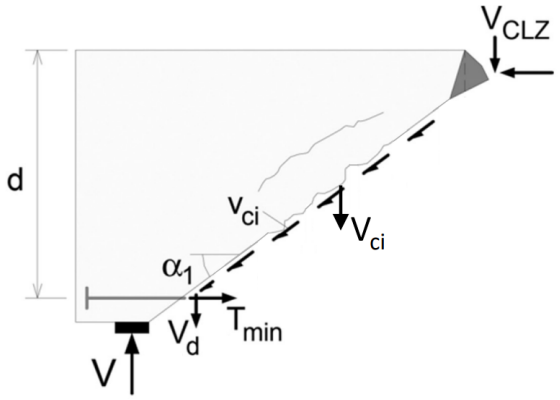

Figure 3.3: Shear mechanisms in FRP-reinforced deep beams without web reinforcement (adapted from [11])

3.4.1 Critical loading zone

The critical loading zone, a key-component of the 2PKT, is carrying a part of the shear force by diagonal compressive stresses. The CLZ was originally determined with a model proposed by Mihaylov et al. [11]. As shown in Fig. 3.4, the compressive strain ε is assumed to vary linearly from zero at the edge of the loading plate to the ultimate strain at the bottom inclined force of CLZ.

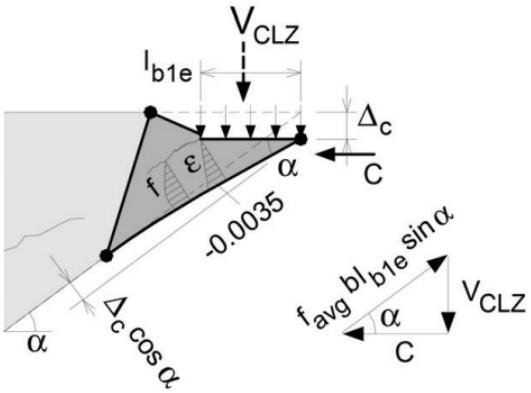

Figure 3.4: Idealized geometry of CLZ in deep beams [11]

As can be seen, the geometry of the CLZ is defined by an idealized triangular deformed shape derived by Mihaylov et al. [11]. However, in the crack-based 2PKT of Trandafir et al., [12] the geometry of the CLZ is defined based on measurements of the crack. This approach is shown in Fig. 3.5.

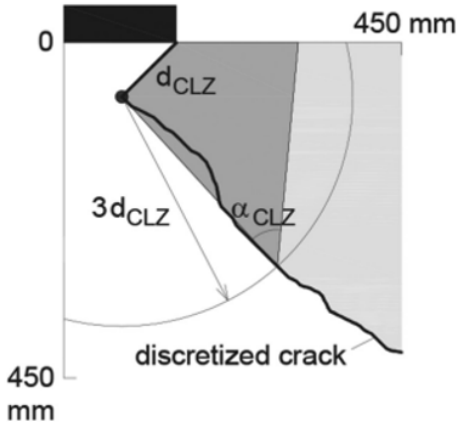

Figure 3.5: Crack-based definition of CLZ geometry [12]

In the crack-based 2PKT, the geometry of the CLZ is determined by two parameters: the angle of the crack α_{CLZ} in the CLZ region (dark grey shade in Fig. 3.5) and the depth of the critical section $d_{CLZ} = l_{b1e} \sin \alpha_{CLZ}$. Instead of predicting this depth, it can be measured directly on the crack geometry, because d_{CLZ} is defined as the shortest distance from the edge of the loading plate to the crack. Next, a circle with radius $3d_{CLZ}$ is drawn from the bottom point of the critical section. This circle represents the size of the critical loading zone. Finally, the radius of the circle that best approximates the critical crack is used to determine the angle α_{CLZ}. These geometrical based parameters are introduced in Eq. (1) according to [12]. The crack shape factor k is not considered when the crack is measured.

$$V_{CLZ} = f_{avg} b d_{CLZ} \sin \alpha_{CLZ} \tag{1}$$

The inclined force of CLZ is determined by the average stress f_{avg} in the CLZ. This stress is directly related to the DOF Δ_c. Both parameters are derived as a function of the strain. The DOF Δ_c is found by $3l_{b1e}e/tan(\alpha)$ and $f_{avg} = \Omega/e$. The strain is varying from zero until failure to obtain the whole envelope of V_{CLZ} and, ultimately, the full response.

3.4.2 Aggregate interlock

Aggregate interlock is a complex mechanism occurring along cracks in concrete structures when the crack surfaces are sliding against each other as shown in Fig. 3.6. The magnitude of the phenomenon is impacted by a roughness acting on different scales. On a macro-scale, the aggregate interlock is influenced by the crack geometry, and more specifically by the angle $\alpha_{cr,i}$ of every crack segment. Steeper crack segments will develop larger shear stresses [12]. However, on a micro-scale, the aggregate interlock is influenced by friction between aggregates which depends on the aggregate matrix arrangement.

The shear force resisted by aggregate interlock is derived from the complete contact density model (CDM) by Li et al. [26]. It predicts the tangential stresses $v_{ci,i}$ and the normal stresses $n_{ci,i}$ acting on each crack segment i in function of the crack width w_i and the crack slip s_i as shown in Fig. 3.6. Then the sum of the vertically projected shear contributions along the whole length of the critical crack is taken to obtain the total shear force resisted by aggregate interlock. The influences of the roughness on a macro- and micro-scale are hereby taken into account in this model, because the macro-roughness is incorporated in the angle of the crack segment and the micro-roughness is embedded in the CDM.

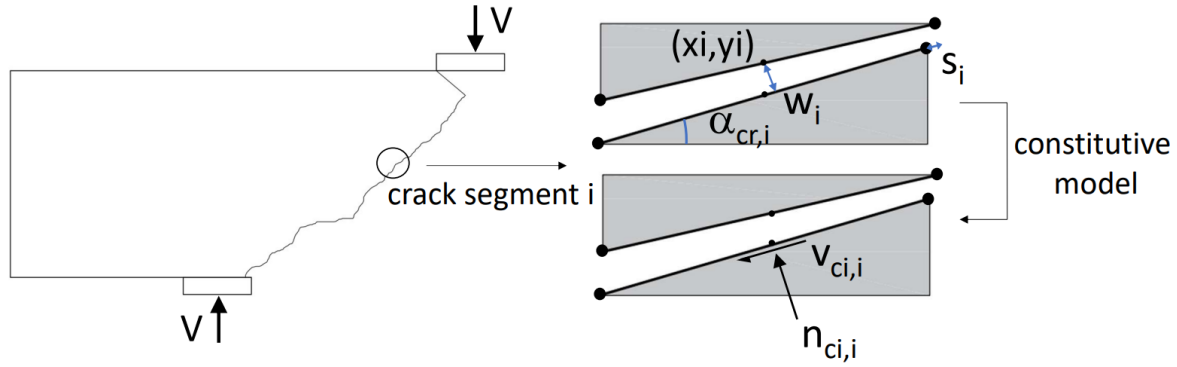

Figure 3.6: Aggregate interlock model with local displacements and stresses

To derive the local stresses, the kinematics of the measured crack, the crack width w_i and crack slip s_i, need to be known. These displacements depend on the coordinates x_i and y_i and the local angle $\alpha_{cr,i}$ of each crack segment i. Therefore, to express them in function of the three DOFs of the model, it is useful to derive the relative horizontal and vertical displacement, $w_{h,i}$ and $w_{v,i}$ of the crack segment which do not depend on local axes, but are a function of the global orthogonal axes. As discussed in Section 3.3, the horizontal displacement $w_{h,i}$ depends on DOF $\varepsilon_{t,avg}$ and DOF Δ_{cx}. On the other hand, the vertical displacement $w_{v,i}$ depends on all three DOFs. For $w_{v,i}$, a distinction is made between the crack segments in the CLZ and out the CLZ. The orthogonal horizontal coordinate x_i of a segment is compared to the length of the CLZ l_{CLZ} which is defined as the horizontal distance from the center of the loading plate to the

end of the CLZ as showed in Fig. 3.5 and can be found by $3d_{CLZ}\sin\alpha_{CLZ}$. The displacements can be derived with Eq. (2).

$$w_{v,i} = \begin{cases} \left(\frac{\varepsilon_{t,avg} l_k}{d} x_i + \Delta_c + \frac{\Delta_{cx}}{d} x_i\right) \frac{x_i}{l_{CLZ}} & \text{if} \quad x_i \leq l_{CLZ} \\ \frac{\varepsilon_{t,avg} l_k}{d} x_i + \Delta_c + \frac{\Delta_{cx}}{d} x_i & \text{if} \quad x_i > l_{CLZ} \end{cases} \tag{2}$$
$$w_{h,i} = \frac{\varepsilon_{t,avg} l_k}{d} y_i + \frac{\Delta_{cx}}{d}(y_i - d)$$

Next, the crack displacements normal and parallel to each crack segment can be expressed with Eq. (3).

$$\begin{aligned} w_i &= w_{v,i}\cos\alpha_{cr,i} + w_{h,i}\sin\alpha_{cr,i} \\ s_i &= w_{v,i}\sin\alpha_{cr,i} - w_{h,i}\cos\alpha_{cr,i} \end{aligned} \tag{3}$$

It can be seen that the local angle $\alpha_{cr,i}$ determines if the horizontal and vertical displacement are locally translated into either relative widths or slips. For straight segments, the slip may be small and the width large, whereas in steep parts of the crack, the width will be small and the slip large.

These equations are similar to the model proposed in the crack-based 2PKT for steel-reinforced deep beams by Trandafir et al. [12]. However, one modification is introduced due to the effects of the use of FRP reinforcement in deep beams. It was observed by Andermatt and Lubell [9] that FRP-reinforced deep beams exhibit very large crack widths in comparison to conventional deep beams. This behavior may be induced by the decreased average bond strength between FRP reinforcement and concrete as discussed in Section 2.2. According to the test data of Baena et al. [20], the average bond strength did decrease. These results support what researchers suggested in the past [19]. However, the available test data is limited, and, therefore, it strongly depends on the material characteristics and the test setup. Baena et al. made use of a pull-out test with a debonded area. This test setup causes a flow of forces around the reinforcement bar which possibly leads to confinement of concrete. This may have possibly influenced the results and caused the differentiating results from normal strength to high strength concrete. Therefore, an assumption of a decrease of 50% of the average bond strength is applied to the model, which can be seen in Eq. 5 by means of $0.5f_{ct}$. This value can be further improved in the future, when more test data is available. The hypothesis can be made that the bond strength is only effecting the local displacements and not the strength of the deep beam.

The average bond strength is directly proportional to the crack spacing s_{cr}. In practice this means that the crack spacing is doubled when a reduction factor of 50% is applied on the bond strength. Furthermore, the decreases average bond strength results in an increase of the anchorage length l_{tr} of the FRP reinforcement which results in an increased l'_k. The quantity l'_k is the sum of the length of the bottom FRP reinforcement whose elongation contributes to the width of the cracks and a supplementary length to take into account anchorage slip as suggested by Trandafir et al. [12]. Proportionally, the crack widths increase too. So finally, the decreased average bond strength will lead to bigger crack widths. The term l'_k can be derived with the following equations

$$
\begin{aligned}
l_0 &= 1.5(h-d)\cot\alpha_1 \geq 2s_{cr} \\
l_k &= l_0 + d(\cot\alpha - \cot\alpha_1) \\
l'_k &= l_k + 0.5l_{tr} - 0.5\frac{[max(l_{tr} - l_{an}, 0)^2]}{l_{tr}} \\
l_{tr} &= \frac{E_{FRP}\varepsilon_{t,avg}d_b}{8 \cdot 0.5 f_{ct}}
\end{aligned}
\tag{4}
$$

where $s_{cr} = (0.28d_b/\rho_l) \cdot 2.5(h-d)/d$ is the spacing of the cracks at the bottom of the section [28] which is multiplied by two as discussed before, d_b is the diameter of the bar, $f_{ct} = 0.33\sqrt{f'_c}$ is the tensile strength of the concrete, $\alpha = \arctan(h/a)$ is the angle between bearing plate and CLZ and $\alpha_1 = \alpha \leq 35°$ is the angle of the critical crack. The expression for the term l'_k assumes that the strains in the FRP bar decrease linearly to zero along l_{tr}, but not beyond anchor heads, hooks or loops as seen in Fig. 3.7.

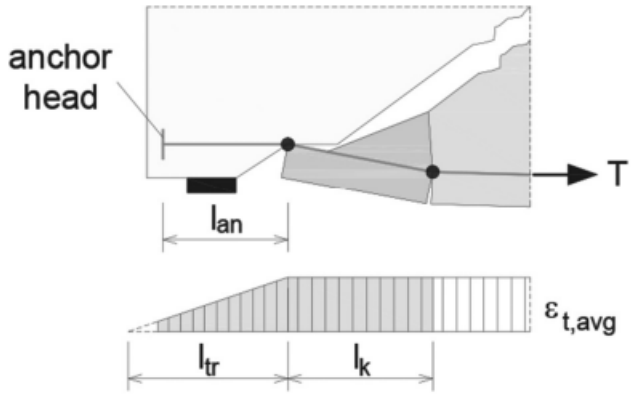

Figure 3.7: Strains along anchorage of FRP reinforcement that contribute to critical crack opening [12]

When the displacements w and s are known, the constitutive model of the contact density model [26] can be used to predict the interlock stresses. The CDM represents the crack surface as a series of contact units oriented with different angles ϕ. A nonlinear contact spring normal to the contact unit is used to model the interaction between the two faces of each unit. These springs behave elastic-perfectly plastic in compression (unit in contact) and have no resistance in tension (no contact). The yield strength of the springs in compression is taken as $f_{c,con}$ $= 0.35 \times 13.7\sqrt[3]{f'_c}$, where 0.35 represents a reduction factor to the yield strength proposed by Trandafir et al. (2022). This reduction factor is particularly relevant for tests on deep beams were wide cracks and, therefore, lower aggregate interlock stresses have been observed, which is the case for FRP-reinforced deep beams. The forces of these springs are projected on axes which are positioned orthogonal to the crack segment orientation and thus obtaining the tangential and normal stresses on these crack segments.

$$
\begin{aligned}
v_{ci,i} &= 0.635 \int_{-\frac{\pi}{2}}^{\frac{\pi}{2}} \sigma_{con} K \sin\phi \cos\phi d\phi \qquad \text{(MPa)} \\
n_{ci,i} &= 0.635 \int_{-\frac{\pi}{2}}^{\frac{\pi}{2}} \sigma_{con} K \cos^2\phi d\phi \qquad \text{(MPa)} \\
\sigma_{con} &= f_{c,con} \frac{s_i \sin\phi - w_i \cos\phi}{0.04} \begin{cases} \leq f_{c,con} \\ \geq 0 \end{cases} \\
K &= 1 - \exp\left(1 - \frac{0.5 a_g}{w}\right) \geq 0
\end{aligned}
\tag{5}
$$

Finally, the shear resisted by aggregate interlock V_{ci} is obtained with Eq. (6).

$$
V_{ci} = b\left(\sum_i^n v_{ci,i} \sin\alpha_{cr,i} l_i - \sum_i^n n_{ci,i} \cos\alpha_{cr,i} l_i\right) \tag{6}
$$

3.4.3 Dowel action

The shear force related to dowel action is derived by considering an elastic beam fixed at both ends subjected to bending by the vertical displacement Δ_c. The upper bound of this component corresponds to the development of theoretical plastic hinges at both ends of the dowel. The capacity of the dowel takes explicitly into account the tension force already developed in the bar due to bending of the beam. The problem is that the dowel is considered to behave elastic-perfectly plastic, which is not the case for FRP bars. Therefore only the elastic contribution will be taken into account, up to rupture of the bar. The developed stress is determined with the following equations

$$
\begin{aligned}
M_d &= K_d \Delta_c \frac{l_k}{2} \\
K_d &= n_b \frac{12 E_{FRP} \pi d_b^4}{64 l_k} \\
N &= E_{FRP} A_{FRP} \varepsilon \\
\sigma &= \frac{N}{A_{FRP}} + \frac{M}{I_{FRP}} \frac{d_b}{2}
\end{aligned}
\tag{7}
$$

Finally, the shear contribution due to dowel action V_d is found with Eq. 8.

$$
\begin{aligned}
V_d = K_d \Delta_c \quad &\text{if} \quad \sigma \leq f_{FRP,u} \\
V_d = 0 \quad &\text{if} \quad \sigma > f_{FRP,u}
\end{aligned}
\tag{8}
$$

In the model, V_d is taken into account. However some hypothesis can be considered: FRP has a very low modulus of elasticity E_{FRP} and an increased value of l_k due to bond effects. Both of them result in a decrease of the stiffness factor K_d. Therefore, the shear contribution by dowel action will probably be very low in comparison to steel-reinforced deep beams and, possibly, completely negligible. This will be analysed in the results section.

3.5 Equilibrium and solution procedure

Now a solution is found by the following procedure: the first DOF Δ_c is chosen and will therefore be a control parameter. From this DOF, the second DOF Δ_{cx} is directly calculated. Mihaylov suggested a simplified approximation [27]: $\Delta_{cx} = 0.5\Delta_x cot\alpha_1$. Finally, an initial strain of 0.05 is assigned to the third DOF $\varepsilon_{t,avg}$, which will be recalculated at the end of the procedure. With the three DOFs known, all three shear contributions, the inclined compression in the critical loading zone V_{CLZ}, the aggregate interlock across the rough crack V_{ci} and dowel action V_d, are calculated.

The sum of these three internal shear mechanisms must be in equilibrium with the shear force induced by the tensile force in the bottom reinforcement $T(\varepsilon_{t,avg})$. The force in the reinforcement takes into account tension stiffening which is provided by an effective concrete area $A_{c,eff}$, defined according to EC2 [29]. The equations are shown in Eq. (9).

$$
\begin{aligned}
f_{ct} &= \frac{f_{ct}}{(1+(200\varepsilon_{t,avg})^{0.5}} \leq E_c\varepsilon_{t,avg} \\
A_{c,eff} &= b \cdot min\Big(2.5(h-d); h/2\Big) \\
T &= E_{FRP}A_{FRP}\varepsilon_{t,avg} + f_{ct}A_{c,eff} \\
V &= \frac{T0.9d}{a} = V_{CLZ} + V_{ci} + V_d
\end{aligned}
\tag{9}
$$

If the equilibrium condition $V = V_{CLZ} + V_{ci} + V_d$ is not satisfied, the DOF $\varepsilon_{t,avg}$ is iterated again by bisection method until equilibrium is reached as seen in Fig. 3.8. This procedure is repeated for increasing values of DOF Δ_c, ranging from zero until failure of the member, to obtain the full load-displacement response.

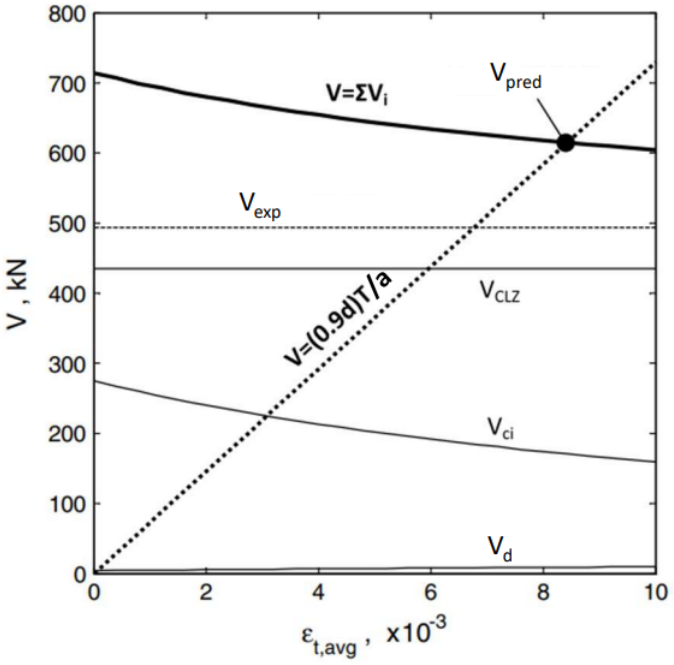

Figure 3.8: Solution procedure of crack-based 2PKT for FRP-reinforced deep beams (adapted from [23])

3.6 Modelling of shear-induced flexural crushing

Typically, diagonal shear cracks in deep beams subjected to four-point bending are developing diagonally from the inner side of the bearing plate to the loading plate. Such crack development was also observed in the tests of Andermatt and Lubell [8] (refer to Section 2.3.1), and Farghaly and Benmokrane [15] (refer to Section 2.3.2). However, in the former test series, most specimens exhibited diagonal cracking towards the applied point-loads up to failure, when the crack angle suddenly decreased. At this instance, the critical crack propagated almost horizontally in the compression zone, causing a premature failure of the specimen as shown in Fig. 3.9.

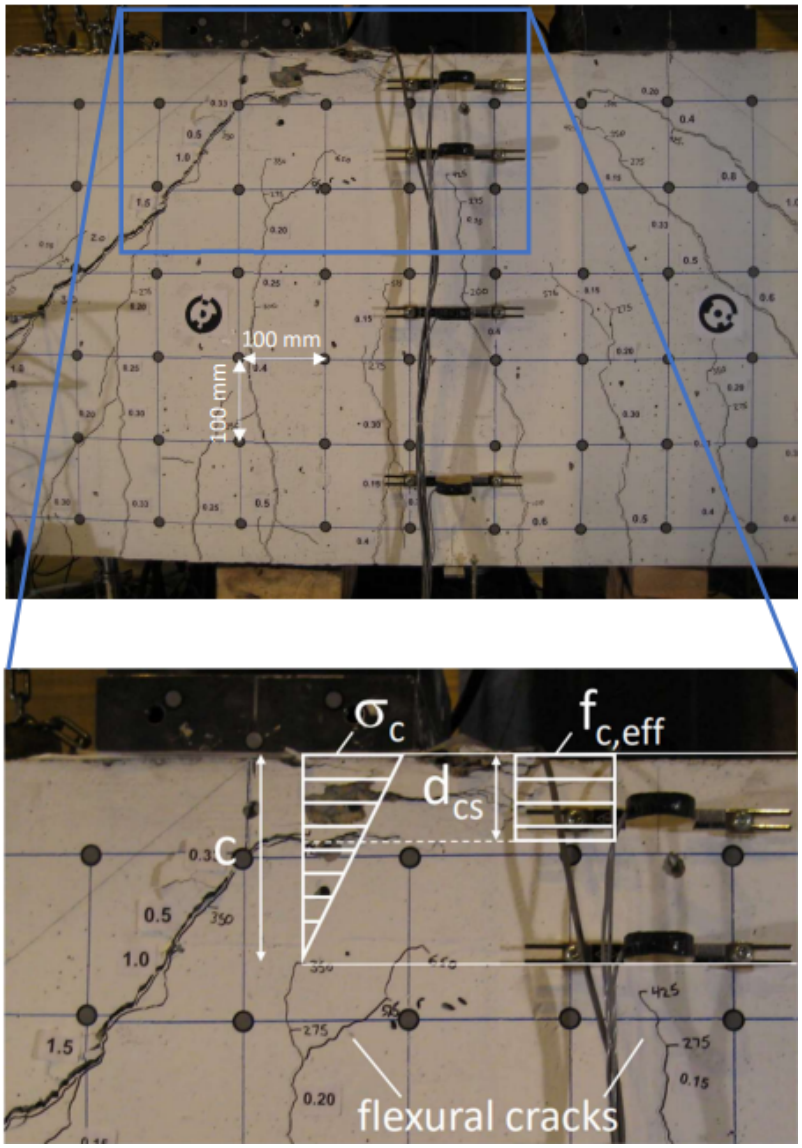

Figure 3.9: Shear-induced flexural crushing in specimen B2N and corresponding model properties (courtesy by Andermatt and Lubell, University of Alberta)

This type of crack propagation and failure mode is not typically observed in deep beams, because they are expected to fail by crushing of the concrete in the CLZ. However, this failure mode and crack pattern are observed in eleven out of twelve tests on FRP-reinforced deep beams performed by [8]. This observed behavior has strong similarities with a theoretical failure mode conceptualized by Kotsovos in 1984 [30]. The author derived this failure mode by stating that

the zone under the loading plate is in a multiaxial compressive state that caused a local increase of the concrete strength. Therefore, the diagonal crack is bypassing this high-strength region and penetrating horizontally in the compression zone of the pure flexural region. However, according to the local equilibrium condition, this is only possible by considering the presence of a resultant tensile force at right angles to the compressive path near the tip of the critical crack. Eventually, failure will occur within the pure flexural region under compression-stress conditions. Later, Salamy et al. [31] used shear reinforcement in the pure flexural region of a deep beam subjected to four-point bending to, successfully, prevent the occurrence of this theoretical failure mode. The failure mode was described by Salamy et al. [31] based on the eccentricity of the trust line that led to a flexural failure in the compression zone. They further formulated that the failure mode results from the extension of the tensile crack in the compressive zone. The reason for the sudden change of direction of the crack angle demands a complex answer. However, in a first instance, the goal of this model is to predict the behavior of FRP-reinforced deep beams by accounting explicitly for the observed failure mode. This failure mode was not previously considered in other kinematics-based approaches. To address this, additional modelling is proposed hereinafter.

When the upper region of a specimen is analysed in more detail, as showed in Fig. 3.9, several remarks can be made. First, there can be seen that the horizontal crack is penetrating into the pure bending region. In this region, flexural cracks have developed vertically from the bottom side of the specimen. The uncracked zone above these cracks is known as the compression zone with an estimated depth c. Further, there can be seen that the horizontal crack is penetrating into the compression zone and decreasing the depth of this zone. In the remaining area above the horizontal crack, the concrete is heavily crushed. This is most probably caused by high horizontal concentrated stresses.

It can be concluded that the specimen has failed due to crushing in the pure flexural zone, but due to a limitation of the compression zone induced by the horizontal propagation of the shear crack rather than a traditional sectional flexural failure. This directly explains the name of the failure mode: shear-induced flexural crushing. Accordingly, a possible approach to address the problem and, more importantly, to model this behavior, is using a bending moment analysis as in a conventional flexural analysis. The conventional flexural analysis uses the entire depth of the compression zone c to develop an elastic stress distribution with a maximal compressive stress σ_c in the top fiber of the section. This stress diagram can be transformed in a compression force working on the concrete section limited by the width of the beam and the depth of the compression zone. The compression force engages a bending moment with respect to the reinforcement. This moment is in equilibrium with the shear force engaged at the bearing plate at a distance a, the length of the shear span. However, in contrast with conventional sectional analysis, the area where the compression force can be developed is, for this failure mode, limited by the horizontal crack. Therefore, only the depth from the top of the beam to the horizontal crack can be used to carry compression. The depth of this zone corresponds to the depth of the crushed section d_{cs} as shown in Fig. 3.9. As a result, the same force needs to pass through a smaller section. It can be assumed that the concrete is now in the plastic region and can be represented by a plastic stress block governed by the concrete compressive strength as shown in Fig. 3.9. Therefore, a simplified plasticity-based model is presented in Eq. (10).

$$
\begin{aligned}
F_c &= d_{cs} f_{c,eff} b \\
M_{SIFC} &= F_c(d - \frac{d_{cs}}{2}) \\
V_{SIFC} &= \frac{M_{SIFC}}{a}
\end{aligned}
\tag{10}
$$

As can be seen in Eq. (10), the strength of the concrete is not defined as $f_c^{'}$. Instead, the concrete strength is defined as an effective concrete compressive strength $f_{c,eff}$. As suggested in literature [32], the behavior of concrete in compression can not be directly assumed as perfectly plastic. However, the exact behavior is a complex phenomenon which lead to the use of a number of strength reduction factors in the past. Therefore, in order to be consistent in all limit analyses, Moccia et al. [32] derived a strength reduction factor which takes into account the brittle behavior of concrete in compression. However, the brittle behavior is dependant on the concrete strength (high strength concrete behaves more brittle) which implies that the value of $f_{c,eff}$ is not constant. Therefore, must $f_{c,eff}$ be determined by multiplying the concrete strength $f_c^{'}$ with a brittleness factor $\eta_{fc} = (30/f_c)^{1/3} \leq 1$ [32].

The final remark concerns the depth of the crushed section d_{cs}. As discussed in Section 2.3.1 and Section 2.3.2, the development of the diagonal shear crack appears already at a low loading stage. However, the penetration of the crack under the loading plate has been observed to happen in a later stage, closer to failure. Therefore, a predictive equation, to estimate the depth of the crushed concrete section d_{cs}, is proposed. Further on, this equation is compared with experimental observations for validation purposed.

From the discussion above, it is clear that the depth of the crushed concrete section d_{cs} and the depth of the compression zone c are related. Therefore, in a first instance, the depth of the compression zone c is approximated with Eq. (11) which assumes an elastic behavior of the materials.

$$
c = (\sqrt{n^2\rho_l^2 + 2n\rho_l} - n\rho_l)d \tag{11}
$$

Where $n = E_{FRP}/E_c$ represents the ratio of the stiffness of the reinforcement to the concrete and $\rho_l = A_{FRP}/bd$ is equal to the reinforcement ratio.

To validate the proposed equation, a direct measurement is performed on high-resolution pictures of the experiment which clearly showed the crushed zone in comparison to the compression zone. In Fig. 3.9, there can be seen that the depth of the compression zone c is around 110 mm (reference length: size of grid is 100x100mm). Eq. (11) predicts a depth of 105 mm which is almost equal. The same validation was done for other specimens, and the results showed the same good predictions. In other words, the results of the proposed equation are confirmed by experimental observations.

By analysing the specimens that failed in SIFC, a correlation was found between the ratio d_{cs}/c as a function of a/d and $f_{c,eff}$. To normalise the concrete strength, $f_{c,eff}$ was divided by 30, similarly to the brittleness factor. This resulted in the relationship shown in Eq. (12) and illustrated in Fig. 3.10.

$$
\frac{d_{cs}}{c} = 1 - 0.24\frac{a}{d}\frac{f_{c,eff}}{30} \tag{12}
$$

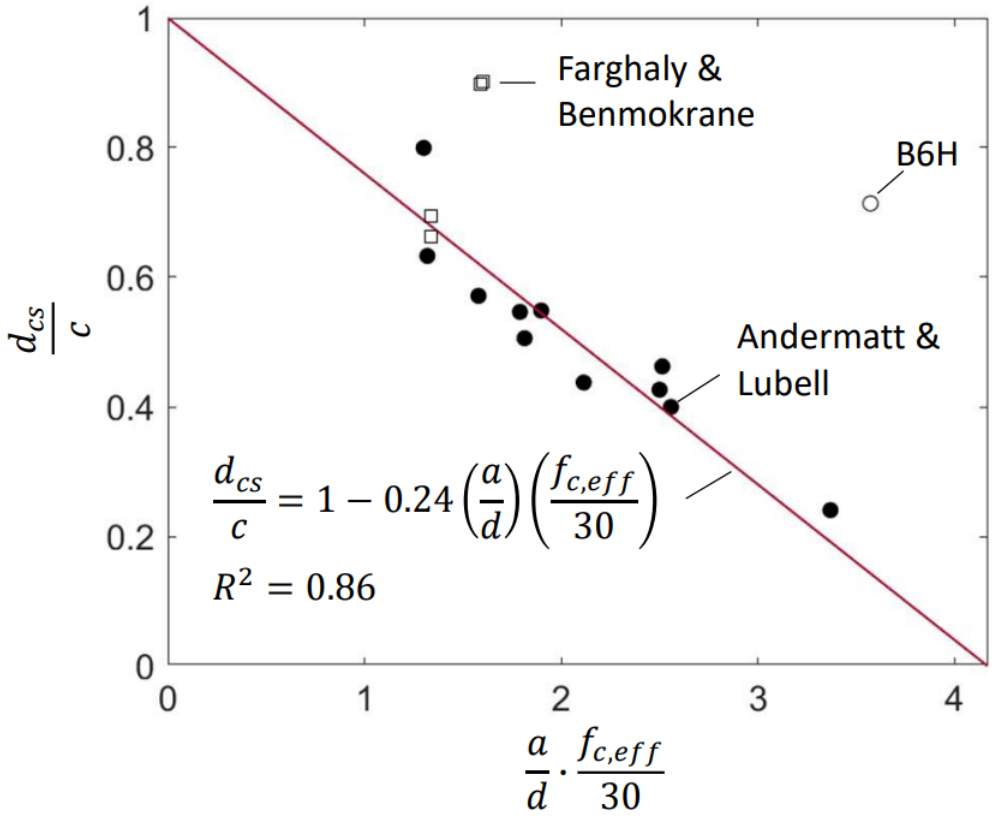

Figure 3.10: Linear correlation of the crushed-to-compressed depth ratio to a/d and $f_{c,eff}$

It can be seen that all specimens which failed in shear-induced flexural failure are very close to the linear correlation (solid dots). However, specimen B6H is not well correlated with the proposed linear function because it exhibited a different failure mode. This failure mode will be further discussed in the next section. Therefore, it is justified to develop the relationship between the crushed-to-compressed depth, and the geometrical and material properties (aspect ratio and concrete compressive strength) based only on specimens which exhibited shear-induced flexural failure considering that the predicted and observed geometrical parameters of the model are in very good agreement. This suggests that the assumptions behind the proposed model and equations are physically-sound. For convenience, predictions of the crushed-to-compressed depth for the specimens tested by Farghaly and Benmokrane [15] are shown (hollow squares). As evident from the plot, the specimens featuring GFRP reinforcement are not well correlated with the employed parameters, while the beams featuring CFRP reinforcement lay on the prediction curve. Nevertheless, it is important to mention that none of the four specimens tested by [15] exhibited SIFC. These aspects will be discussed later in the manuscript.

With the proposed relationship $d_{cs} = c\Big(1 - 0.24(a/d)(f_{c,eff}/30)\Big)$ the depth of the crushed section d_{cs} can be predicted just with simple geometrical and material properties. The presented approach provides a simple and rational basis to predict the capacity corresponding to this failure mode.

3.7 Modelling of cracking of critical loading zone

The failure mode, cracking of the critical loading zone, occurred only in specimen B6H. After the flexural cracks had formed, the shear crack did not develop from bearing plate to loading

plate along a diagonal path as it was observed in other specimens. Instead the crack developed first slightly under and then above the diagonal line such in the form of an S-shaped crack, see Fig. 2.7b. The crack reached the CLZ under a relatively flat angle.

Once-more, this type of crack propagation is not typical for deep beams. Although, a failure mode with some similar aspects has been conceptualized by Cavagnis et al. [33] and Fernandez Ruiz et al. [34] and has been observed in tests a few times in the past [11].

The reason for the S-shaped crack to form is mostly related to the a/d ratio of 2.06, which is in the transition region between slender beams and deep beams. These cracks are more typically observed in slender beams. One of the interesting questions is to understand why it occurred in this particular deep beam. However, the goal of the model is to predict the behavior of FRP-reinforced deep beams.

When the beam is analysed more in detail, there can be seen that besides the huge opening of the S-shaped crack, an almost vertical crack developed in the vicinity of the CLZ at the top side of the beam. This crack seems to have been initiated due to excessive tensile stresses at the top of this area, and, induces the failure of the CLZ cantilever due to excessive tension at the top face. Therefore, this failure mode is defined as cracking of the critical loading zone.

The observed behavior can be approached with an elastic beam model applied on a variable-depth elastic cantilever fixed at one end and loaded at the other, as previously proposed by Mihaylov [11]. According to this model, plane sections perpendicular to the bottom face of the cantilever remain plane and the tip section, defined as d_{CLZ}, is subjected to uniform compressive stresses. The following step is to determine which forces, responsible for these stresses, are acting on the cantilever. This cantilever, subjected to a vertical force, is rotating around its fixed end. There can be understood that due this rotation, the crack widths are varying. These crack widths are directly proportional to the aggregate interlock shear force: when crack widths increase, the aggregate interlock decreases. To simplify the model, the contribution of aggregate interlock is neglected, which is conservative. Furthermore, as suggested before, the contribution of dowel action is most probably small in comparison to other shear contributions and, therefore, this shear mechanism is also neglected in the model. This means that the only force acting on this cantilever section, is the shear force carried by the CLZ, which is applied at the center of the d_{CLZ}. From the applied force, the elastic stresses in inclined sections along the span of the cantilever can be derived from basic mechanics. As suggested before, when the stress in this top fiber exceeds the tensile strength of concrete, a vertical crack forms, and, the beam exhibits a CLZ cracking failure. The geometrical parameters used to formulate this model are presented in Fig. 3.11.

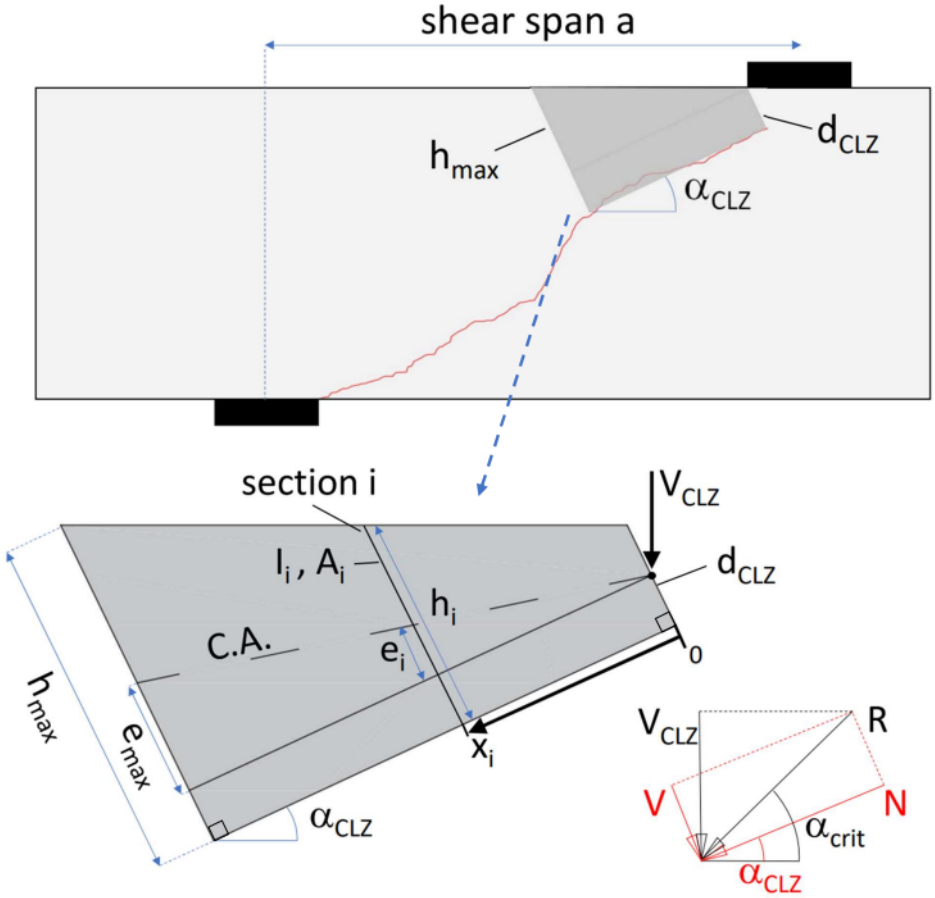

Figure 3.11: Geometrical model for cracking of critical loading zone

The first assumption to address is how to define the geometry of the cantilever and, more importantly, where to check the stresses. In this model, it is opted to check stresses on inclined sections perpendicular to the axis x defined by the angle of the critical loading zone α_{CLZ}. This angle is determined with the crack-based geometry of the CLZ as discussed in Section 3.4.1. The position of the section where the maximal stress develops is not as easy to derive due to the fact that the sections are inclined which implies varying geometrical parameters such as the position of the centroidal axis (C.A.), the eccentricity e, the depth h, the area A, and the moment of inertia I. However, there can be assumed that the maximal stresses will not develop further than half of the shear span. Therefore, the stress check is performed on every section starting from d_{CLZ} to mid shear span, which corresponds to the section with the maximal height h_{max} as shown in Fig. 3.11.

Having defined the geometry, the next step is to transform the forces into stresses. The objective is to project the vertical force V_{CLZ} on the inclined sections, but this can not be done directly. Due to the assumption that the aggregate interlock (and dowel action) is negligible, there must be a resultant force passing through the intersection point of the center of the bearing plate and the reinforcement due to equilibrium conditions. This resultant force R is inclined under angle $\alpha_{crit} = atan(d/a)$. However, as said before, the forces orthogonal to the inclined section, the shear force V and the normal force N, are needed, and, therefore the resultant force R is projected on the inclined plain with an angle equal to $\alpha_{crit} - \alpha_{CLZ}$ as can be seen in Fig. 3.11. With the known orthogonal forces are known, the stresses acting on the inclined sections are derived as shown in Fig. 3.12.

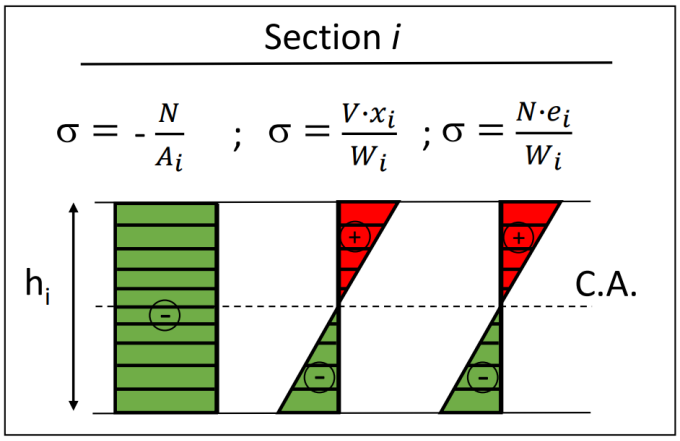

Figure 3.12: Three stress contributions developing in a section i

It can be seen that there are three stress contributions: the first one is induced by the compression force N, the second one is due to the shear force V and the third one comes from the moment developed due to the eccentricity e of the compression force N. As said before, the stress check is performed at the top fiber of the specimen. Therefore, the sum of the three contributions is taken and compared to the tensile strength of concrete. This results in Eq. (13).

$$\begin{aligned} \sigma_{top,i} &= -\frac{N}{A_i} + \frac{Vx_i}{W_i} + \frac{Ne_i}{W_i} \\ \sigma_{bottom,i} &= -\frac{N}{A_i} - \frac{Vx_i}{W_i} - \frac{Ne_i}{I_i} \end{aligned} \tag{13}$$

where $W_i = \frac{h_i}{2}$. As can be seen from the geometrical definition of this zone in Fig. 3.11, the area A, the moment of inertia I, the height h and the eccentricity e are varying along the sections. The definition of the area and moment of inertia are straightforward for a rectangular section defined by the the width of the beam b and the height of the inclined section h. The eccentricity e for a section i can be found by trigonometry: $e_i = \frac{h_i}{2} - \frac{d_{CLZ}}{2}$.

Finally, the calculated stress at the top fiber can be compared to the tensile strength of concrete. For normal-strength concrete, the tensile strength is estimated by $f_{ct} = 0.3 f_c'^{2/3}$ found in EC 2 [29], while for high-strength concrete as $f_{ct} = 0.3(50 f_c'^{1/3})$ according to [33] and [35]. In literature, numerous ways to predict the tensile strength of concrete are presented. It is of interest to analyse in the results section to which extent this parameter is influencing the results.

The only parameter that is yet to be defined is the magnitude of the force V_{CLZ}. This force is already known in function of the kinematics obtained by the crack-based 2PKT. Therefore, the stresses are checked for the full envelope of V_{CLZ}. If the tension limit is reached for a certain avlue of V_{CLZ}, the total shear strength is derived by adding the corresponding V_{ci} to V_{CLZ} obtained with the crack-based 2PKT. If the tension limit is not reached, the behavior of the CLZ is not governed by cracking, and therefore the failure mode will not occur.

3.8 Implementation of the failure modes in the 2PKT framework

The models for shear-induced flexural crushing and cracking of the CLZ are implemented within the crack-based 2PKT code. More precisely, the crack-based 2PKT is used to calculate the complete shear response up to failure. However, the predicted failure load of the specimen is not necessarily determined by crushing of the CLZ, as the failure load is considered to be the minimum peak resistance generated by the three failure modes.

Therefore, the outcome of the model is the complete predicted load-deformation response, which accounts for the measured crack, as well as different failure modes. This procedure is illustrated in Fig. 3.13 for specimen B4N.

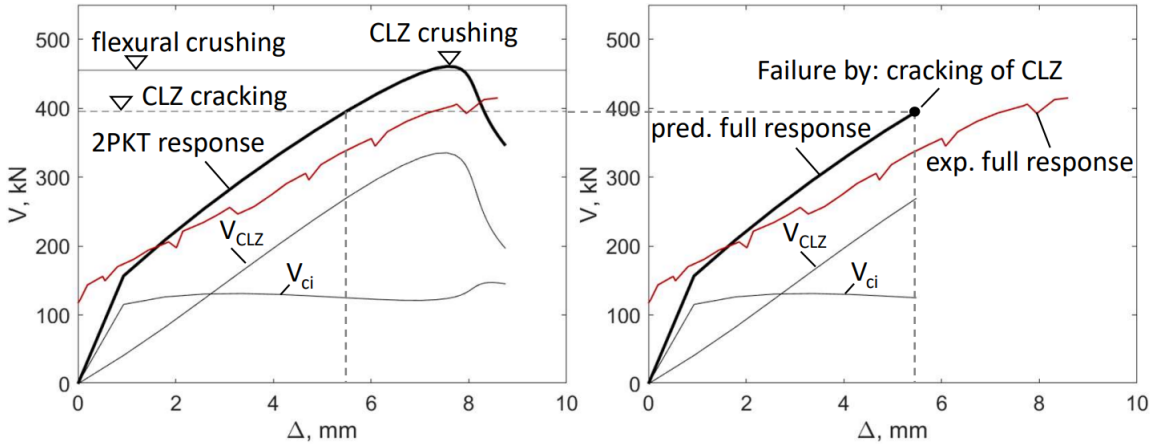

Figure 3.13: Full response as a function of three possible failure modes determined with crack-based 2PKT for FRP-reinforced deep beams, specimen B4N

3.9 Modelling of flexural deformations in pure bending regions

The crack-based 2PKT is designed to predict the deflections of the shear span. However, all test specimens that are analysed in this work were subjected to symmetrical four-point bending which has a pure bending region between the two applied forces. In four-point bending, an additional deformation occurs in the pure bending region between the applied point loads. Therefore, the experimental deflections are modified such that the results are comparable to the predictions. The procedure is based on the method presented by Mihaylov [27].

First, Eq. (11) is used to predict the depth of the compression zone c. This equation is already introduced in a previous section (refer to Section 3.6). It is used to calculate the depth of the compression zone in the pure flexural region. With this depth, the cracked moment of inertia $I_{cr} = bc^3/3 + nA_{FRP}(d-c)^2$ can be derived. Finally, the constant curvature ϕ in this pure bending region is estimated by Eq. (14).

$$\phi = \frac{V_{exp}a}{E_c I_{cr}} \tag{14}$$

The curvature ϕ, constant over the length l_f between the loading plates, contributes to the midspan deflection as shown in Eq. (15).

$$\Delta_{exp,mod} = \Delta_{exp} - \phi\left(\frac{l_f^2}{8} + \frac{l_f a}{2}\right) \tag{15}$$

So, to obtain the shear span deflection, the deformation of the pure bending region is subtracted from the experimental deflection measured at mid span.

4 Results and discussion

In the following sections, the results will be presented in detail. For both testing series, each specimen will be analysed separately, while different specimens will be compared against others to determine the effects of variables on the capacity later in the paper.

The goal is to present and discuss results which are valuable and contribute to the understanding of the model and the specimens. Therefore, the following decisions are made:

- some displacement data measured during the tests by linear variable differential transformer (LVDT) were not available and therefore no comparison could be made between experimental and predicted crack widths for some experiments;
- the shear by dowel action was taken into account in the model, but the results showed that the shear contribution was less then 1% of the final shear capacity, even for CFRP which has a stiffness more comparable to steel. This is in line with the hypothesis that was stated in Section 3.4.3. Therefore, the contribution can be neglected and will not be presented in the results;
- the tests performed by [15] featured sufficient top reinforcement to suppress the failure due to cracking of the CLZ, and thus this failure mode is not considered for specimens G8N6, G8N8, C12N3 and C12N4;
- in the test program of Farghaly and Benmokrane [15], the only available data concerning the local displacements was the crack width measured under an angle of 45°. Therefore, the predicted horizontal and vertical crack displacement were projected to obtain orthogonal crack displacements under a 45° angle to allow for a direct comparison to the experimental measurements.

4.1 Tests by Andermatt and Lubell (2010)

4.1.1 Predictions of global and local shear behavior

A1N

In Fig. 4.1, the predicted (bolt black) and the experimental (thin red) load-displacement response of specimen A1N are presented.

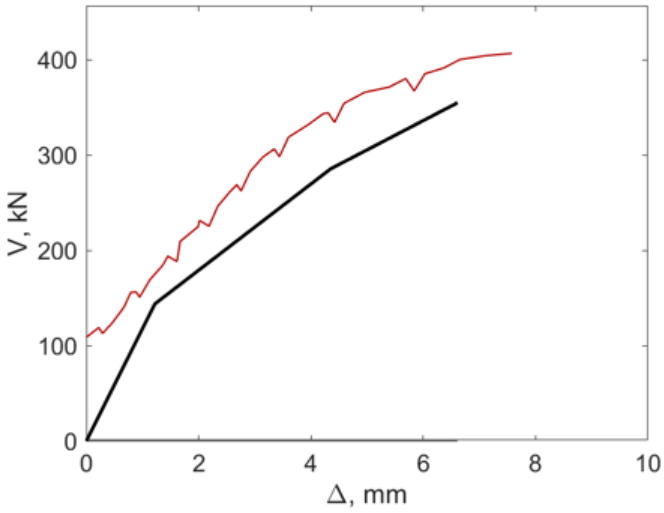

Figure 4.1: Experimental and predicted load-displacement response for specimen A1N

Firstly, the predicted failure mode for specimen A1N is shear-induced flexural crushing which corresponds well with the experimental observations as can be seen in Fig. 4.2. The predicted failure load is 355 kN, while the experimental strength was 407 kN. The ratio $V_{exp}/V_{pred} = 1.15$ shows a underestimation of 15% of the capacity. This is probably influenced by the small depth of the specimen. There can also be seen that there shear is carried entirely by the contribution of V_{CLZ} which means that the aggregate interlock is non-existent. Therefore, an underestimation of the aggregate interlock may be a possible explanation for the underestimated failure load. Another interesting conclusion is that the predicted deflection of around 6.5 mm is similar to the experimental deflection of 7.5 mm. Both responses exhibit the same slope which indicates that the stiffness of the beam, after diagonal cracking, is correctly predicted.

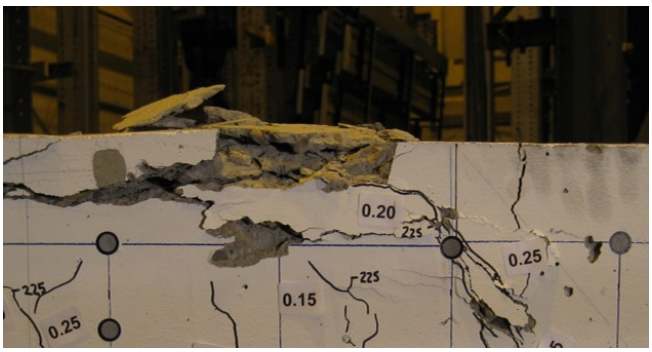

Figure 4.2: Shear-induced flexural crushing in specimen A1N (courtesy by Andermatt and Lubell, University of Alberta)

Next, the predicted strain in the FRP reinforcement is compared to the average strain of the reinforcement along the shear span during the experiment. The results are shown in Fig. 4.3.

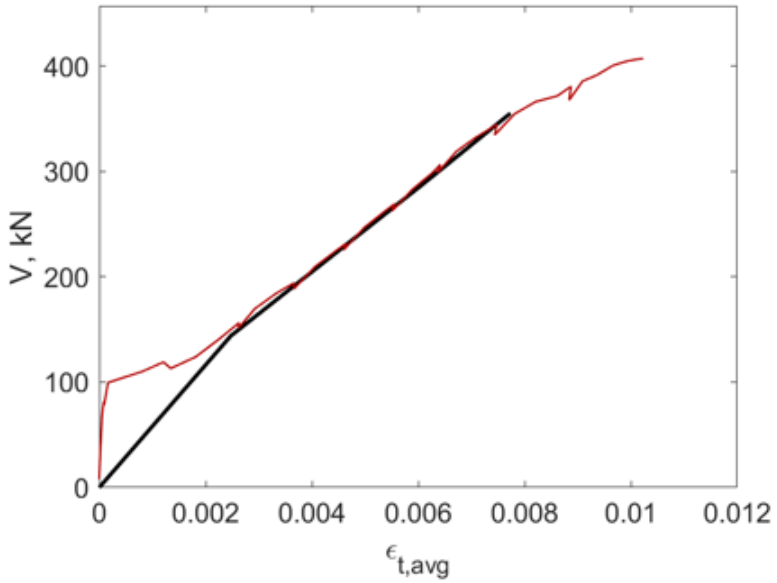

Figure 4.3: Experimental and predicted load-strain response for specimen A1N

There can be seen that the strain development in the FRP bar during the test is predicted almost perfectly. The difference in the beginning of the response is due to a assumption of the

model: 2PKT assumes a cracked section from the start, while the specimen only exhibit flexural cracks when a load of 100 kN has been reached. Although the underestimation of the capacity also lead to an underpredicted strain at failure, both the experimental and predicted response demonstrate the same thing: the strain at peak resistance is around 8×10^{-3} to 10×10^{-3}, which is a very high strain in comparison to conventional steel where the elastic strain limit is around 2×10^{-3}.

Finally, the horizontal and vertical displacement at the position of the LVDT-rosette are predicted as shown in Fig. 4.4.

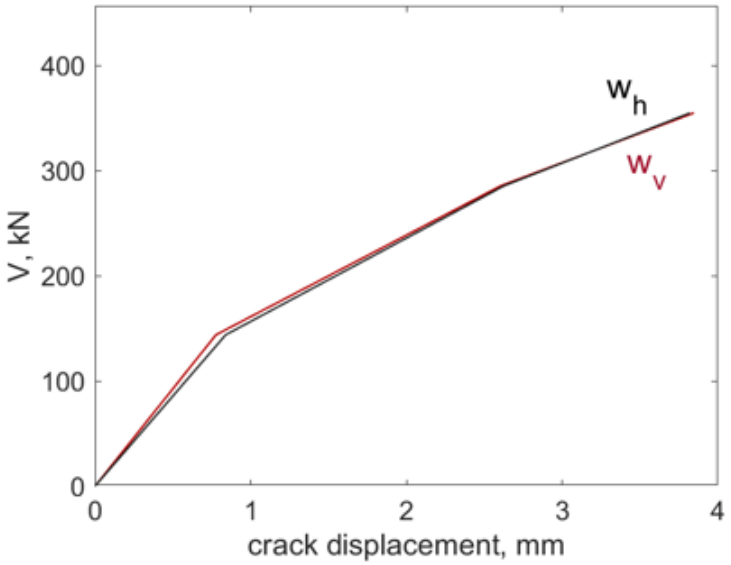

Figure 4.4: Experimental and predicted load-crack displacement response for specimen A1N

There can be seen that the horizontal and vertical crack displacement reach almost 4 mm which is very high for a specimen with a relatively small depth. They can not be compared with the experimental ones, because the LVDTs stopped registering during the tests. Furthermore, as can be seen in the results of the following specimens, the vertical crack displacement is for most of the predictions larger than the horizontal one. However, for specimen A1N, both displacements are almost equal. The reason why these values are very close, is possibly the result of a combination of factors: firstly, the depth of a specimen is directly proportional to the kinematics in the crack-based 2PKT. For a small specimen, the DOF Δ_c has not increased very much until failure occurs. This means that, in correspondence with Eq. (2), the vertical and horizontal displacement will both be mainly determined by the DOFs $\varepsilon_{t,avg}$ and Δ_{cx}, where Δ_{cx} is proportional to Δ_c, thus will also be very small. The only remaining DOF to consider is thus $\varepsilon_{t,avg}$, which is equal in both cases. Secondly the angle of the crack plays a role in how the displacements are distributed in horizontal and vertical direction. However, specimen A1N has shear span-to-depth ratio of almost 1, which means that the diagonal crack propagates theoretically under an angle of 45° which results Once-more in a equal crack displacement in the horizontal and vertical direction. The combination of these two effects, lead to an (almost) similar load-crack displacement response in the horizontal and vertical direction.

A2N

The experimental and predicted load-displacement response of specimen A2N are presented in Fig. 4.5.

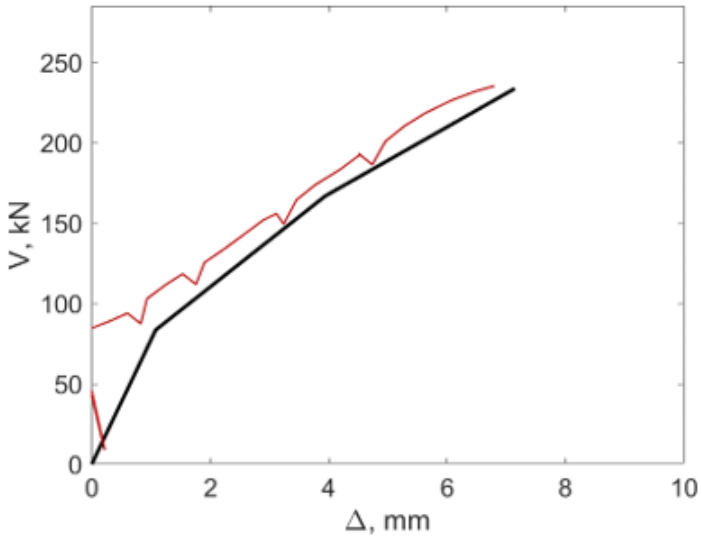

Figure 4.5: Experimental and predicted load-displacement response for specimen A2N

Specimen A2N is predicted to fail by shear-induced flexural crushing which corresponds well with the experimental observations as can be seen in Fig. 4.6. Furthermore, the experimental and predicted response in Fig. 4.5 are identical: the predicted failure load of 234 kN is practically equal to the experimental load of 235.5 kN, the predicted deflection of around 7 mm is equal to the experimental one and the stiffness of the responses are parallel. There can also be seen that, similar to specimen A1N, there is only a shear contribution from V_{CLZ}.

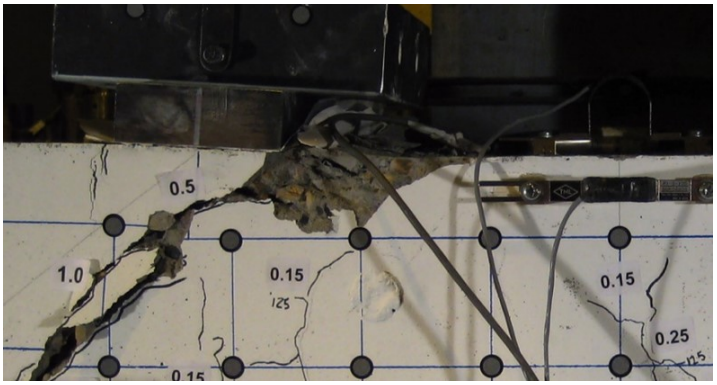

Figure 4.6: Shear-induced flexural crushing in specimen A2N (courtesy by Andermatt and Lubell, University of Alberta)

Next, the predicted strain is compared with the experimental strain in the FRP reinforcement in Fig. 4.7.

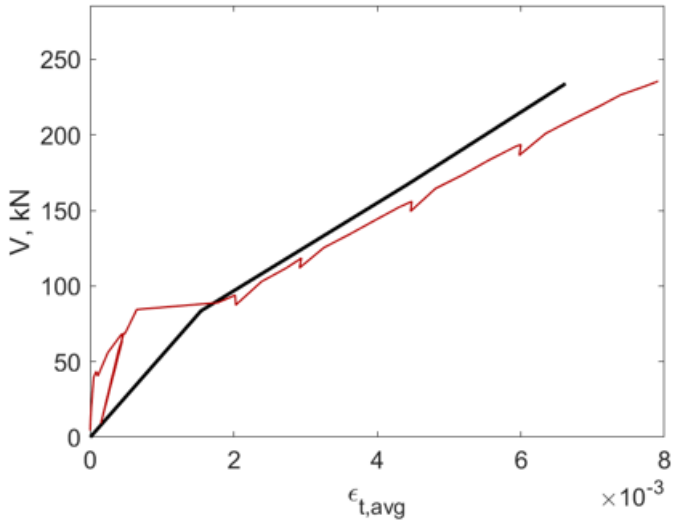

Figure 4.7: Experimental and predicted load-strain response for specimen A2N

The predicted strain of almost 7×10^{-3} is very close to the experimental one of 8×10^{-3}. As can be seen in Fig. 4.7, the stiffness of the predicted response is almost parallel to the experimental stiffness after flexural cracking.

Finally, the horizontal and vertical displacement at the position of the LVDTs are predicted as shown in Fig. 4.8.

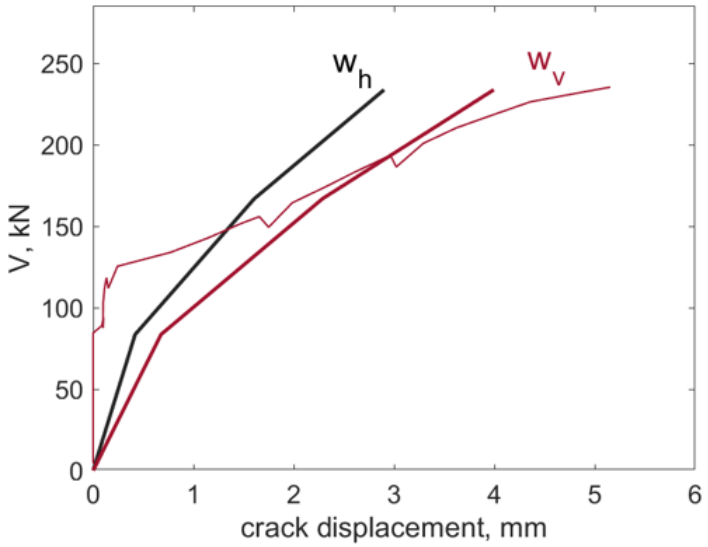

Figure 4.8: Experimental and predicted load-crack displacement response for specimen A2N

The predicted horizontal crack displacement (bold black) reaches 3 mm. This can not be compared to the test results because the data measurement was interrupted. At failure, the maximum vertical crack displacement (solid red) is equal to 4 mm, which is a little bit lower than the experimental (thin red) value of almost 5 mm. The slope of the experimental vertical displacement is underestimated by the predicted response.

A3N

The predicted and experimental load-displacement response of specimen A3N are presented in Fig. 4.9.

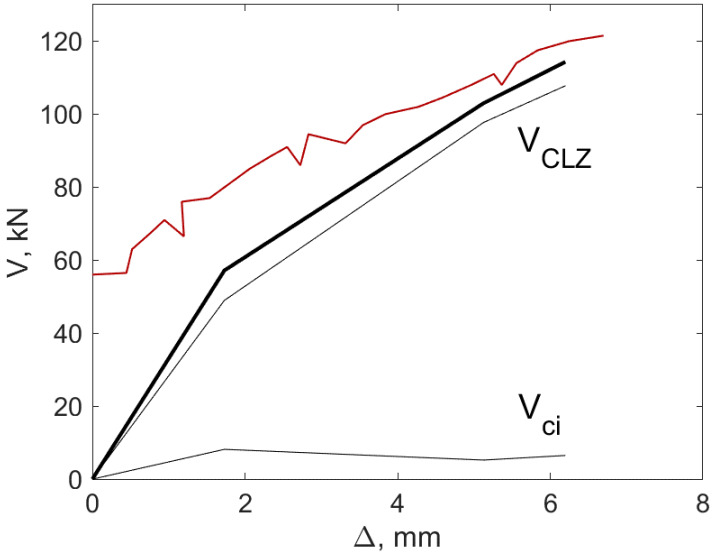

Figure 4.9: Experimental and predicted load-displacement response for specimen A3N

Shear-induced flexural crushing is predicted to happen in specimen A3N which corresponds well with the experimental observations as can be seen in Fig. 4.10. The predicted failure load (bold black), 114 kN, only just underestimates the experimental failure load (thin red) of 121.5 kN, by 7%. Further, there is a shear contribution by aggregate interlock V_{ci}, but it is only responsible for a small contribution of around 5% of the shear capacity. Finally, the deflection at mid span, equal to 6.5 mm, is predicted almost perfectly.

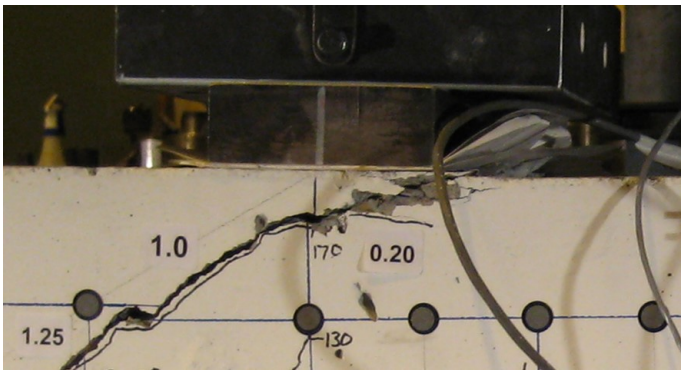

Figure 4.10: Shear-induced flexural crushing in specimen A3N (courtesy by Andermatt and Lubell, University of Alberta)

Next, the predicted strain is compared with the experimental strain in Fig. 4.11.

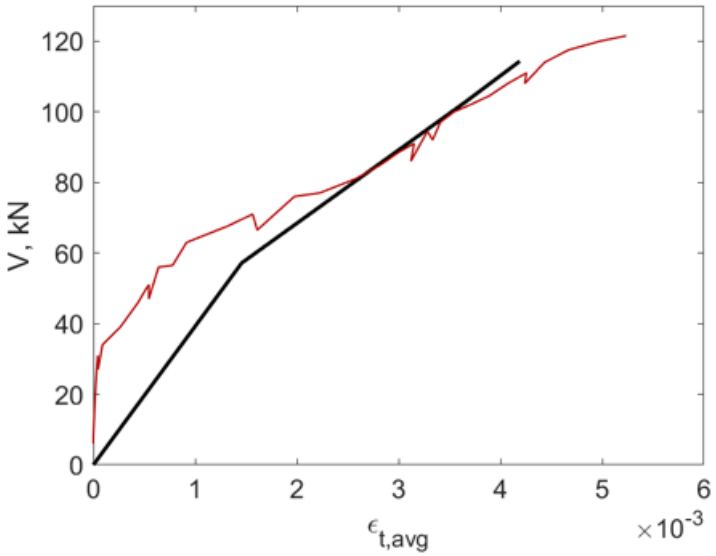

Figure 4.11: Experimental and predicted load-strain response for specimen A3N

For this specimen, the maximum predicted strain is equal to 4×10^{-3} while the experimental strain was slightly larger and equal to 5×10^{-3}. However, this is directly correlated with the underestimation of the capacity. The general form of both responses is very similar, although the stiffness seems to be slightly overestimated.

Finally, the horizontal and vertical displacement at the position of the LVDT-rosette are predicted as shown in Fig. 4.12.

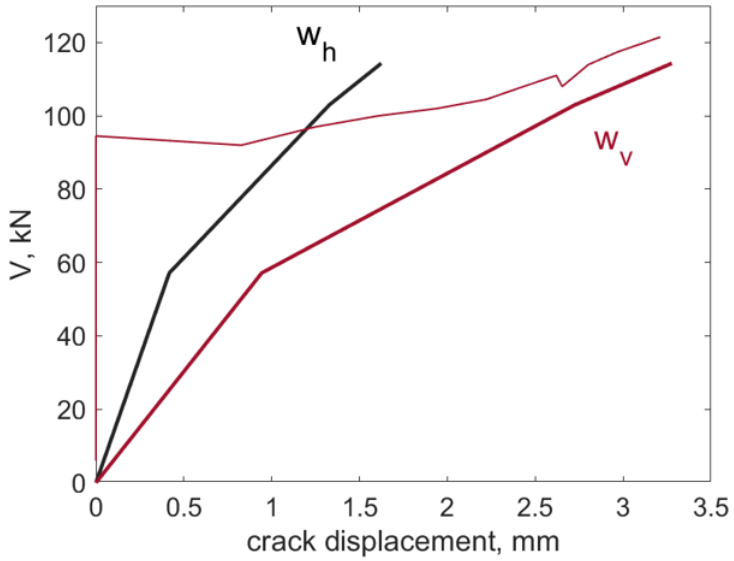

Figure 4.12: Experimental and predicted load-crack displacement response for specimen A3N

The data measurement of the horizontal crack displacement was interrupted. The predicted maximal horizontal crack displacement is equal to 1.5 mm. Further, the maximum vertical crack displacement is equal to the experimental one which was slightly larger than 3 mm. Although the first part of the experimental horizontal displacement seems non-physical, in the last part, the experimental vertical crack displacement seems to be almost parallel with the predicted one.

A4H

The experimental and predicted load-displacement response of specimen A4H are presented in Fig. 4.13.

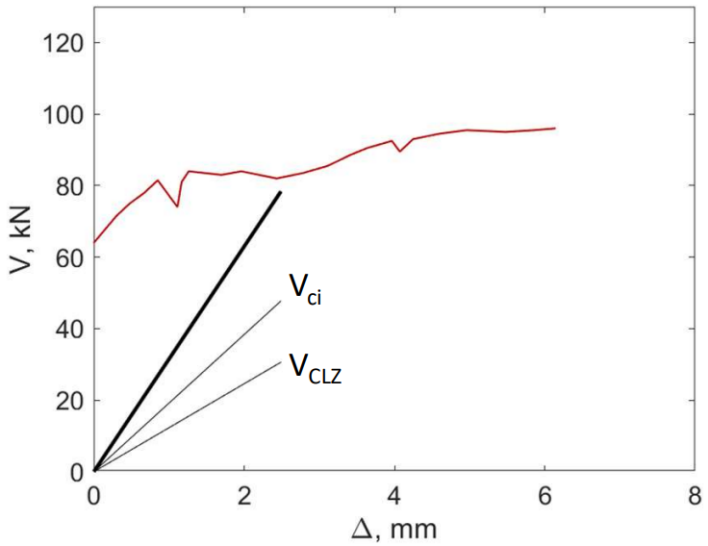

Figure 4.13: Experimental and predicted load-displacement response for specimen A4H

The predicted failure load is equal to 78 kN, while the experimental one is 96 kN, this results in a ratio $V_{exp}/V_{pred} = 1.23$. In other words, the experimental value is underestimated by 23%. This ratio needs to be analysed with care due to several factors. As discussed before, specimen A4N featured the smallest depth of the test serie, is made out of high strength concrete and has the largest a/d ratio, equal to 2.1, of all specimens. All three are inconvenient for obtaining consistent and reliable results, especially, when they are combined together. Furthermore, 23% is relative to the failure load which was only 96 kN. The precision of tracking the crack geometry, the accuracy of predicting material properties and conservative choices in the model can all lead to a difference of several kilo newtons. These effects are always present in absolute values, but on a relative scale, they make the largest difference for specimens with a low failure load.

Next, the predicted failure mode is shear-induced flexural crushing which corresponds well with the experimental observations as can be seen in Fig. 4.14. For this specimen almost two-thirds of the total shear capacity is induced by aggregate interlock V_{ci}. This can be explained by the fact that the crack widths are still small when the specimen failed as can be seen in Fig. 4.15. From the other hand, the shear contribution of the CLZ is gradually increasing, but did not had the time to develop completely due to early failure. This early failure also played a role in the deflection which was underestimated by 4 mm.

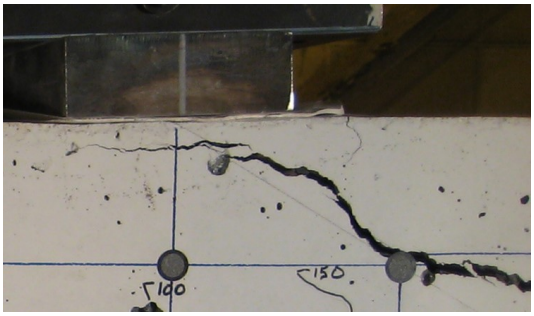

Figure 4.14: Shear-induced flexural crushing in specimen A4H (courtesy by Andermatt and Lubell, University of Alberta)

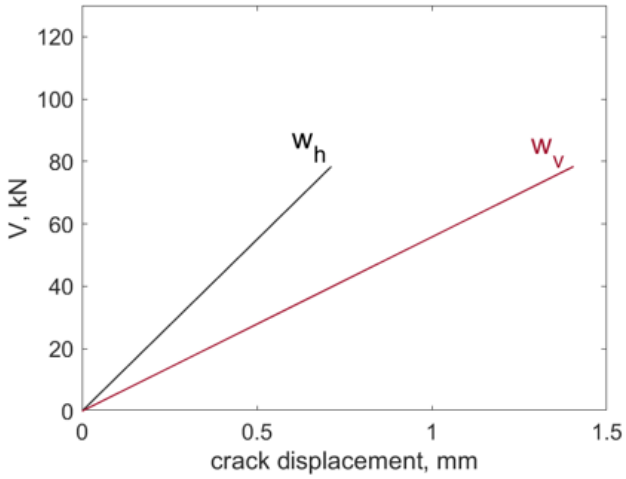

Figure 4.15: Experimental and predicted load-crack displacement response for specimen A4H

Next, the predicted strain is compared with the experimental strain in the FRP reinforcement in Fig. 4.16.

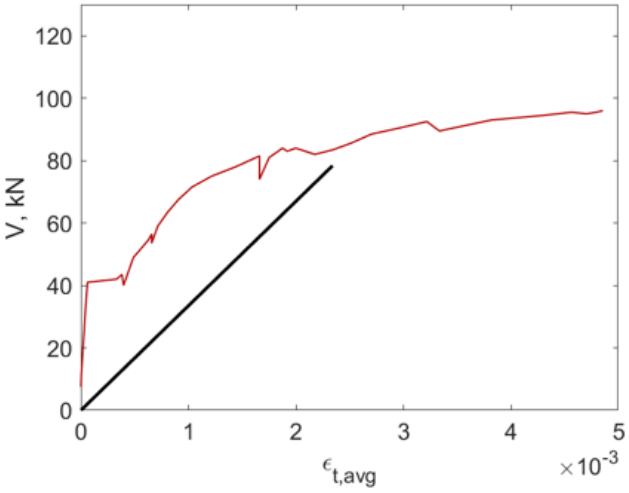

Figure 4.16: Experimental and predicted load-strain response for specimen A4H

The predicted strain (thin red) differs from the experimental strain (bolt black), but it is rather hard to take a conclusion due to early failure of the specimen.

B1N

The experimental and predicted load-displacement response of specimen B1N are presented in Fig. 4.17.

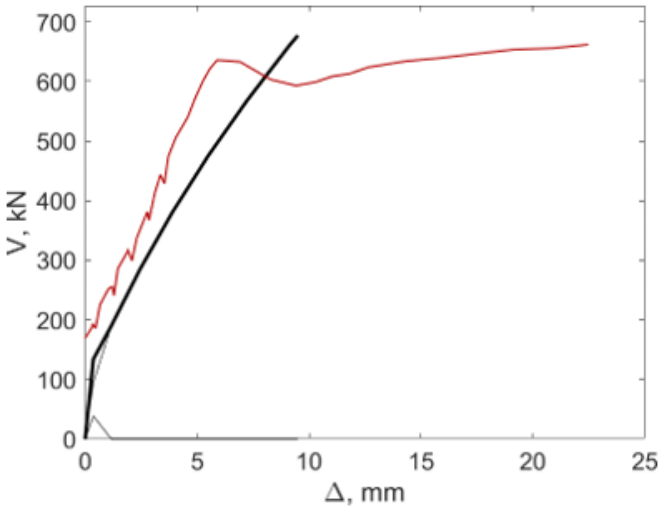

Figure 4.17: Experimental and predicted load-displacement response for specimen B1N

Specimen B1N is predicted to fail by shear-induced flexural crushing which corresponds well with the experimental observations as can be seen in Fig. 4.18. The experimental response (thin red) in Fig. 4.17 shows that the specimen exhibited creep behavior during the test. After the maximal load is reached, the deformation keeps increasing for an almost constant load. In terms of modelling precision, this behavior is not relevant to define the capacity and corresponding deflection of the beam. Values at peak capacity need to be compared. The predicted failure load of 677 kN is close to the experimental load of 636.5 kN. This means an overprediction of 6%. At failure, there is only a shear contribution from V_{CLZ} which is probably related to the big crack displacements (see Fig. 4.20). Furthermore, the predicted deflection is equal to 9 mm which slightly overestimates the experimental deflection of 6 mm. In general, the slopes of both responses are very close, although the stiffness is slightly underpredicted.

Figure 4.18: Shear-induced flexural crushing in specimen B1N (courtesy by Andermatt and Lubell, University of Alberta)

Next, the predicted strain is compared with the experimental strain in the FRP reinforcement in Fig. 4.19.

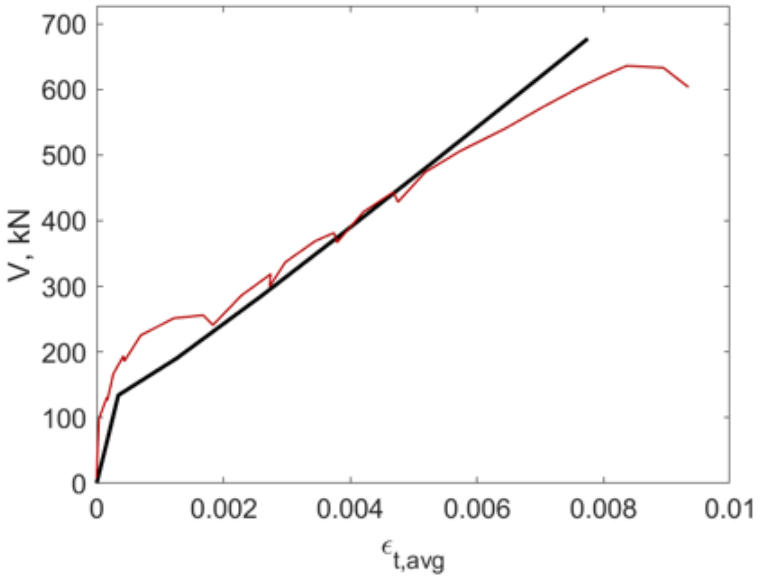

Figure 4.19: Experimental and predicted load-strain response for specimen B1N

The predicted strain is very close to the experimental one with a maximum strain of around 8×10^{-3}. Both responses are almost identical.

Finally, the horizontal and vertical crack displacement at the position of the LVDTs are predicted as shown in Fig. 4.20.

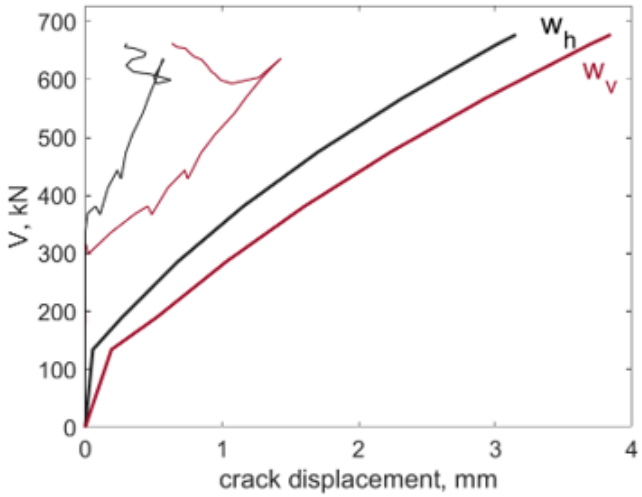

Figure 4.20: Experimental and predicted load-crack displacement response for specimen B1N

The maximal horizontal crack displacement reaches 3 mm and the maximum vertical crack displacement is equal to 4 mm. Both predictions are three to four times higher than the experimental ones. However, the predicted vertical response seems to be parallel to the experimental vertical displacement while the slope of the predicted horizontal crack displacement is lower than the corresponding experimental one.

B2N

The experimental and predicted load-displacement response of specimen B2N are presented in Fig. 4.21.

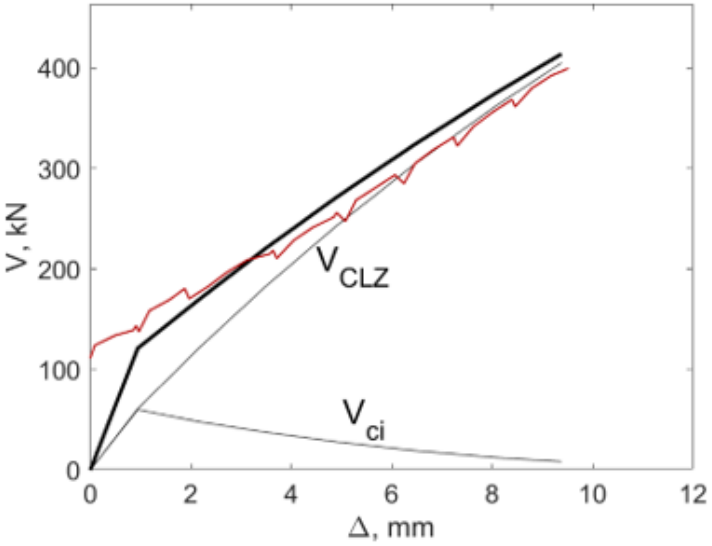

Figure 4.21: Experimental and predicted load-displacement response for specimen B2N

The predicted failure mode is shear-induced flexural crushing which corresponds well with the experimental observations as can be seen in Fig. 4.22. The predicted response in Fig. 4.21 is almost similar to the experimental response, they both exhibit the same stiffness. The predicted failure load of 414 kN slightly underestimates the experimental load of 399.5 kN by 4% and the experimental deflection of 10 mm is predicted very accurately. At failure, it can be stated that only the critical loading zone is contributing to the shear capacity, which means that the increased crack widths prohibited the aggregate interlock to carry shear.

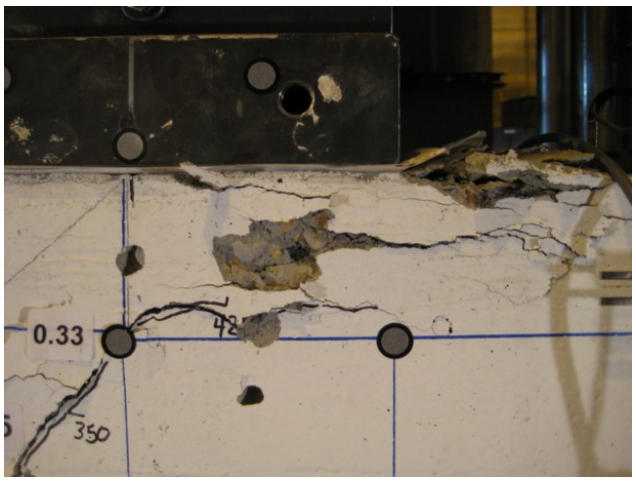

Figure 4.22: Shear-induced flexural crushing in specimen B2N (courtesy by Andermatt and Lubell, University of Alberta)

Next, the predicted strain is compared with the experimental strain in the FRP reinforcement in Fig. 4.23.

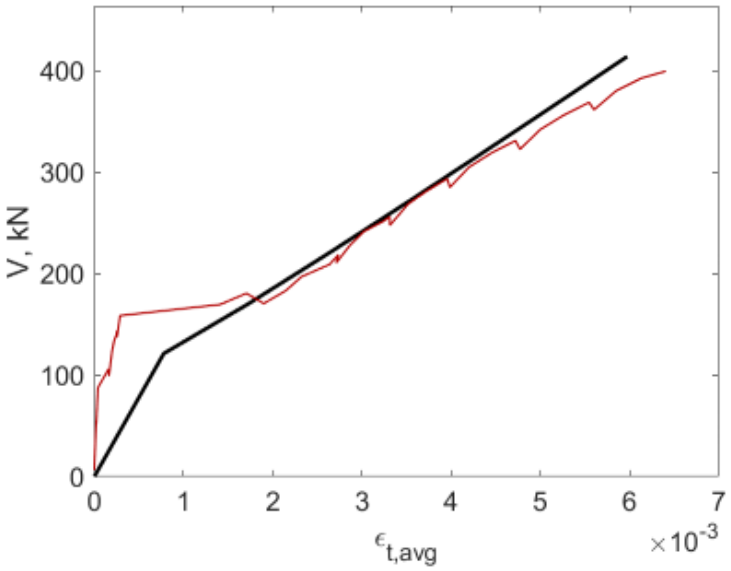

Figure 4.23: Experimental and predicted load-strain response for specimen B2N

The predicted strain response is developing similarly as the experimental one. The only minor difference is close to failure where the strains increased a little bit more in the tests than is predicted. It can be stated that the stiffness was accurately predicted.

Finally, the horizontal and vertical crack displacement at the position of the LVDT-rosette are predicted as shown in Fig. 4.24.

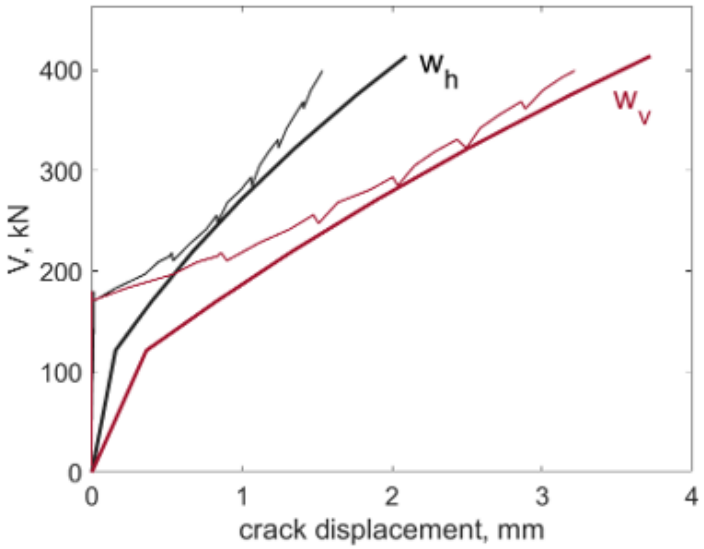

Figure 4.24: Experimental and predicted load-crack displacement response for specimen B2N

The general form of both predicted responses is very similar to the experimental ones. In terms of maximal deformations, the predicted horizontal crack displacement reaches 2 mm compared to 1.5 mm during the test and the vertical crack displacement reaches to 3.5 mm which is almost equal to the experimental one.

B3N

The experimental and predicted load-displacement response of specimen B3N are presented in Fig. 4.25.

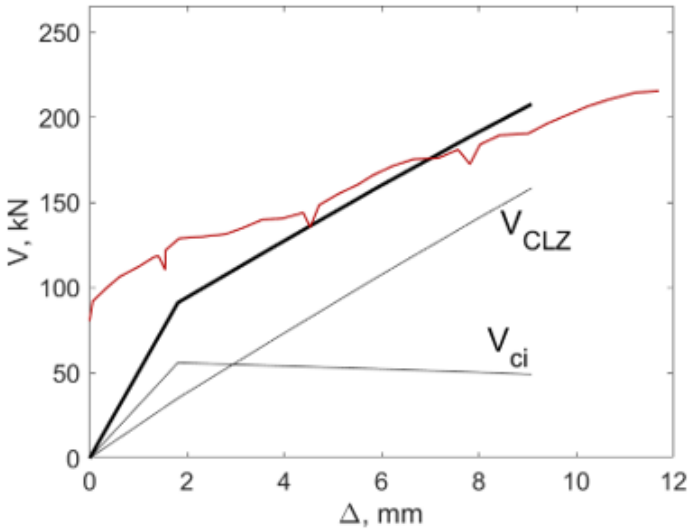

Figure 4.25: Experimental and predicted load-displacement response for specimen B3N

The predicted failure mode is shear-induced flexural crushing which corresponds well with the experimental observations as can be seen in Fig. 4.26. The predicted failure load is equal to 208 kN which is almost equal to the experimental load of 215.5 kN. The predicted deflection of 9 mm slightly underestimates the experimental deflection of 11 mm. At failure, one-fourth of the shear contribution is given by aggregate interlock and the other three-quarters due to V_{CLZ}.

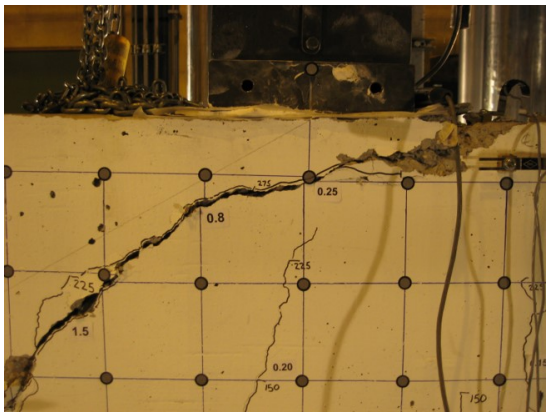

Figure 4.26: Shear-induced flexural crushing in specimen B3N (courtesy by Andermatt and Lubell, University of Alberta)

Next, the predicted strain is compared with the experimental strain in the reinforcement in Fig. 4.27.

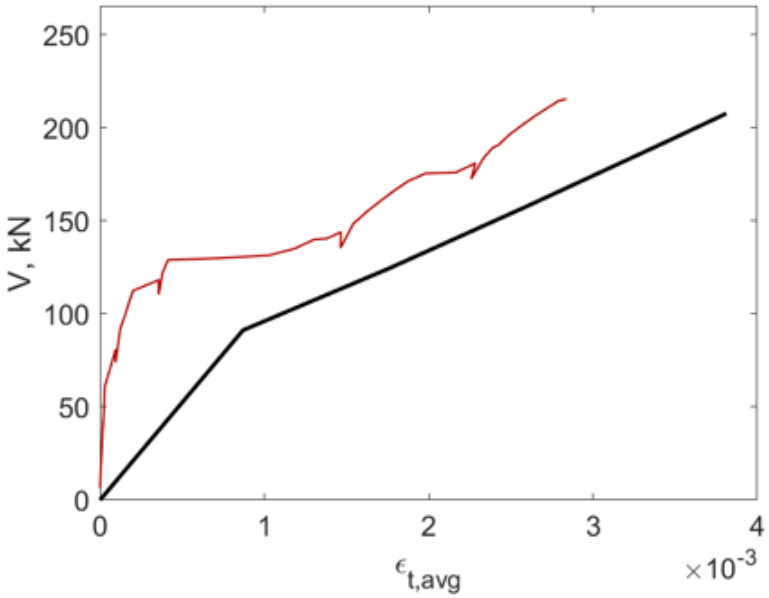

Figure 4.27: Experimental and predicted load-strain response for specimen B3N

The predicted strain of 4×10^{-3} is close to the experimental strain of 3×10^{-3}. The stiffness of the response is accurately predicted.

Finally, the horizontal and vertical displacement at the position of the LVDT-rosette are predicted as shown in Fig. 4.28.

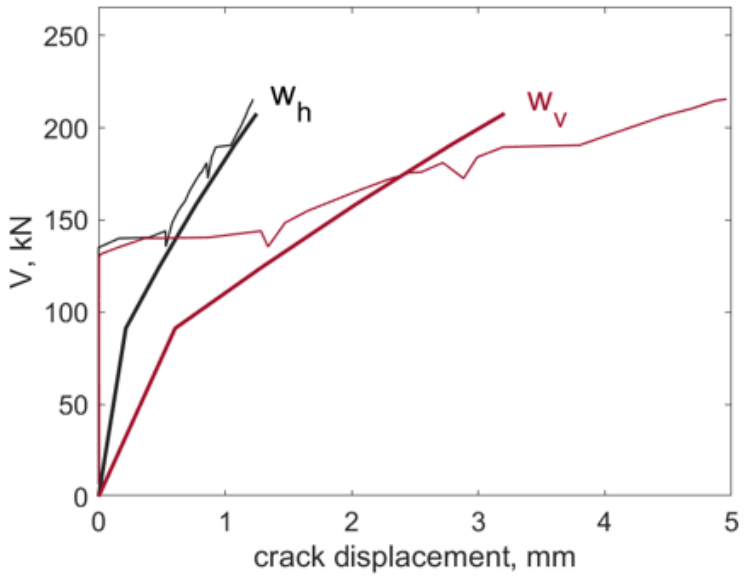

Figure 4.28: Experimental and predicted load-crack displacement response for specimen B3N

The predicted horizontal crack displacement at failure is equal to the experimental one of 1 mm and the maximal vertical crack displacement of 3 mm underestimates the experimental one of 5 mm. In terms of slope of the response, it can be concluded that the predicted horizontal response is very close to the experimental horizontal crack displacement, but the vertical response seems to be double as steep as the experimental vertical displacement.

B4N

The experimental and predicted load-displacement response of specimen B4N are presented in Fig. 4.29.

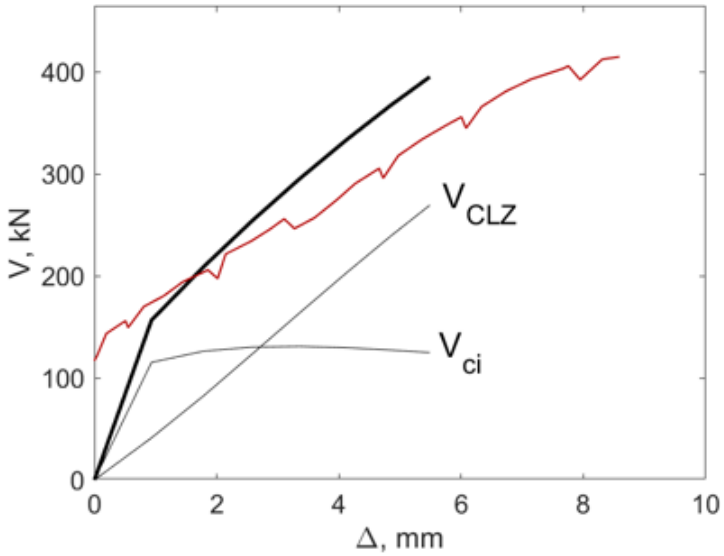

Figure 4.29: Experimental and predicted load-displacement response for specimen B4N

For specimen B4N, failure mode 1 is predicted (refer to Fig. 2.9 in Section 2.3.3): cracking of the CLZ . This does, in first instance, not correspond with the actual experimental failure mode which was shear-induced flexural crushing as presented in Fig. 4.30.

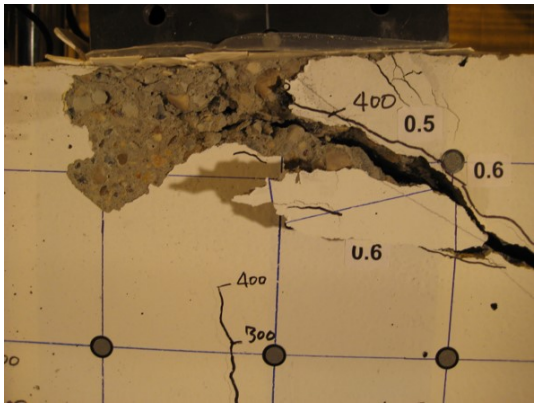

Figure 4.30: Shear-induced flexural crushing in specimen B4N (courtesy by Andermatt and Lubell, University of Alberta)

However, in Fig. 4.31 the complete response is shown. The horizontal dashed line represents the capacity due to the failure mode by cracking of the CLZ, the horizontal solid line is the capacity by shear-induced flexural crushing and the third failure mode, CLZ crushing, is represented by the maximal value of the 2PKT response in bolt.

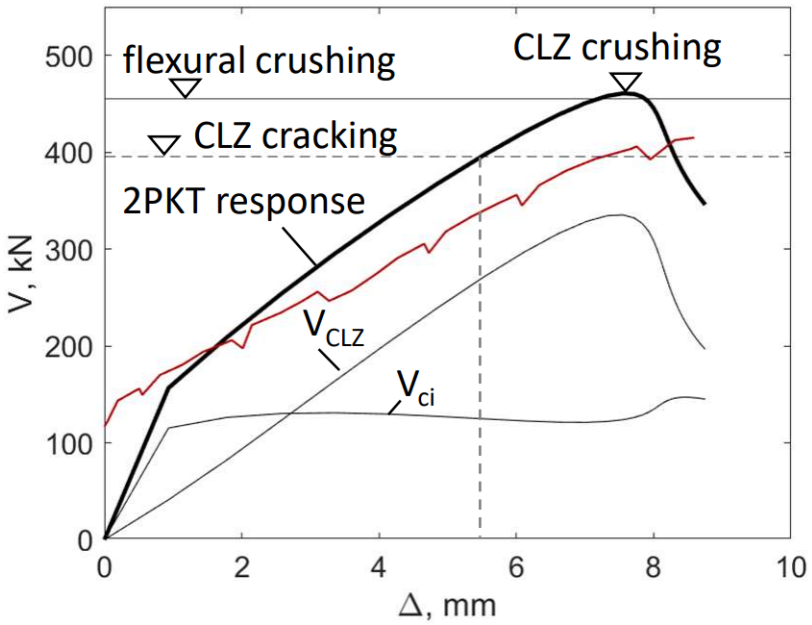

Figure 4.31: Complete load-displacement response for specimen B4N

Here can be seen that failure due CLZ cracking has a predicted capacity of 395 kN, shear-induced flexural crushing gives a capacity of 455 kN and finally, crushing of the CLZ corresponds to capacity of 460 kN. The experimental capacity is in between these values and equal to 415 kN. In other words, all three capacities are very close to each other with only a difference of 60 kN between them. The lowest one underestimates the capacity by 5% and the highest failure mode overestimates the capacity by 9%. This means that, however failure mode 1 is predicted, it seems possible that all three failure modes could have occurred. If Once-more, the experimental failure is analysed (see Fig. 4.30), it seems possible that a combination of failure modes have occurred: flexural crushing and diagonal crushing. Therefore, it can be concluded that predictions must always be treated with care and experimental failure modes can sometimes be hard to distinguish. To be consistent, the predicted failure mode, cracking of CLZ, is used to present the other results as well.

Next, the predicted strain is compared with the experimental strain in the FRP reinforcement in Fig. 4.32.

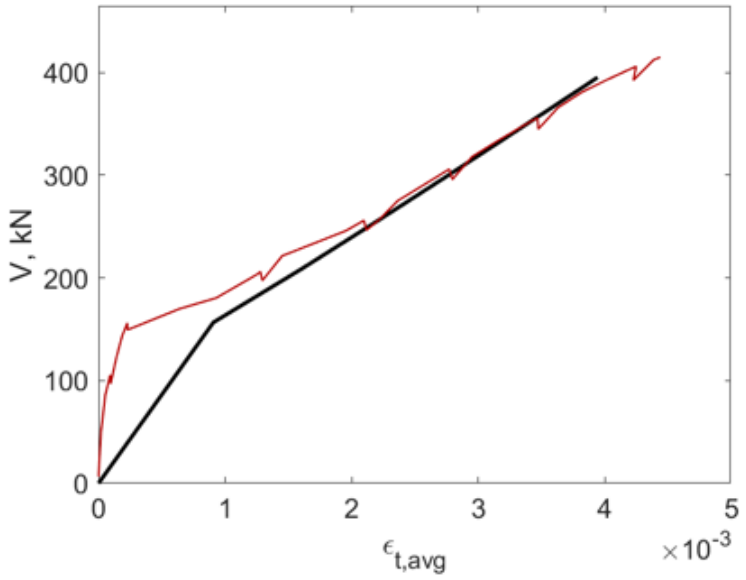

Figure 4.32: Experimental and predicted load-strain response for specimen B4N

The predicted and experimental strain are almost identical. Due to the small underestimation of the capacity, the maximal strain is also slightly underestimated by only 0.5×10^{-3}.

Finally, the horizontal and vertical crack displacement at the position of the LVDT-rosette are predicted as shown in Fig. 4.33.

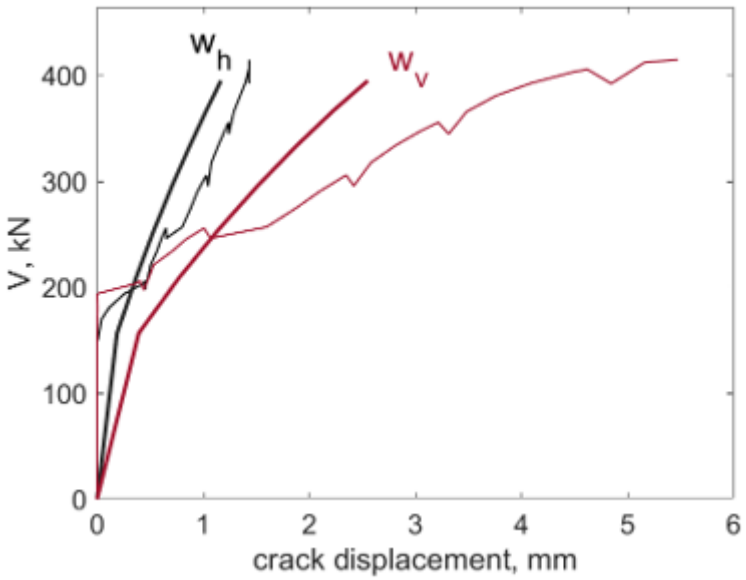

Figure 4.33: Experimental and predicted load-crack displacement response for specimen B4N

The predicted horizontal crack displacement of 1 mm is accurately predicting the experimental one. The predicted vertical crack displacement of 2.5 is underestimating the experimental one of 5.5. The slope of the predicted horizontal displacement response is almost equal to the experimental one, while the slope of the predicted horizontal displacement response is double as stiff as the experimental one.

B5H

The experimental and predicted load-displacement response of specimen B5H are presented in Fig. 4.25.

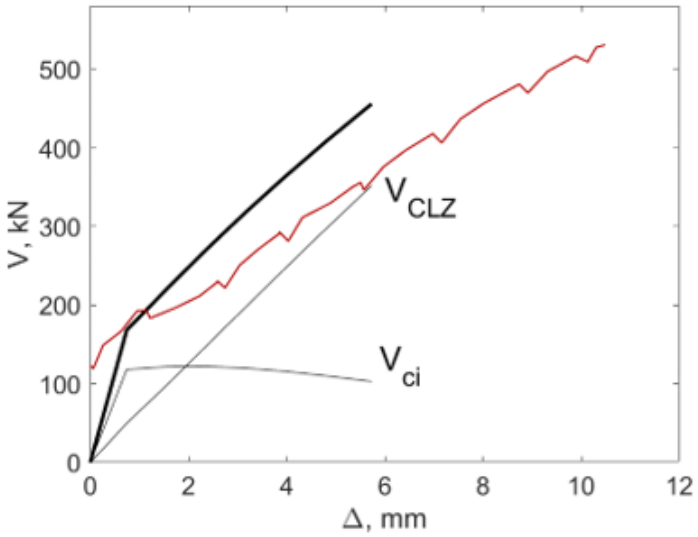

Figure 4.34: Experimental and predicted load-displacement response for specimen B5H

The predicted failure mode is shear-induced flexural crushing which corresponds well with the experimental observations as can be seen in Fig. 4.35. It can be seen that the predicted failure load of 456 kN underestimates the experimental load of 531 kN by 16% and the predicted deflection of 6 mm also underestimates the experimental deflection of 11 mm. Furthermore, the predicted response overestimates the experimental stiffness of the beam. At failure, one-fourth of the shear contribution is given by aggregate interlock and the other three-quarters by V_{CLZ}.

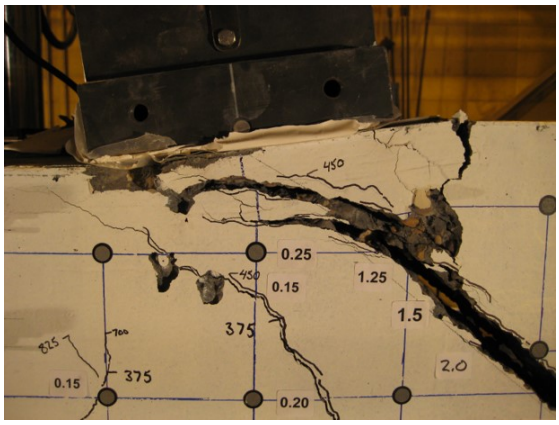

Figure 4.35: Shear-induced flexural crushing in specimen B5H (courtesy by Andermatt and Lubell, University of Alberta)

Next, the predicted strain is compared with the experimental strain in the FRP-reinforcement in Fig. 4.36.

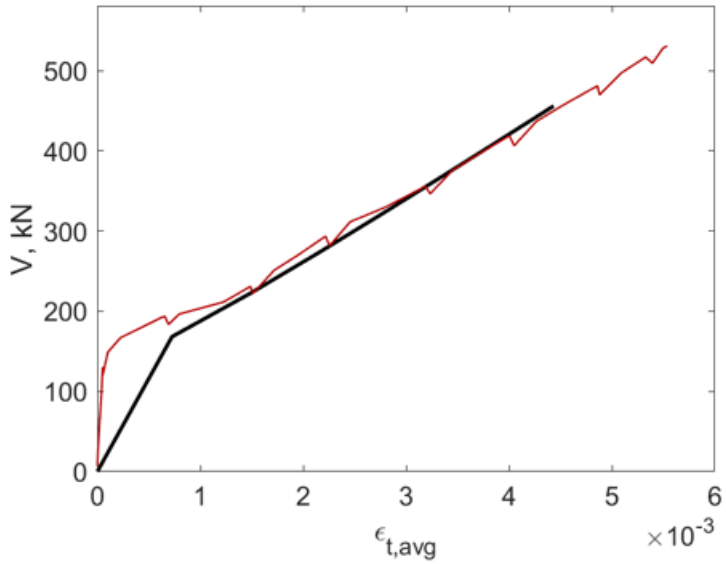

Figure 4.36: Experimental and predicted load-strain response for specimen B5H

The form of the response is very well predicted, however due to the underestimated capacity the maximal strain is also underestimated.

Finally, the horizontal and vertical crack displacement at the position of the LVDT-rosette are predicted as shown in Fig. 4.37.

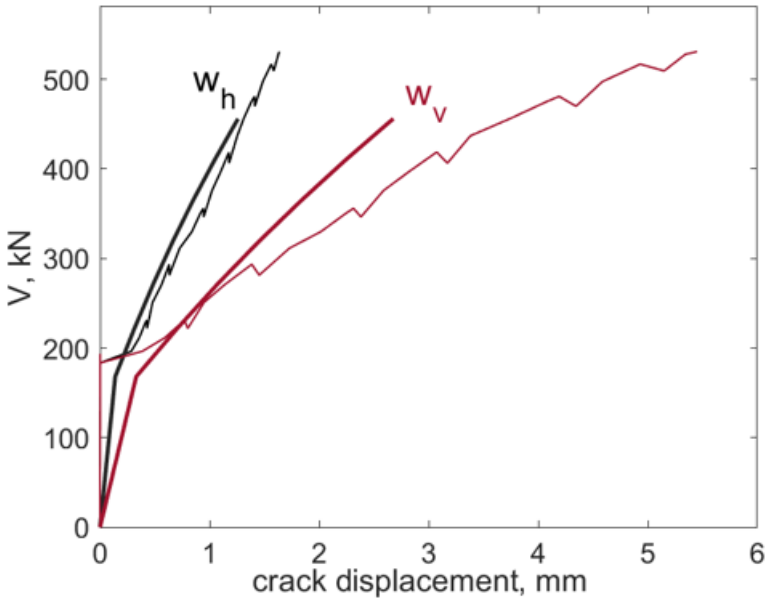

Figure 4.37: Experimental and predicted load-crack displacement response for specimen B5H

The predicted horizontal crack displacement develops similarly as the experimental response, while the slope of the predicted vertical crack displacement is twice as big as the experimental one. Furthermore, the predicted vertical displacement of almost 3 mm underestimates the experimental one of 5.5 mm, while the horizontal crack displacement is predicted almost perfectly.

B6H

The experimental and predicted load-displacement response of specimen B6H are presented in Fig. 4.38.

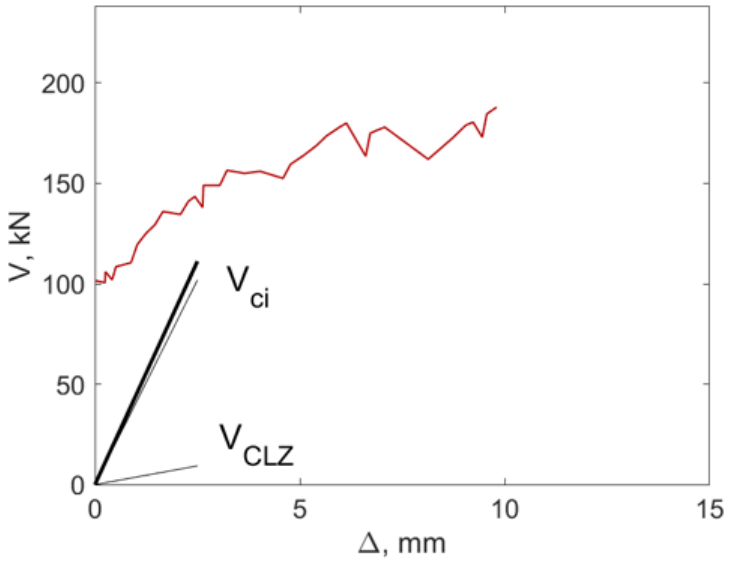

Figure 4.38: Experimental and predicted load-displacement response for specimen B6H

For specimen B6H, the predicted failure mode is failure mode 3 (refer to Fig. 2.9 in Section 2.3.3): shear-induced flexural crushing. However, the experimental failure mode was cracking of the CLZ as can be seen in Fig. 4.39. While the experimental failure load was 188 kN, the predicted capacity is 111 kN, an underprediction of 69%. In correspondence, the deflections are heavily underestimated.

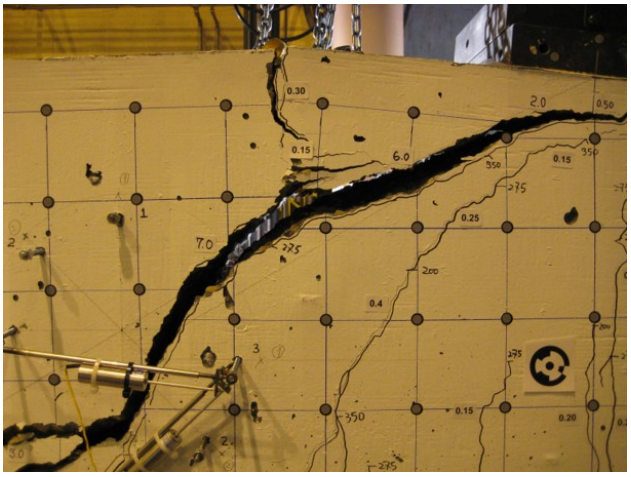

Figure 4.39: Shear-induced flexural crushing in specimen B6H (courtesy by Andermatt and Lubell, University of Alberta)

Next, the predicted strain and the displacements are presented in Fig. 4.40.

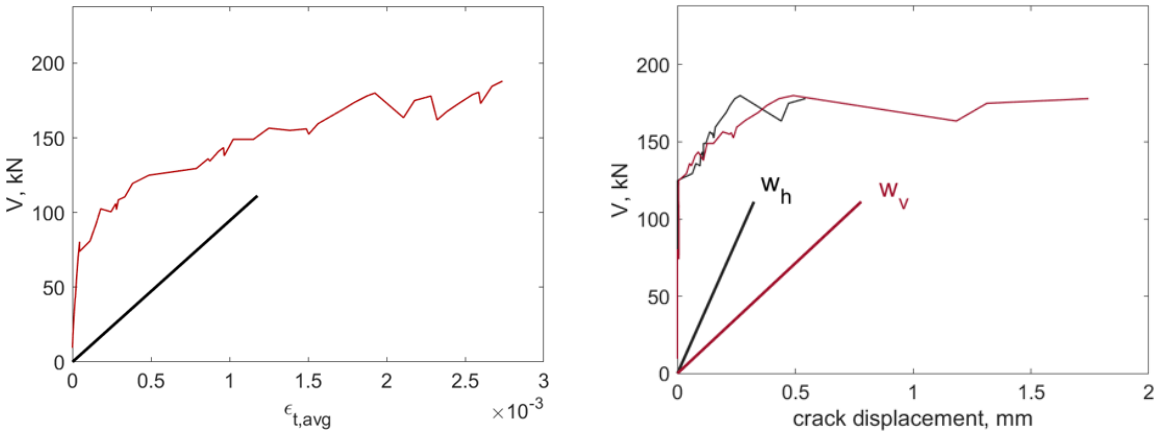

(a) Experimental and predicted load-strain response for specimen B6H

(b) Experimental and predicted load-crack displacement response for specimen B6H

Figure 4.40: Results for specimen B6H

There can be concluded that the predictions are not that good.

However, a discussion can be made if the failure mode by shear-induced flexural crushing can possibly occur. The load-displacement response is presented again in Fig. 4.41, but this time the cracking of the CLZ is assumed to govern the shear capacity.

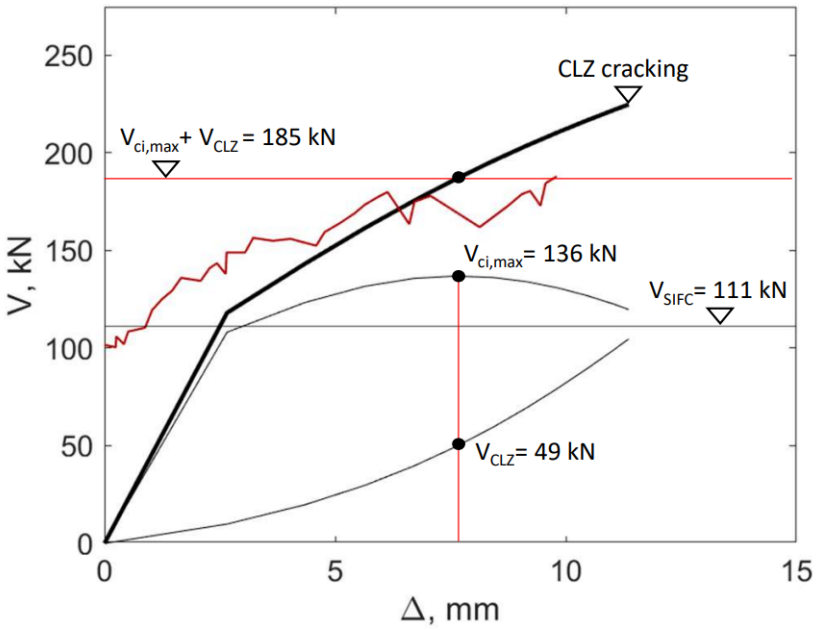

Figure 4.41: Experimental and adapted load-displacement response for specimen B6H

The predicted failure mode by shear-induced flexural crushing is represented by the horizontal grey line. At the moment that the SIFC should occur according to the prediction, there is still a lot of aggregate interlock and also a small contribution of the V_{CLZ}. If the sum of the maximum of aggregate interlock $V_{ci,max}$ and the corresponding V_{CLZ} is taken, then the shear capacity equals 185 kN. Until this point shear can still be carried, and, moreover, shear is carried for more than 70% by aggregate interlock. Therefore, it seems not possible that the specimen will

fail at a value of 111 kN. Now an interesting remark to make is that in all the previous specimens, there was almost no aggregate interlock contribution or it was negligible in comparison to V_{CLZ}. This time however, aggregate interlock represents the main contribution to shear and, exactly for this reason, it is the big aggregate interlock which prohibits the shear-induced flexural crushing to happen. The following assumption can be made: $V_{SIFC} \geq V_{ci,max} + V_{CLZ}$ if it is smaller, it will not happen.

If this assumption is implemented in the model, then the predicted failure mode is cracking of the CLZ. The predicted capacity is 225 kN in comparison to the experimental failure load of 188 kN. The prediction still overestimated the capacity by 16%, but the accuracy of the prediction has largely improved.

The results, obtained after the implementation of the condition $V_{SIFC} \geq V_{ci,max} + V_{CLZ}$, are accounted for in the further discussion and are referred to as 'adapted predictions'.

First, the adapted predicted strain in the FRP reinforcement is presented in Fig. 4.42.

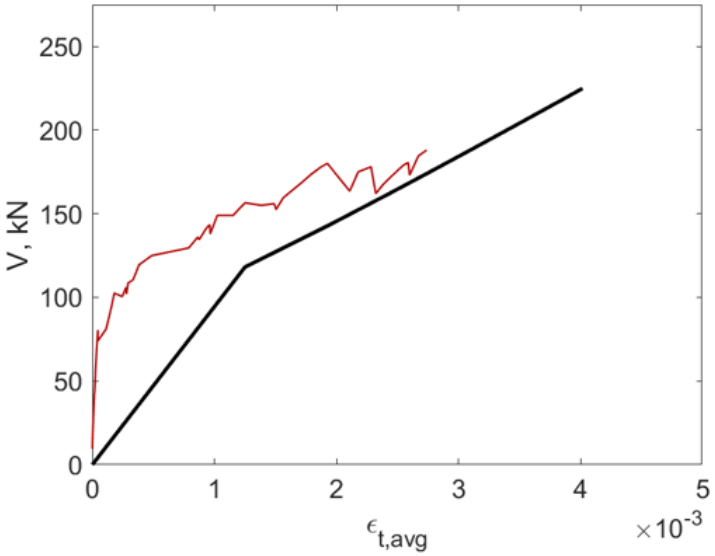

Figure 4.42: Experimental and adapted predicted load-strain response for specimen B6H

The strains are overestimated, but the stiffness of the prediction is comparable to the stiffness of the experiment.

Finally, the adapted predicted crack displacements are shown in Fig. 4.43.

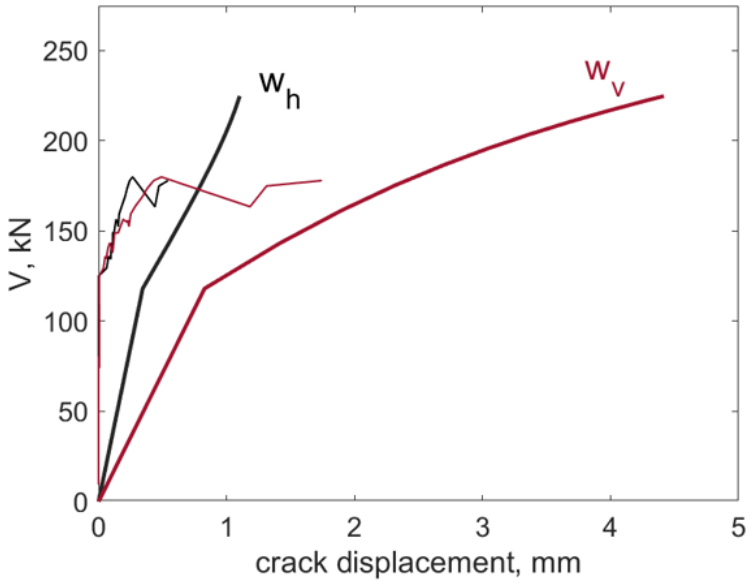

Figure 4.43: Experimental and adapted predicted load-crack displacement response for specimen B6H

The predicted horizontal displacement goes up to 1 mm and the vertical displacement is equal to 4.5 mm. Both displacement responses overestimate the experimental ones.

It may be assumed that the condition $V_{SIFC} \geq V_{ci,max} + V_{CLZ}$ is justified and therefore permanently implemented in the model. Now, a second discussion to make is about the fact that the model, which now predicts cracking of the critical loading zone to occur, assumed that there was no aggregate interlock such that the resultant force is constrained to pass through the center of the bearing plate. This resulted in the use of α_{crit} to determine the angle of the resultant force. However, Fig. 4.44 presents the stress distribution along the crack due to aggregate interlock.

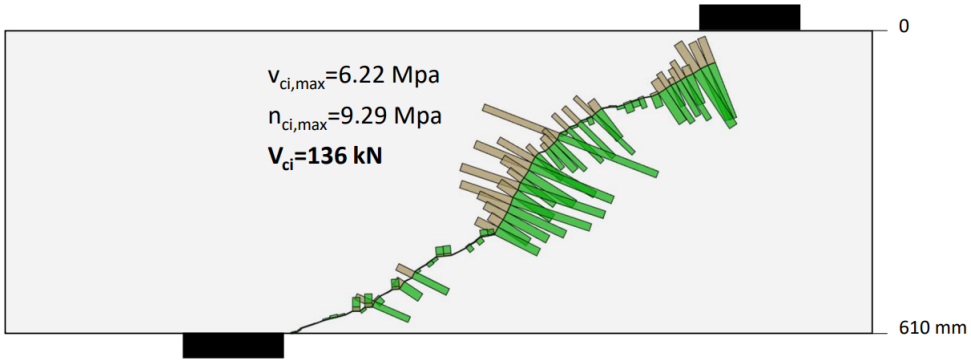

Figure 4.44: Aggregate interlock stresses along the critical crack in specimen B6H

This figure shows the detailed distribution of interlock stresses of every crack segment along the crack. The total shear contribution equals 136 kN which corresponds to the value shown in Fig. 4.41. This implies that the aggregate interlock is not negligible. If this is taken into account, then, the earlier-discussed assumption is not valid anymore. Resulting from this, the shear force by CLZ, V_{CLZ}, can directly be projected on the inclined plane with the angle α_{CLZ} (refer to Fig. 3.11 in Section 3.7). The new results are shown in Fig. 4.45.

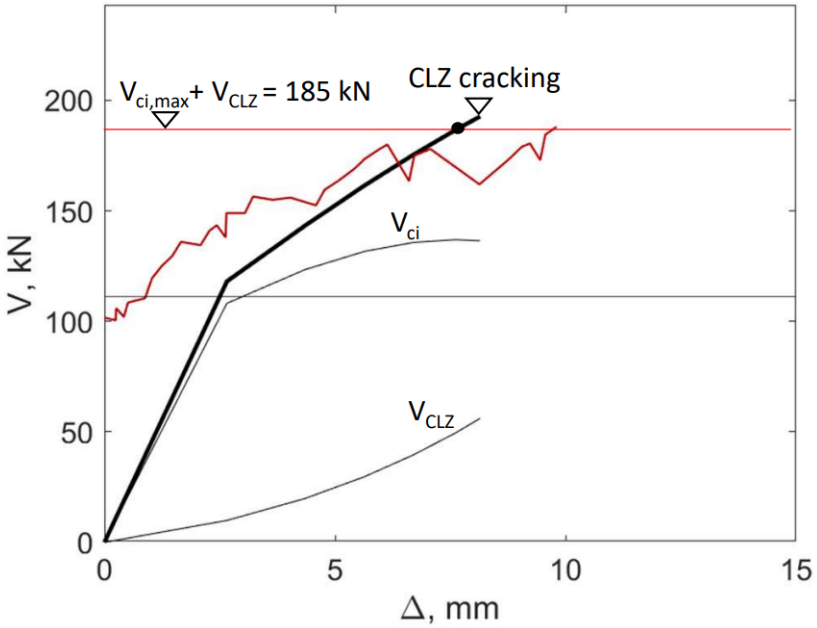

Figure 4.45: Experimental and final predicted load-displacement response for specimen B6H

Now the predicted shear capacity is equal to 193 kN compared to an experimental value of 188 kN. This is almost a perfect prediction. Furthermore, the condition $V_{SIFC} \geq V_{ci,max} + V_{CLZ}$ can also be applied on the capacity by CLZ cracking, but it is not governing the results as shown in Fig. 4.45.

The condition $V_{SIFC} \geq V_{ci,max} + V_{CLZ}$ and the discussion on the angle of the resultant force are both justified by the results. Therefore, the model was modified to take them into account. The final predicted capacity of specimen B6H is thus equal to 193 kN. For convenience, the final load-strain and the final load-crack displacement responses are recalculated with the model and shown in Fig. 4.46. The responses are, for obvious reasons, similar to Fig. 4.42 and Fig. 4.43.

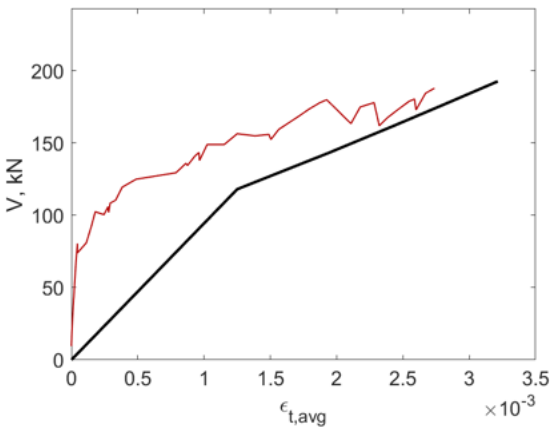

(a) Experimental and final predicted load-strain response for specimen B6H

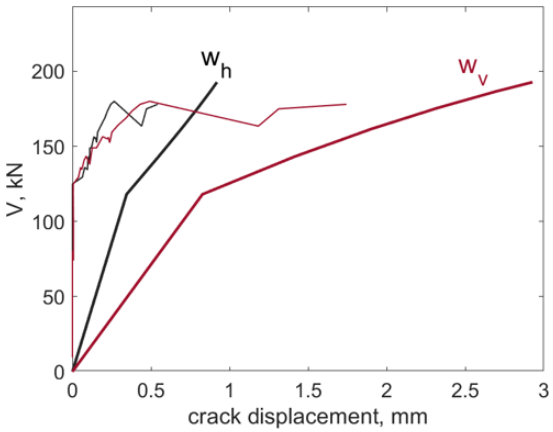

(b) Experimental and final predicted load-crack displacement response for specimen B6H

Figure 4.46: Final results for specimen B6H

In correspondence with the improved prediction of the shear capacity, the predictions of the strain at failure and the crack displacements have improved.

A final discussion can be held on the effect of the concrete tension strength limit f_{ct} (refer to Section 3.7) on the results. It is clear that a higher tension limit will lead to a higher possible shear capacity and vice versa. Therefore, it seems important to accurately predict this value. There exist several equations to predict the tension limit f_{ct}. One very conservative approach is to take $f_{ct} = 0.5f_r$. This rupture strength f_r is derived by a three point bending test on a unreinforced beam and, from this, the tension limit can be directly derived. The rupture strength is known from tests [8] and is equal to 6.3 MPa, this results in $f_{ct} = 0.5f_r = 3.15$ MPa. The modified load-displacement response is shown in Fig. 4.47.

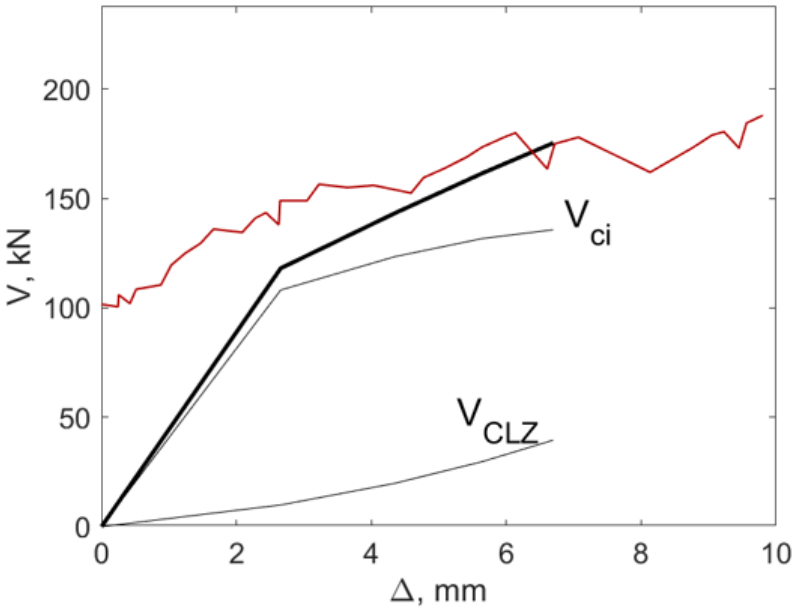

Figure 4.47: Experimental and modified predicted load-displacement response for specimen B6H

The predicted capacity is equal to 175 kN. As expected, this is lower than the previous prediction, and, therefore, using $f_{ct} = 0.5f_r$ will result in conservative predictions. The difference in shear capacity by using the equation from the model and this new equation is 18 kN. The ratio for the original equation was $V_{exp}/V_{pred} = 0.97$ and for the new equation $V_{exp}/V_{pred} = 1.07$. The experimental capacity value will be somewhere between the two shear capacities induced by the two concrete tension strength limits.

The question raises to which extend the prediction of the concrete tension strength needs to be optimized to increase the accuracy of the predictions. It is clear that this one parameter not only governs the results, but clearly affects them. From the other hand, as mentioned before, there are numerous approaches to predict this tension strength, but in the end, this value remains strongly 'specimen-dependant'. Therefore, the need to optimize the prediction of the concrete tension strength and, thus, the correspondent equations seems not necessary in terms of not complicating a rather simplified modelling approach as the cracking of the CLZ.

C1N

The experimental and predicted load-displacement response of specimen C1N are presented in Fig. 4.48.

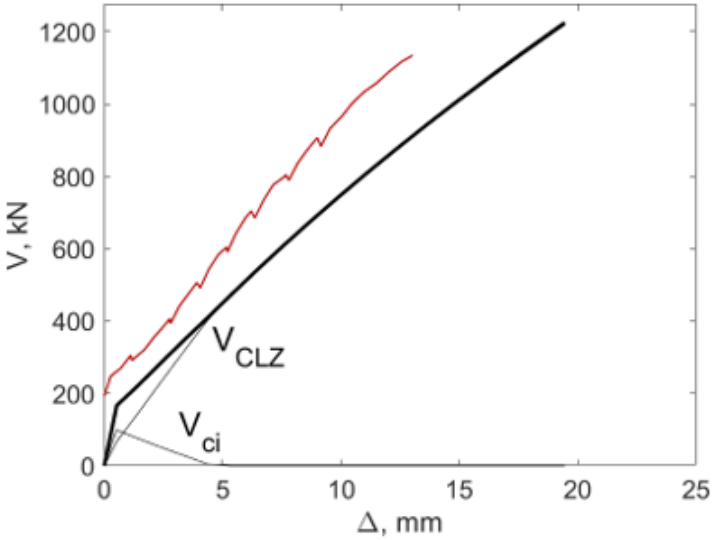

Figure 4.48: Experimental and predicted load-displacement response for specimen C1N

The predicted failure mode is shear-induced flexural crushing which corresponds well with the experimental observations as can be seen in Fig. 4.49. The predicted failure load is equal to 1225 kN, compared to an experimental load of 1134.5 kN. The ratio between them is $V_{exp}/V_{pred} = 0.93$. The predicted deflection of almost 20 mm overestimates the experimental deflection of 13 mm. At failure, the shear capacity is fully carried by V_{CLZ} which is due to the large crack widths which prohibit aggregate interlock to carry shear (see Fig. 4.51).

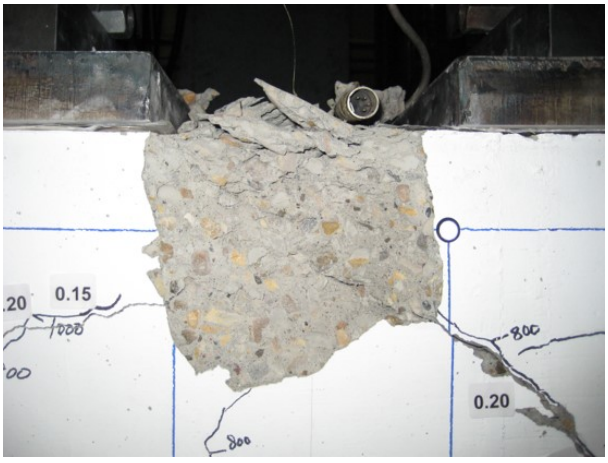

Figure 4.49: Shear-induced flexural crushing in specimen C1N (courtesy by Andermatt and Lubell, University of Alberta)

Next, the predicted strain is compared with the experimental strain in the FRP reinforcement in Fig. 4.50.

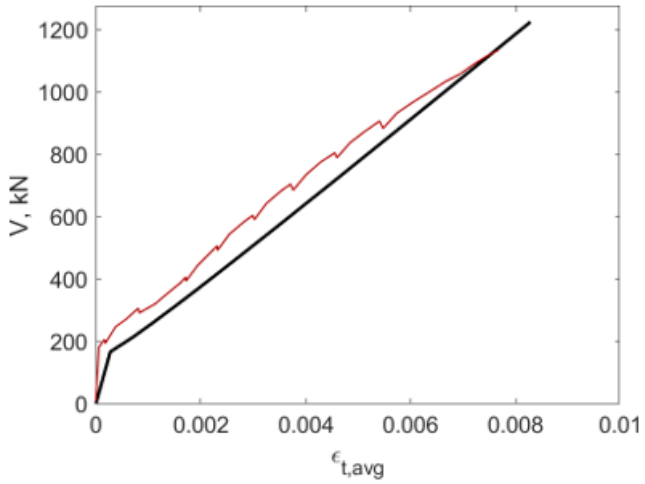

Figure 4.50: Experimental and predicted load-strain response for specimen C1N

The predicted strain follows almost perfectly the experimental response. Due to the small overprediction of strength, the strain is also slightly overpredicted.

Finally, the horizontal and vertical crack displacement at the position of the LVDT-rosette are predicted as shown in Fig. 4.51.

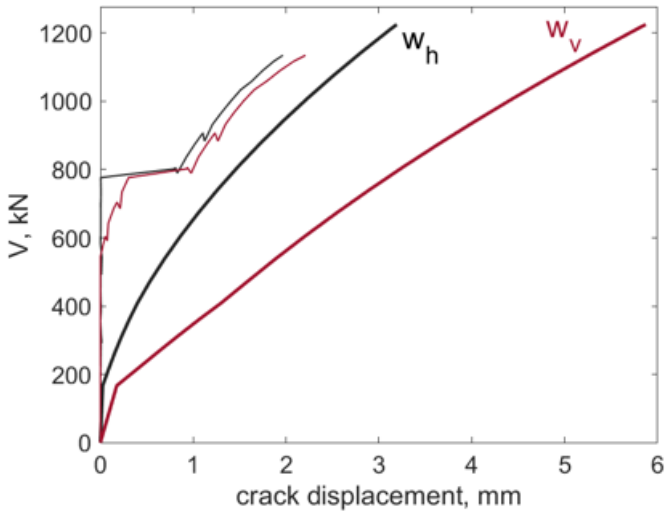

Figure 4.51: Experimental and predicted load-crack displacement response for specimen C1N

The predicted maximal horizontal displacement is equal to 6 mm and the predicted vertical displacement is equal to 3 mm. These values are not very accurately predicted in comparison to the experimental ones. The measurements showed that the horizontal and vertical crack displacement almost developed exactly the same. This may be possible because the a/d ratio is almost equal to 1 for this specimen, but, from the other hand, it can be possible that measurement equipment was not correctly employed.

C2N

The load-displacement response of specimen C2N is presented in Fig. 4.52.

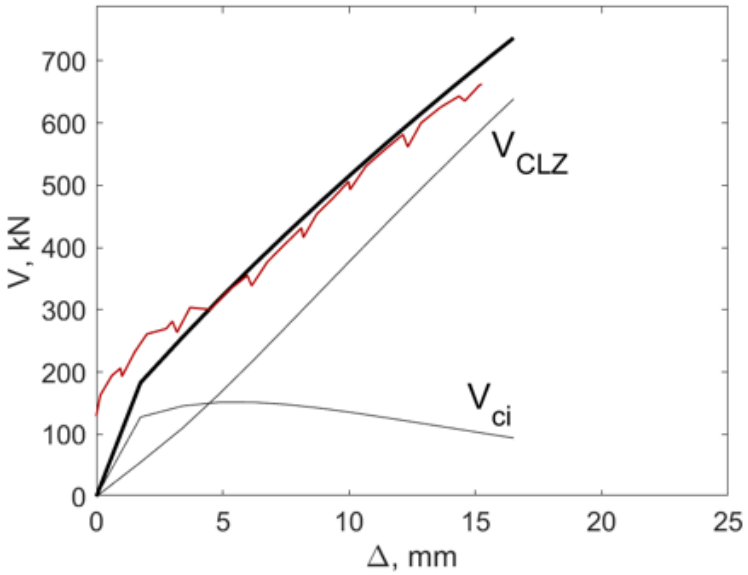

Figure 4.52: Experimental and predicted load-displacement response for specimen C2N

The predicted failure mode is shear-induced flexural crushing which corresponds well with the experimental observations as can be seen in Fig. 4.53. The predicted failure load of 736 kN overestimates the experimental load of 662 kN by 10%. The predicted deflection of 17 mm is almost equal to the experimental deflection of 15 mm. At failure, the shear capacity is carried for 70% by V_{CLZ} and the rest by aggregate interlock. The fact that there is a contribution of aggregate interlock, can be explained by the small crack widths developing in the specimen (see Fig. 4.55). Further, it can be stated that, once-again, the experimental response is accurately predicted in terms of stiffness.

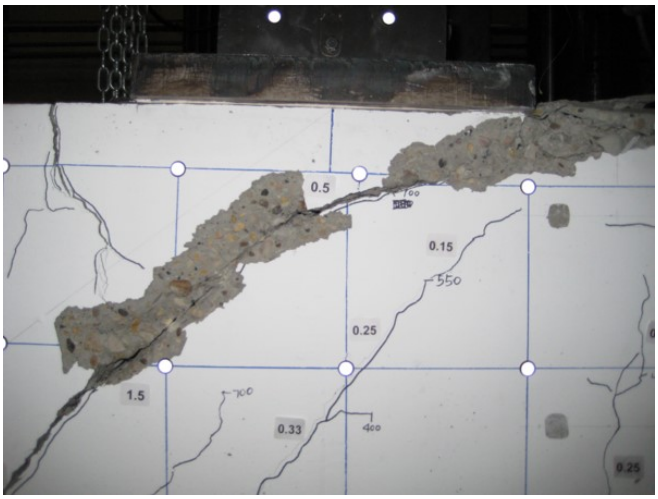

Figure 4.53: Shear-induced flexural crushing in specimen C2N (courtesy by Andermatt and Lubell, University of Alberta)

Next, the predicted strain is compared with the experimental strain in the FRP reinforcement

in Fig. 4.54.

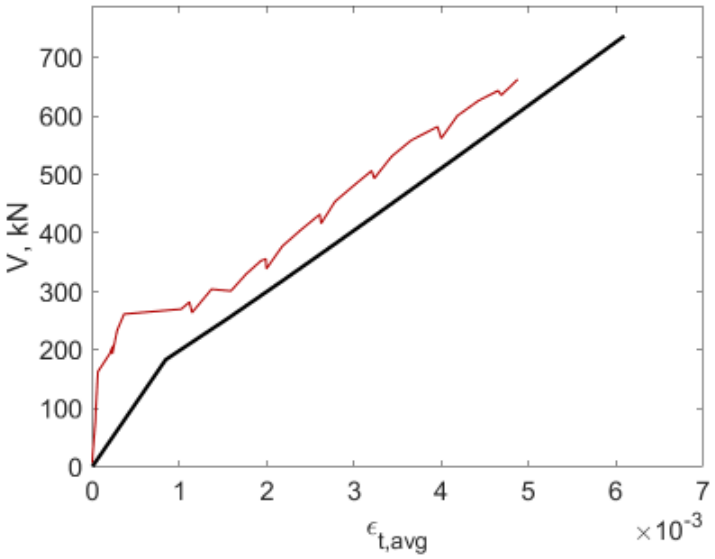

Figure 4.54: Experimental and predicted load-strain response for specimen C2N

The predicted strain has the same stiffness as the experimental response. Due to the small overprediction of strength, the strain is also slightly overpredicted.

Finally, the horizontal and vertical crack displacement at the position of the LVDTs are predicted as shown in Fig. 4.55.

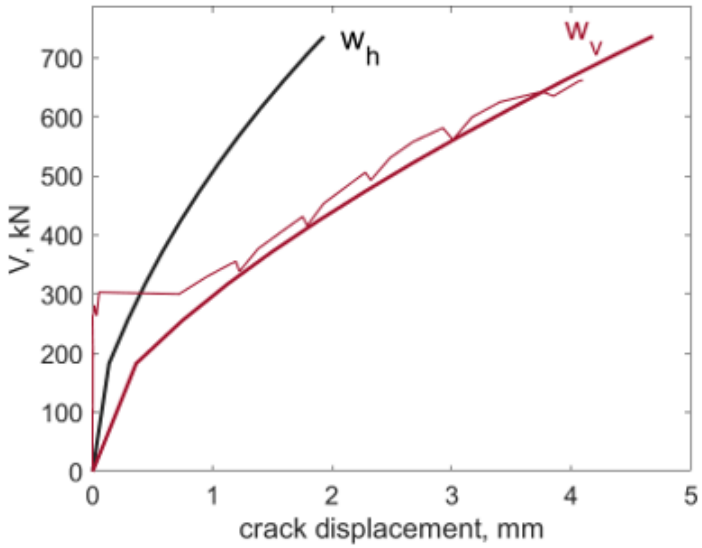

Figure 4.55: Experimental and predicted load-crack displacement response for specimen C2N

The horizontal crack displacement was not measured during the test, but the predicted maximal horizontal crack displacement is equal to 2 mm. The predicted vertical crack displacement is equal to 4.5 mm which is very close to the experimental one of 4 mm.

4.1.2 Effects of test variables

Variables can have an effect on the strength and the stiffness of specimens. This effect is analysed by comparing similar specimens with only one different variable. Therefore, based on the variables defined in Table 1, the effects of the following variables are analysed: shear span-to-depth ratio a/d, reinforcement ratio ρ_l and the concrete strength f_c'.

Shear span-to-depth ratio in specimens A1N, A2N and A3N

The shear span-to-depth ratio of specimens A1N, A2N and A3N are respectively equal to 1.07, 1.44 and 2.02. First, the experimental and predicted load-displacement responses of all three specimens are compared in Fig. 4.56.

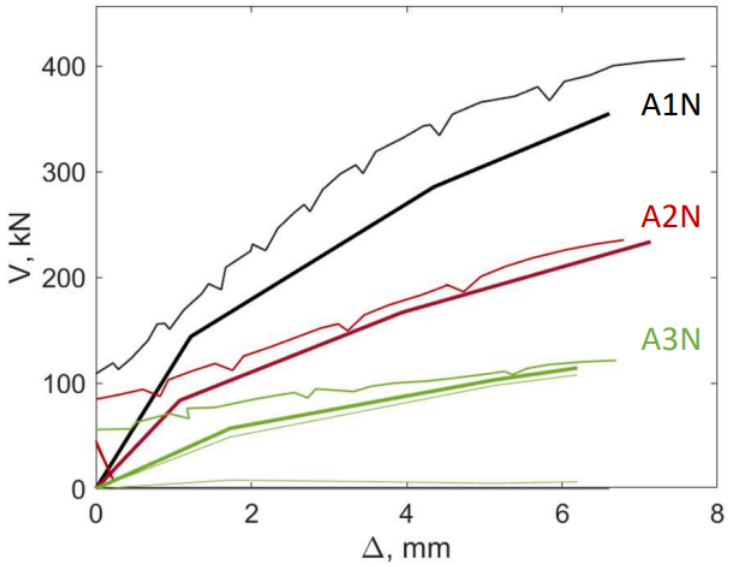

Figure 4.56: Experimental and predicted load-displacement response for specimens A1N, A2N and A3N

There can be seen that both in experiments as in the predictions a gradual decrease of the shear capacity is observed for increasing a/d ratio's which is in correspondence with the trend shown in 2.1. Going from specimen A3N to specimen A2N, a/d decreases from almost 2 to 1.44, which resulted in a doubling of the capacity. Then, when the a/d is further decreased from 1.44 for specimen A2N to almost 1 for specimen A1N, the capacity doubled again. All specimens are carrying shear completely by V_{CLZ}, and, therefore, the increasing capacity is due to the increasing shear contribution of CLZ. The difference between the experimental and predicted capacity seems to increase by a decreasing a/d. This may be due to an underestimation of the CLZ, which is possibly caused by the small dimensions of these specimens. The underestimation of the CLZ is proportional to the importance of the shear by CLZ, which is more and more important for a decreasing a/d. Therefore the underestimation of the failure load is larger in specimen A1N than A2N and A3N Furthermore, the stiffness is also increasing by decreasing the a/d ratio. The final deflection of all three specimens are inbetween 6 to 7 mm.

It can be seen that specimen A3N is the only specimen with a shear contribution by aggregate interlock, but it is only responsible for a small contribution of around 5% of the shear capacity. However, the fact that there is a contribution may be explained by the smaller crack displacements in this specimen (see Fig. 4.12) than the crack displacements of the other two

specimens (see Fig. 4.8 and 4.4) .

Next, the strains in the FRP reinforcements are shown in Fig. 4.57.

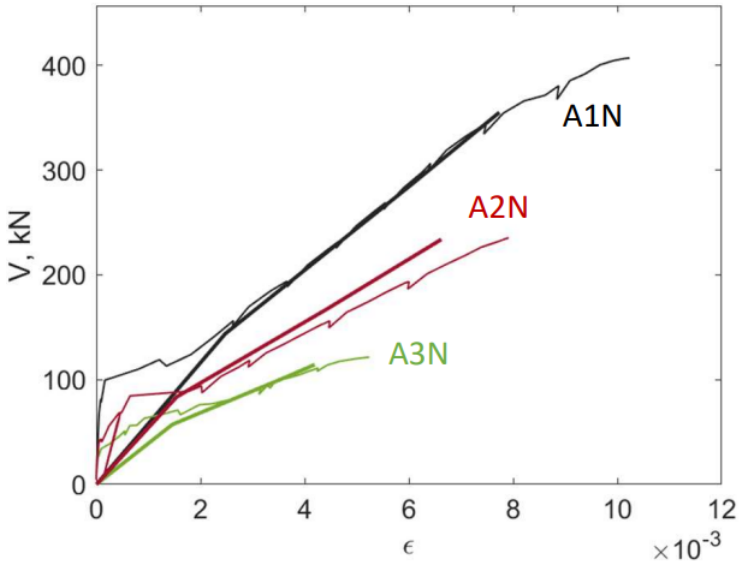

Figure 4.57: Experimental and predicted load-strain responses for specimens A1N, A2N and A3N

The effect of the shear span-to-depth ratio on the strain is related to the capacity of the specimens. By decreasing the a/d ratio, the failure loads are increasing and, thus, the strains are increasing.

Finally, the effect on the crack displacements is analysed in Fig. 4.58.

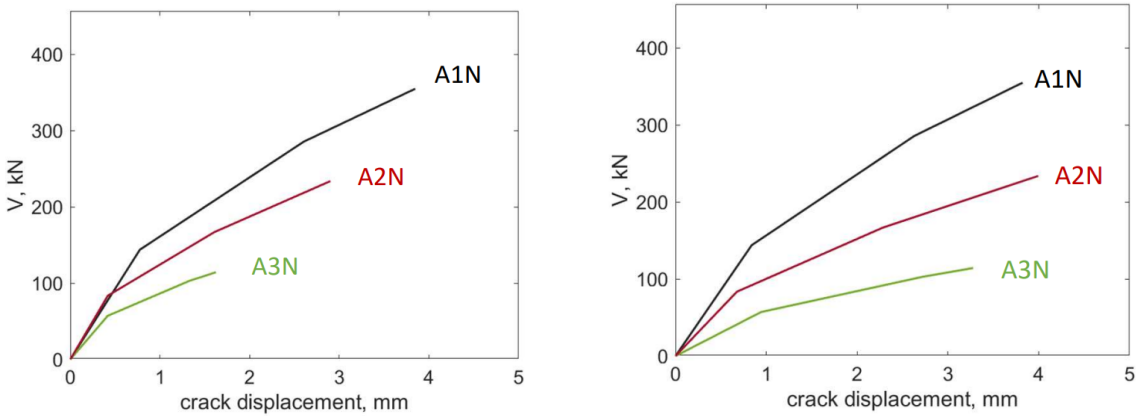

(a) Predicted horizontal crack displacement for specimens A1N, A2N and A3N

(b) Predicted vertical crack displacement for specimens A1N, A2N and A3N

Figure 4.58: load-crack displacement response for specimens A1N, A2N and A3N

Here can be seen that the predicted horizontal crack displacements are increasing when a/d in decreasing. From the other hand, the predicted vertical displacement stays almost equal.

Shear span-to-depth ratio in specimens B1N, B2N and B3N

The shear span-to-depth ratios of specimens B1N, B2N and B3N are respectively equal to 1.08, 1.48 and 2.07 which are comparable to the previous comparison. First, the predicted and experimental load-displacement responses are presented in Fig. 4.59.

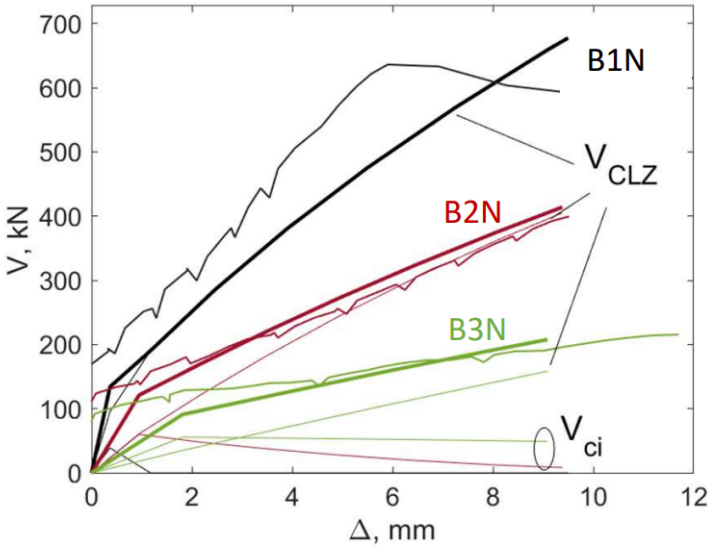

Figure 4.59: Experimental and predicted load-displacement response for specimens B1N, B2N and B3N

Once-more, an increase of the shear capacity is observed by decreasing the shear span-to-depth ratio. By decreasing a/d from 2.07 to almost 1.5, the capacity has almost doubled and when the a/d is further decreased from almost 1.5 to 1.08 the capacity increases by a bit more than 50%. Corresponding to the increase of the strength, the importance of V_{CLZ} increases. Furthermore, in the experiments and in the predictions, it can be seen that an increased a/d ratio leads to an increase stiffness. Together with an increased stiffness, the maximal experimental deflections decrease from 12 mm in B3N to 9 mm in B2N to 6 mm in B1N (the post-peak deformation of B1N shown on the graph, is not taken into account). However, the predictions show an almost similar deflection.

Next, the strains in the FRP reinforcements are shown in Fig. 4.60.

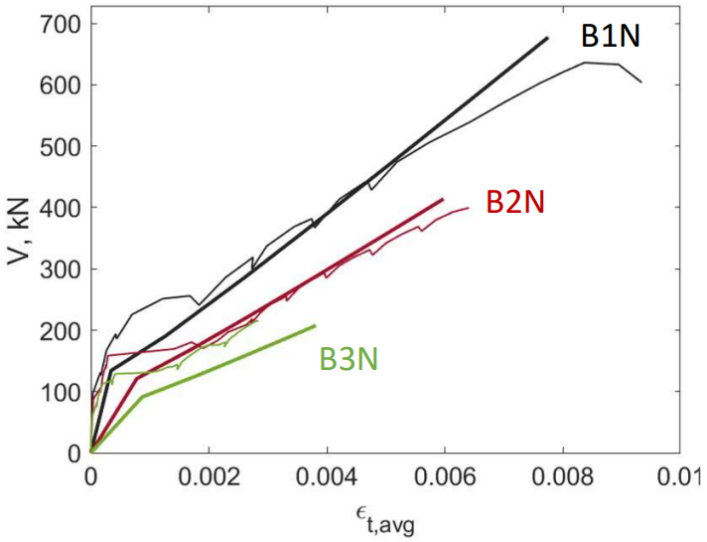

Figure 4.60: Experimental and predicted load-strain responses for specimens B1N, B2N and B3N

Once-more, the strains are increasing by decreasing the a/d ratio. While in specimen B3N the strains were twice as big as the elastic strain limit in conventional steel, the strains grow to 8×10^{-3} which is four times bigger than the elastic limit of steel.

Finally, the effect on the crack displacements is analysed in Fig. 4.61.

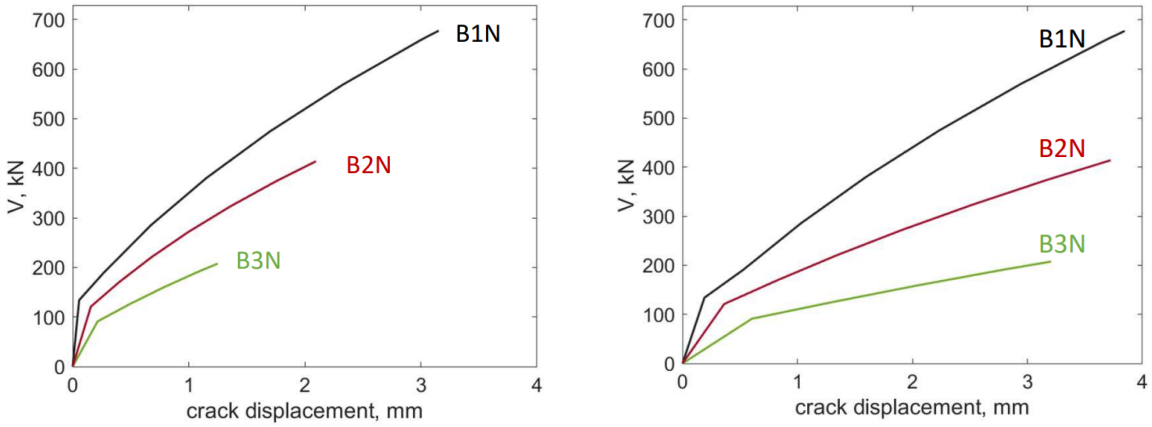

(a) Predicted horizontal crack displacement for specimens B1N, B2N and B3N

(b) Predicted vertical crack displacement for specimens B1N, B2N and B3N

Figure 4.61: load-crack displacement response for specimens B1N, B2N and B3N

Again, the horizontal crack displacement increases for a decreasing a/d and the maximal vertical displacements are almost equal.

Shear span-to-depth ratio in specimens C1N and C2N

The shear span-to-depth ratios of specimen C1N is 1.1 and of specimen C2N is 1.49. The experimental and predicted load-displacement responses of both specimens are presented in Fig. 4.62.

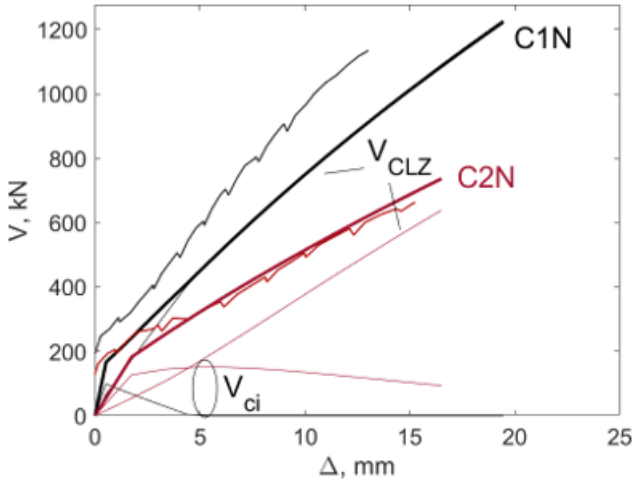

Figure 4.62: Load-displacement response for specimens C1N and C2N

For a third time, decreasing the shear span-to-depth ratio leads to a higher shear capacity and, Once-more, the importance of V_{CLZ} increases. However, while specimen C2N had still a contribution of aggregate interlock, specimen C1N is completely depending on the shear contribution of the CLZ. This may be caused by the smaller crack displacements which allowed the aggregate interlock to occur. There can be observed that the stiffness increases for lower a/d ratios, but the stiffness is still a bit underpredicted which lead to an overpredicted maximum deflection.

Next, the strains in the FRP reinforcement are shown in Fig. 4.63.

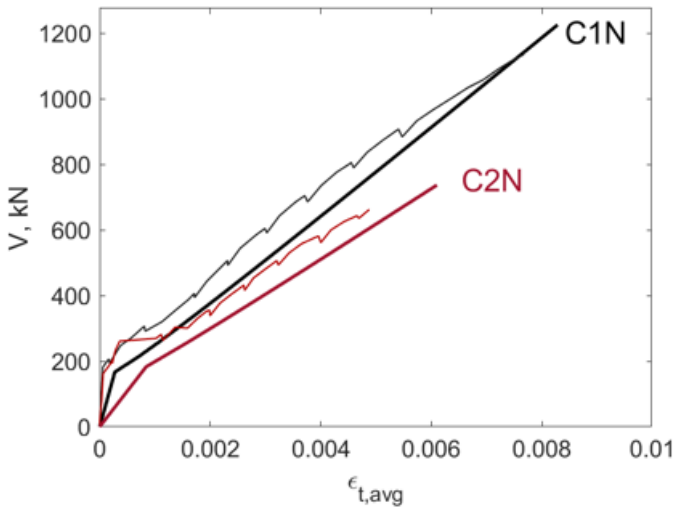

Figure 4.63: Experimental and predicted load-strain responses for specimens C1N and C2N

Once-more, the maximal strain increased for a decreased a/d ratio.

Finally, the effect on the crack displacements is analysed with Fig. 4.64.

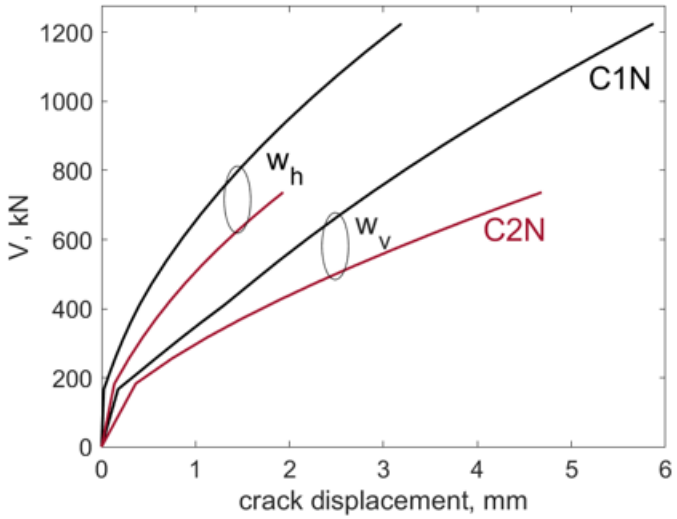

Figure 4.64: Experimental and predicted load-crack displacement for specimens C1N and C2N

For these two specimens, both the horizontal and vertical displacement increased when the a/d ratio decreased. This behavior differs from the previous two comparisons.

Reinforcement ratio in specimens B2N and B4N

The reinforcement ratio of specimen B2N is 1.71% and of specimen B4N is 2.13%. The experimental and predicted load-displacement responses of both specimens are presented in Fig. 4.65.

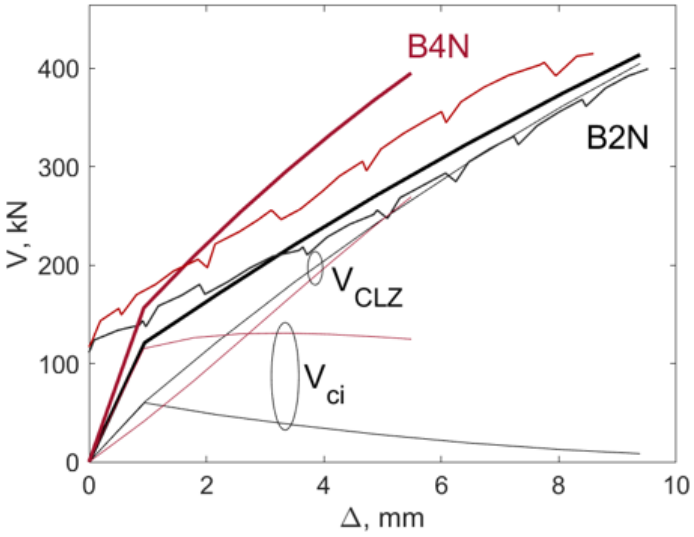

Figure 4.65: Experimental and predicted load-displacement response for specimens B2N and B4N

In the predicted results the increase of the reinforcement ratio lead to an increase of the stiffness. However, in the experimental results the stiffness stayed almost constant. The same difference between experimental and predicted behavior is seen by the maximal deflection. The increased reinforcement ratio lead to a smaller prediction of the deflection, while the experimental

maximal deflections were almost equal. Furthermore, the reinforcement ratio did not had an effect on the shear capacity of the specimen. However, the shear capacity developed in a different manner. For specimen B4N, one-third of the shear capacity was due to aggregate interlock, while for specimen B2N with the lower reinforcement ratio the aggregate interlock contribution was negligible at failure. This can be explained by the fact that the higher reinforcement ratio, keeps the crack displacements lower, which enables aggregate interlock to occur.

Next, the strains in the FRP reinforcement are shown in Fig. 4.66.

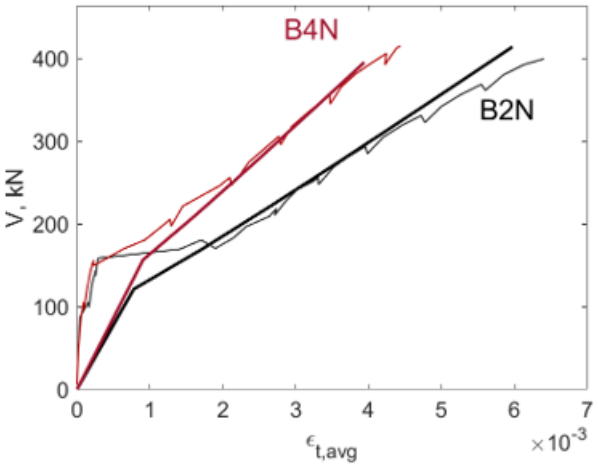

Figure 4.66: Experimental and predicted load-strain responses for specimens B2N and B4N

There can be seen that both predictions were very accurate. The increase of the reinforcement ratio lead, logically (higher area of reinforcement for same force results in lower stresses, and thus in lower strains), to a lower average strain in the reinforcement.

Finally, the effect on the crack displacements is analysed in Fig. 4.67.

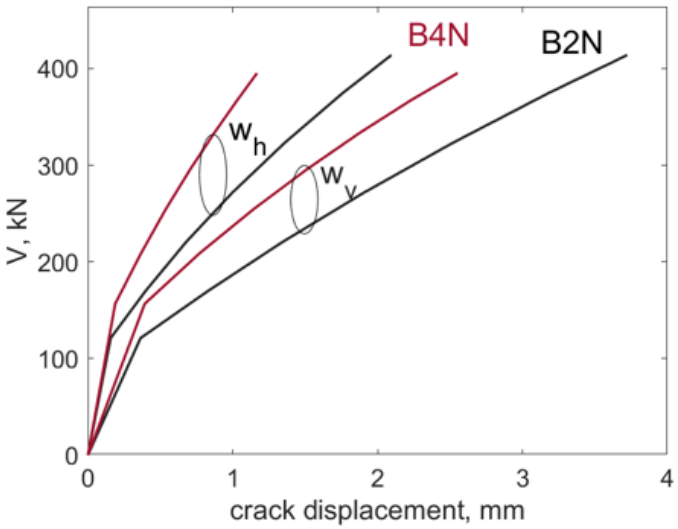

Figure 4.67: Experimental and predicted load-crack displacement for specimens B2N and B4N

The horizontal and vertical displacement are observed to decrease when the reinforcement ratio is increased. As mentioned before, this makes sens, because reinforcement is placed in con-

crete to control the cracking and, therefore, also the crack widths. Thus a higher reinforcement ratio should lead to smaller crack displacements.

Concrete strength in specimens A3N and A4H

The concrete strength of specimen A3N is 41.3 MPa and of specimen A4H is 64.6 MPa. The load-displacement responses are presented in Fig. 4.68.

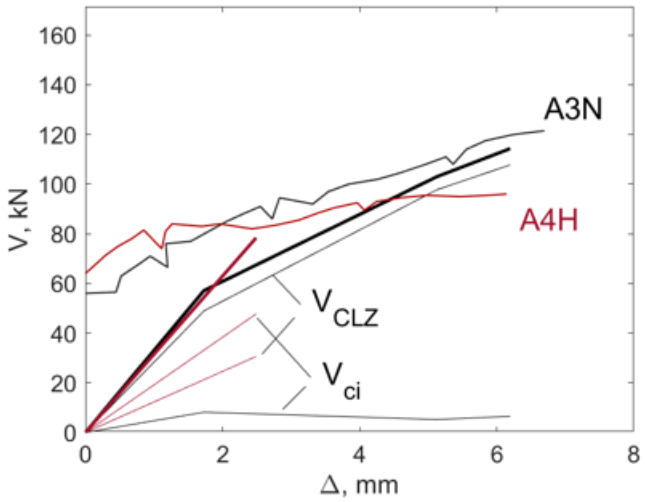

Figure 4.68: Experimental and predicted load-displacement response for specimens A3N and A4H

In both the experimental and predicted results, the increase of the concrete strength lead to an minor decrease of the shear capacity. In the experimental results, the stiffness seems to decrease when the concrete strength was increased. For the predicted results, nothing can be concluded for certain. It is difficult to take a consistent conclusion of this plot due to the early failure of both specimens, but especially specimen A4H.

Next, the strains in the FRP reinforcement are shown in Fig. 4.69.

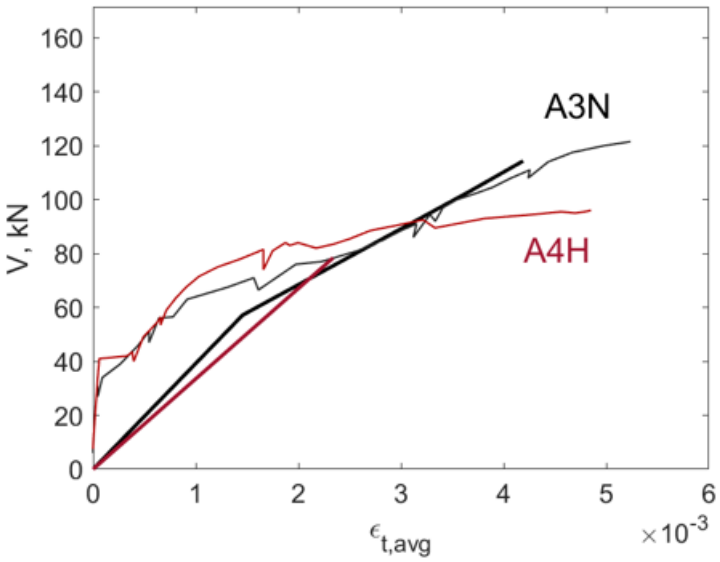

Figure 4.69: Experimental and predicted load-strain responses for specimens A3N and A4H

The strain is slightly decreasing for an increasing concrete strength. Once-more, it is hard to take a conclusion for small specimens.

Finally, the effect on the crack displacements is analysed with Fig. 4.70.

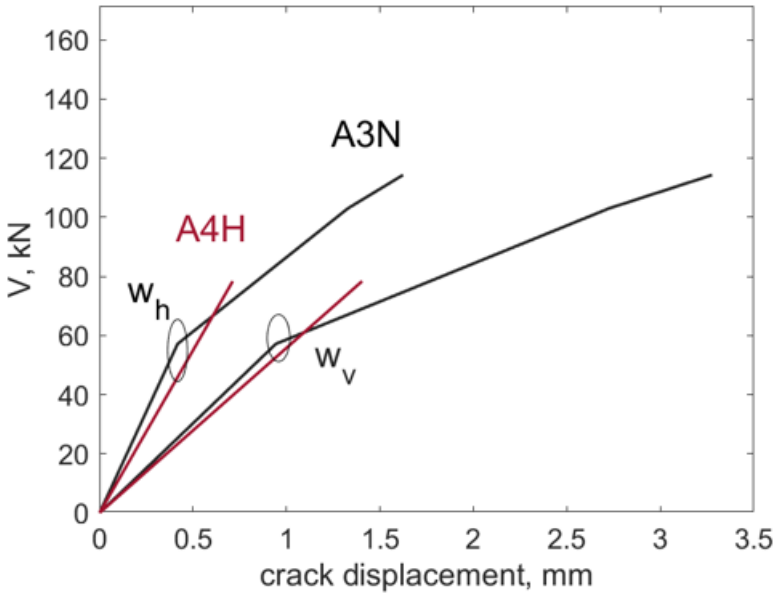

Figure 4.70: Experimental and predicted load-crack displacement for specimens A3N and A4H

The horizontal and vertical crack displacement are observed to decrease when the concrete strength is increased.

Concrete strength in specimens B3N and B6H

The concrete strength of specimen B3N is 41.2 MPa and of specimen B6H is 68.5 MPa. The load-displacement responses are presented in Fig. 4.71.

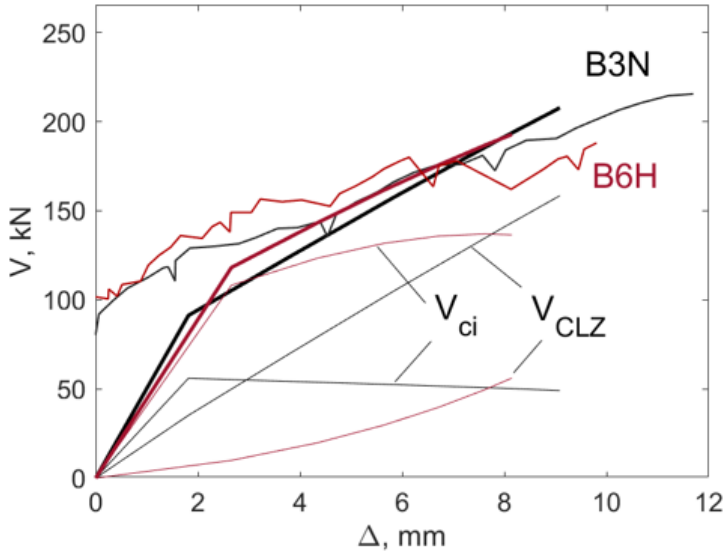

Figure 4.71: Experimental and predicted load-displacement response for specimens B3N and B6H

Once-more, the increase of the concrete strength lead to an minor decrease of the shear capacity in both the experimental and predicted results. Furthermore, the stiffness also tends to decrease slightly when the concrete strength is increased in both the experiment as the prediction. The only clear differences between both specimens are the way they carry shear and their failure mode. Specimen B3N is carrying shear mainly by the CLZ and fails by SIFC, but specimen B6H is carrying shear by mainly aggregate interlock and is failing by cracking of the CLZ. Although both specimens exhibit a different experimental failure mode, the model rightly predicted both of them and predicted accurately the failure load.

Next, the strains in the FRP reinforcement are shown in Fig. 4.72.

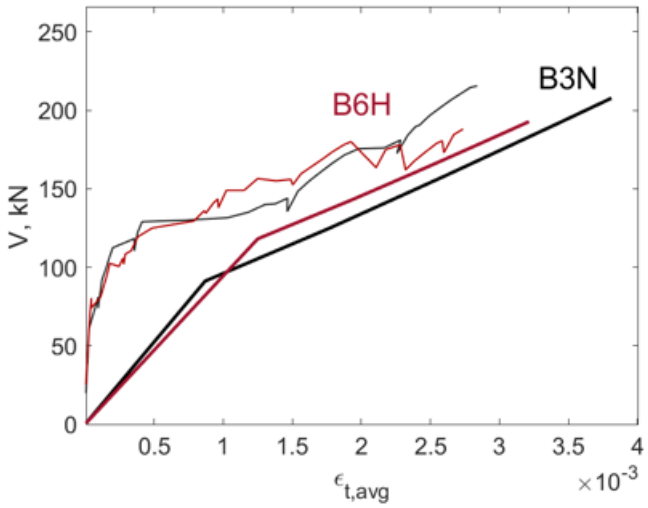

Figure 4.72: Experimental and predicted load-strain responses for specimens B3N and B6H

The experimental maximal strain did not change by increasing the concrete strength. The predicted is slightly decreasing for an increased concrete strength, but this is almost negligible.

Finally, the effect on the crack displacements is analysed in Fig. 4.73.

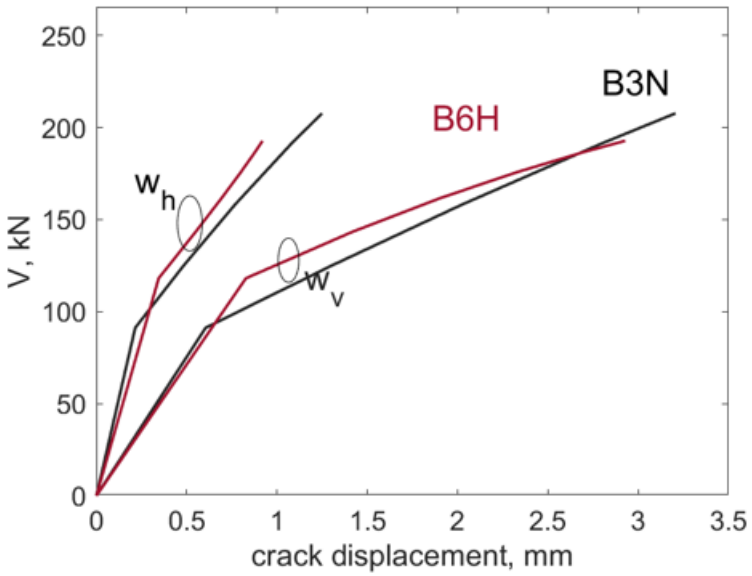

Figure 4.73: Experimental and predicted load-crack displacement for specimens B3N and B6H

There can be seen that the horizontal and vertical displacement is almost not affected by increasing the concrete strength.

Concrete strength in specimens B4N and B5H

The concrete strength of specimen B4N is 40.7 MPa and of specimen B5H is 66.4 MPa. The load-displacement responses are presented in Fig. 4.74.

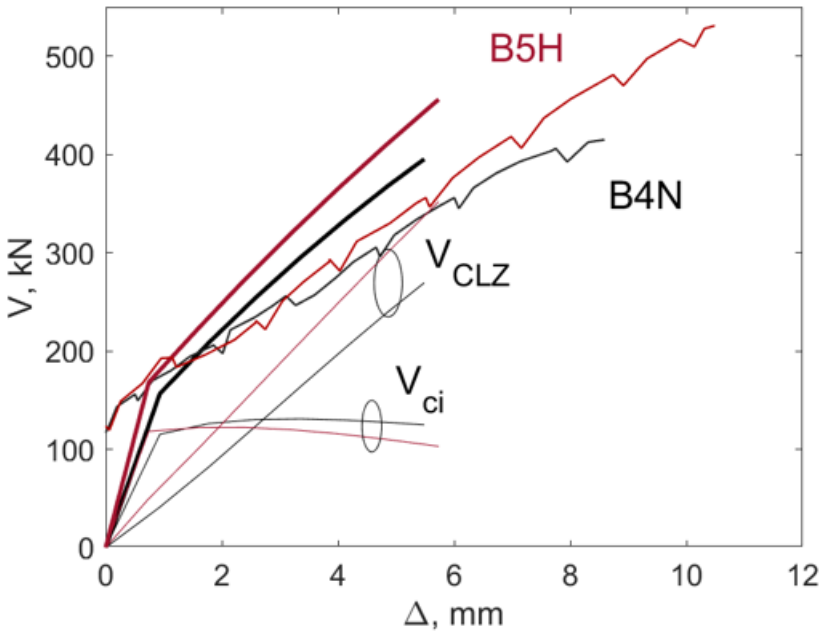

Figure 4.74: Experimental and predicted load-displacement response for specimens B4N and B5H

The predicted behavior of both specimens is in accordance with the experimental one. Both specimens seem to behave in a similar way in terms of strength and stiffness. Although, by increasing the concrete strength both the strength and the stiffness increased slightly.

Next, the strains in the FRP reinforcement are shown in Fig. 4.75.

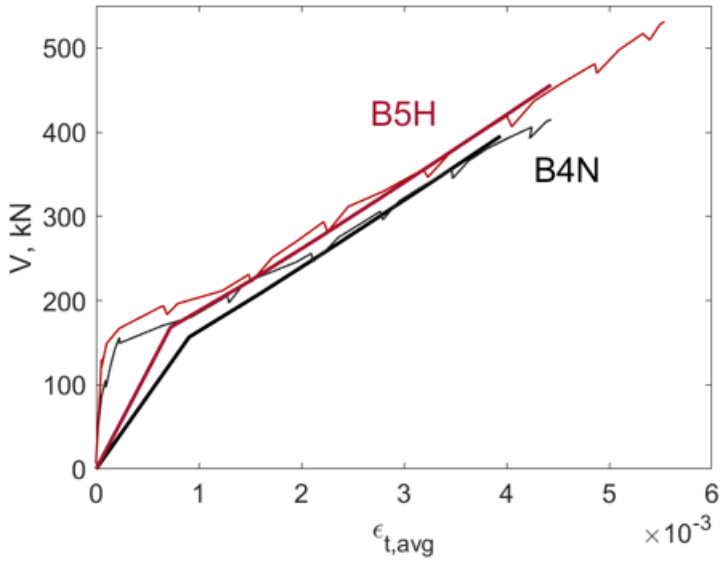

Figure 4.75: Experimental and predicted load-strain responses for specimens B4N and B5H

In both the experimental as the predicted results there can be seen that the strain is increasing for an increased concrete strength. The effect is more explicit in the experimental measurements.

Finally, the effect on the crack displacements is analysed with Fig. 4.76.

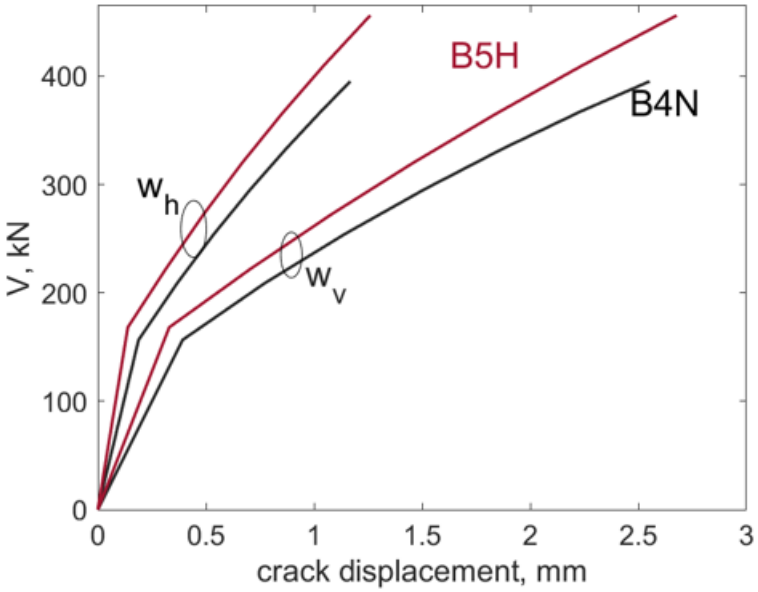

Figure 4.76: Experimental and predicted load-crack displacement for specimens B4N and B5H

Once-more, there can be seen that the horizontal and vertical displacement is not affected by increasing the concrete strength.

4.2 Tests by Farghaly and Benmokrane (2013)

4.2.1 Predictions of global and local shear behavior

G8N6

The experimental and vertical load-displacement response of specimen G8N6 is presented in Fig. 4.77.

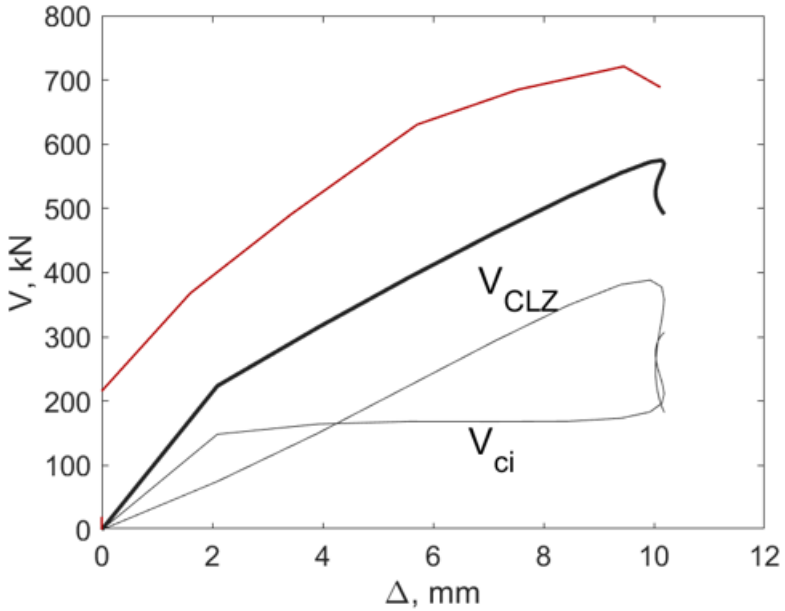

Figure 4.77: Experimental and predicted load-displacement response for specimen G8N6

The predicted failure mode is crushing of the CLZ which corresponds well with the experimental observations. The predicted failure load is equal to 575 kN and the experimental load is equal to 723.5 kN, which means that the capacity is underpredicted by 26%. This may be induced by an underestimation of the CLZ. The predicted deflection of 10 mm is almost equal to the experimental deflection. At failure, two-thirds of the shear capacity is carried by V_{CLZ} and the rest by aggregate interlock.

A first discussion on these results can be reported: specimen G8N6 is the first specimen (compared to what has been discussed here above) where crushing of the CLZ occurred during the test, and, moreover, was predicted by the model. This failure mode, crushing of the CLZ, did not happen in the specimens of Andermatt and Lubell [8], neither was it predicted to happen. This may lead to the question why crushing of the CLZ was not predicted to happen, which can be explained by the following: the a/d ratio of specimen G8N6 is equal to 1.14, which leads to, based on Eq. (12), an predicted crushed-to-compressive depth of almost 90 mm, and, by using Eq. (10), this resulted in a capacity of 944 kN. It is clear that this capacity is much higher than the capacity of 575 kN related to crushing in the CLZ. It may thus be stated that the predicted failure mode is rightly predicted with a lot of margin. The following specimens need to be analysed to be able to conclude if these accurate predictions are obtained in a consistent way or not.

Next, the predicted strain is compared with the experimental strain in the FRP reinforcement in Fig. 4.78.

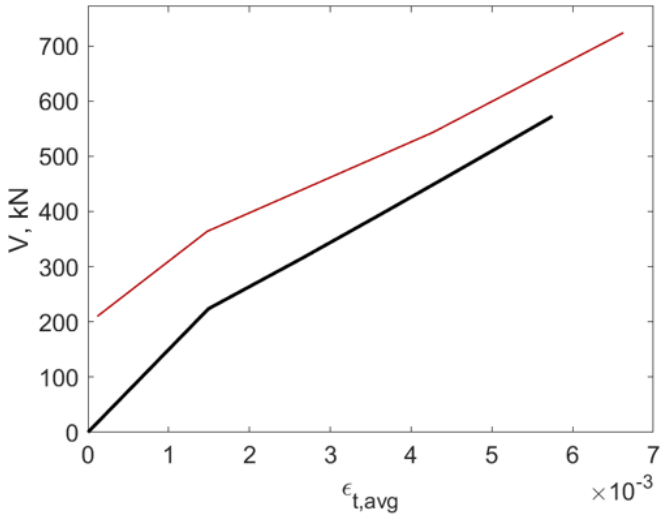

Figure 4.78: Experimental and predicted load-strain response for specimen G8N6

The predicted strain has the same stiffness as the experimental response. Due to the underprediction of the strength, the strain is slightly underpredicted.

Finally, the crack displacement is predicted as shown in Fig. 4.79.

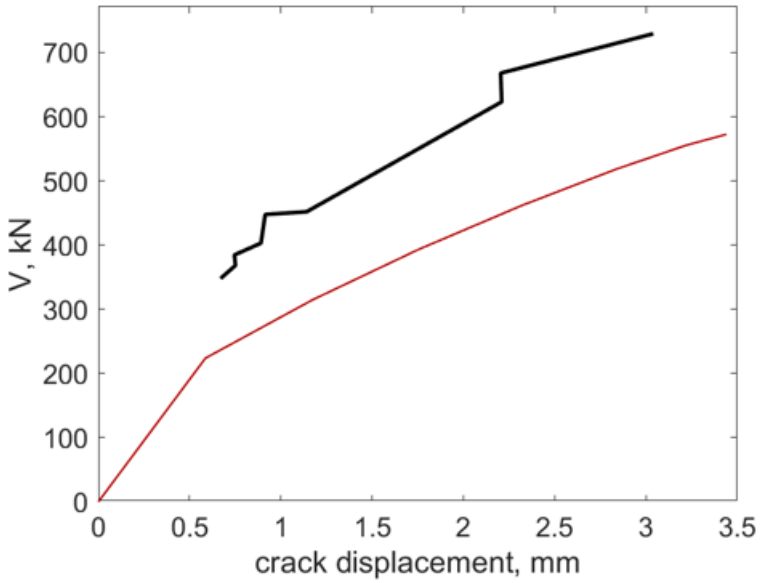

Figure 4.79: Experimental and predicted load-crack displacement response for specimen G8N6

The experimental crack displacement is developing similarly, but at a later loading stage then was predicted. However, the final predicted crack width of 3.5 mm is almost equal to the experimental one.

G8N8

The load-displacement response of specimen G8N8 is presented in Fig. 4.80.

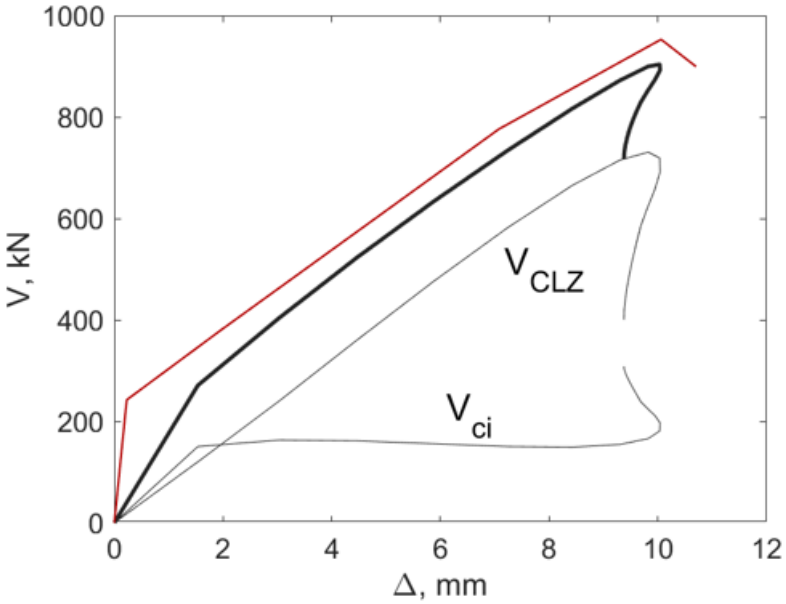

Figure 4.80: Experimental and predicted load-displacement response for specimen G8N8

Once-more, crushing of the CLZ is predicted to happen in specimen G8N8, which corresponds well with the experimental observations. This is in line with the correct prediction for the previous specimen. The predicted failure load for specimen G8N8 is 904 kN, which is close to the experimental load of 953 kN. The deflection is very accurately predicted. At failure, three-fourths of the shear capacity is carried by V_{CLZ} and the rest by aggregate interlock. The presence of the aggregate interlock is possible due to lower crack displacements.

Next, the predicted strain is compared with the experimental strain in Fig. 4.81.

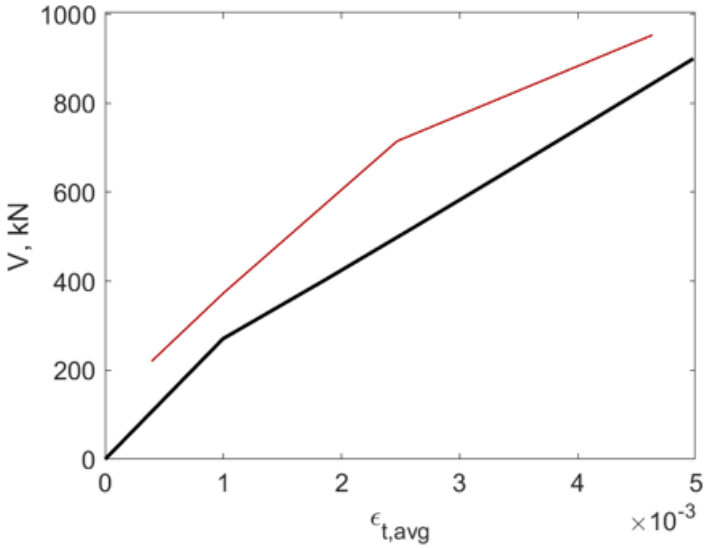

Figure 4.81: Experimental and predicted load-strain response for specimen G8N8

The predicted strain of 5×10^{-3} is almost equal to the experimental strain of 4.5×10^{-3}. Both responses experience the same stiffness.

Finally, the opening of the crack is predicted as shown in Fig. 4.82.

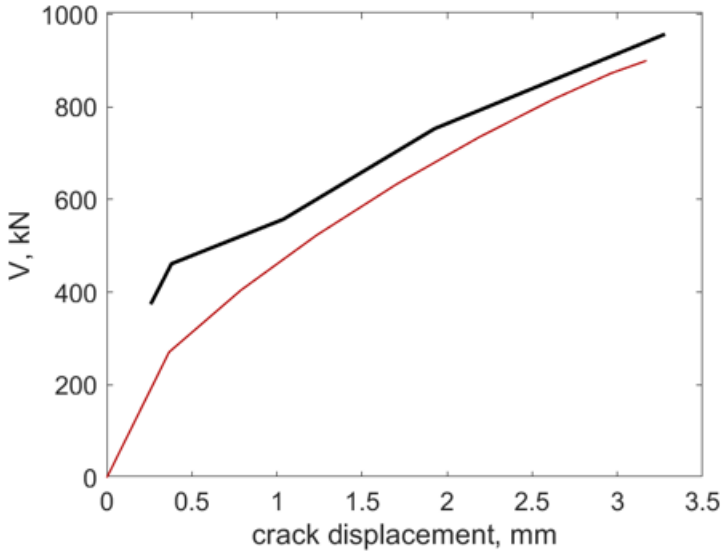

Figure 4.82: Experimental and predicted load-crack displacement response for specimen G8N8

The maximal predicted crack width of 3.5 mm is equal to the experimental one.

C12N3

The load-displacement response of specimen C12N3 is presented in Fig. 4.83.

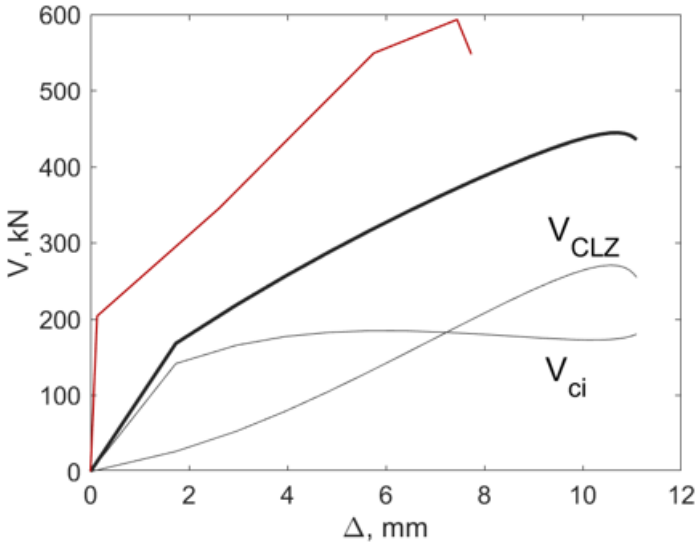

Figure 4.83: Experimental and predicted load-displacement response for specimen C12N3

Although the failure mode, crushing of the CLZ, is well predicted, the corresponding failure load of 445 kN is largely underestimating the experimental capacity of 595.5 kN by 34%. In contrast with the capacity the deflections are overestimated. the specimen behaved stronger and stiffer than predicted. At failure, V_{CLZ} and aggregate interlock are contributing almost equally

to the shear capacity. Therefore, it may be possible that the underestimated part of the failure load is due to an underestimation of the CLZ.

Next, the predicted strain is compared with the experimental strain in Fig. 4.84.

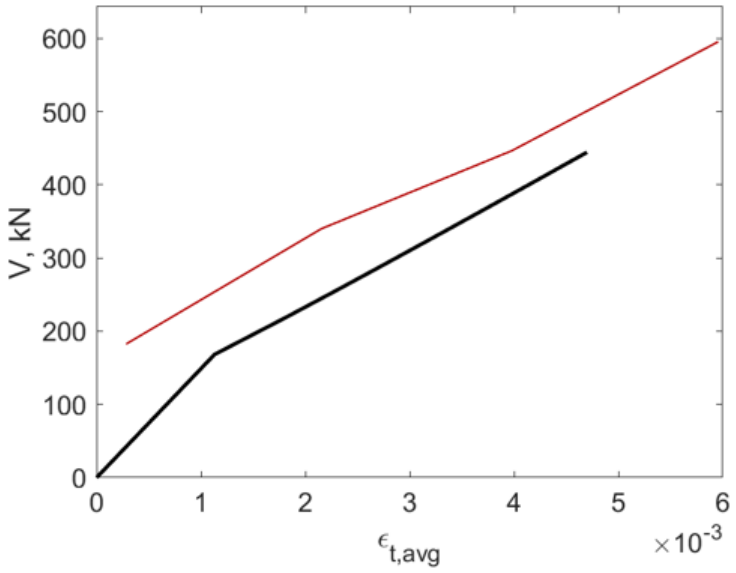

Figure 4.84: Experimental and predicted load-strain response for specimen C12N3

The predicted strain of 5×10^{-3} is smaller than the experimental one of 6×10^{-3}. Both responses experience the same stiffness.

Finally, the opening of the crack is predicted as shown in Fig. 4.85.

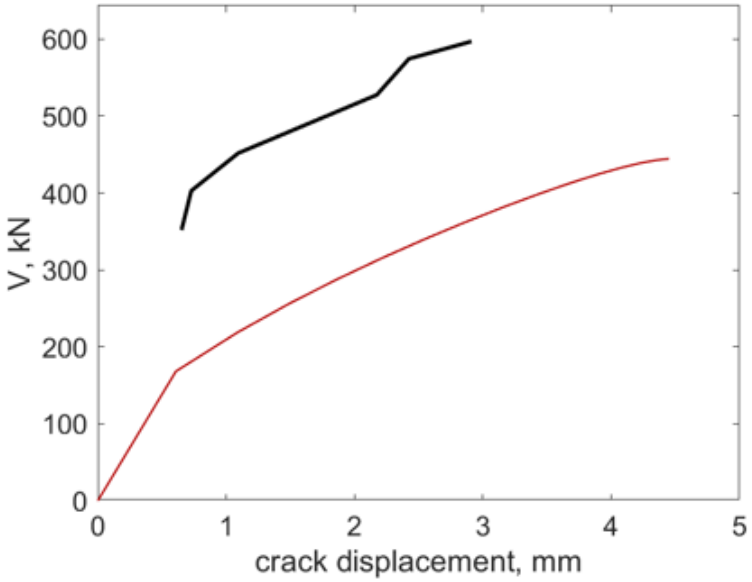

Figure 4.85: Experimental and predicted load-crack displacement response for specimen C12N3

The responses have the same trend, but due to the underestimated failure load, the responses are parallel but shifted. Next, the predicted crack width is higher than the experimental one.

C12N4

The load-displacement response of specimen C12N4 is presented in Fig. 4.86.

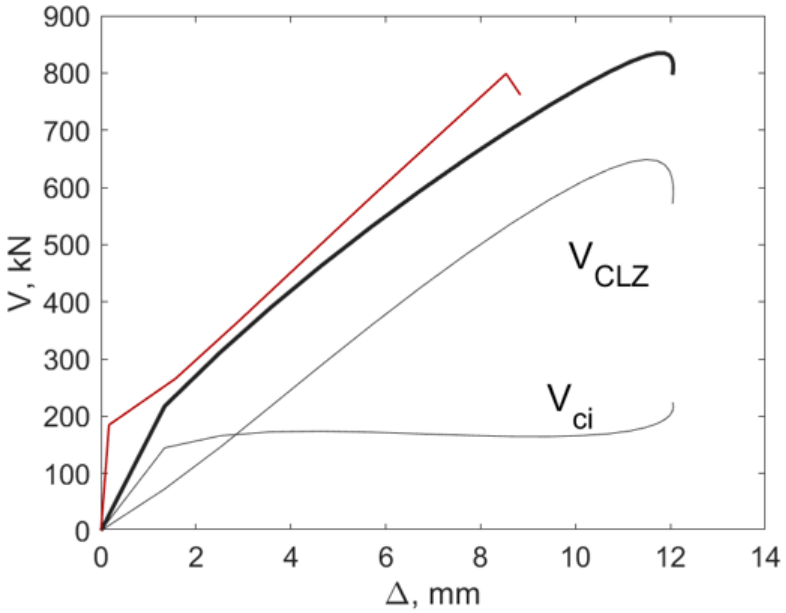

Figure 4.86: Experimental and predicted load-displacement response for specimen C12N4

The predicted failure mode is crushing of the CLZ which corresponds well with the experimental failure mode. The predicted failure load of 834 kN is very close to the experimental failure load of 800.5 kN. The predicted deflection of 12 mm overestimates the experimental one of 8 mm. At failure, one-fifth of the shear capacity was carried by aggregate interlock while the rest was contributed by V_{CLZ}.

It can now be concluded that all specimens of Farghaly and Benmokrane [15] were correctly predicted to fail by crushing of the CLZ. This means that the suggested models to predict the two new observed failure modes in FRP-reinforced deep beams, cooperate adequately together inside the crack-based 2PKT.

Next, the predicted strain is compared with the experimental strain in Fig. 4.87.

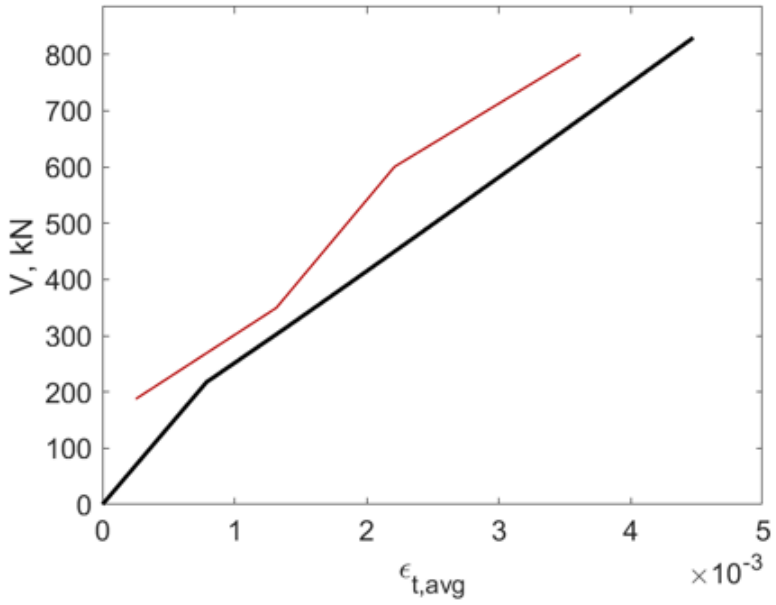

Figure 4.87: Experimental and predicted load-strain response for specimen C12N4

The predicted strain of 4.5×10^{-3} is slightly larger than the experimental one of 3.5×10^{-3}. Both responses experience the same stiffness.

Finally, the opening of the crack is predicted as shown in Fig. 4.88.

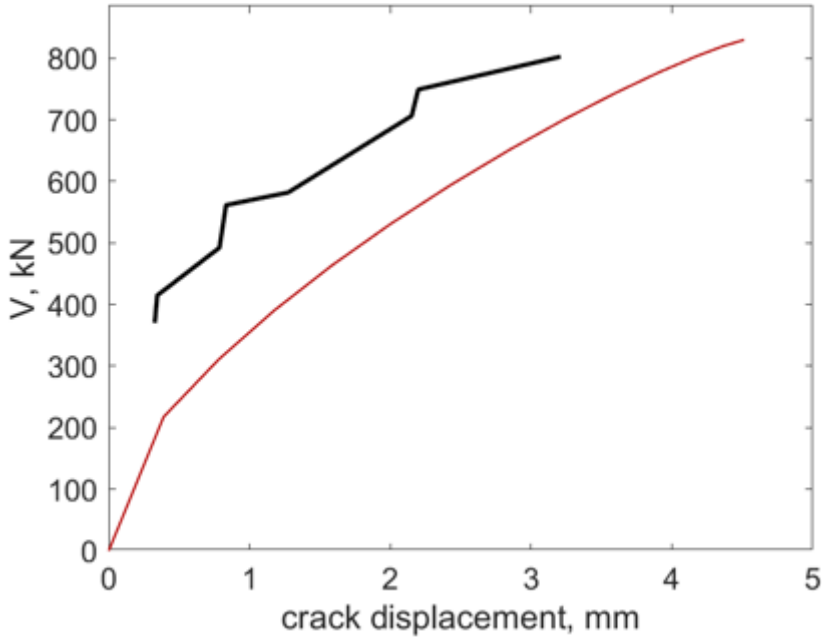

Figure 4.88: Experimental and predicted load-crack displacement response for specimen C12N4

The responses have the same trend, but the predicted crack width is higher than the experimental one.

4.2.2 Effects of test variables

The tests of Farghaly and Benmokrane can be used to analyse the effect of reinforcement ratio. The comparisons are presented in the following sections.

Reinforcement ratio in specimens G8N6 and G8N8

The reinforcement ratio of specimen G8N6 is 0.69% and of specimen G8N8 is 1.24%. The load-displacement responses are presented in Fig. 4.89.

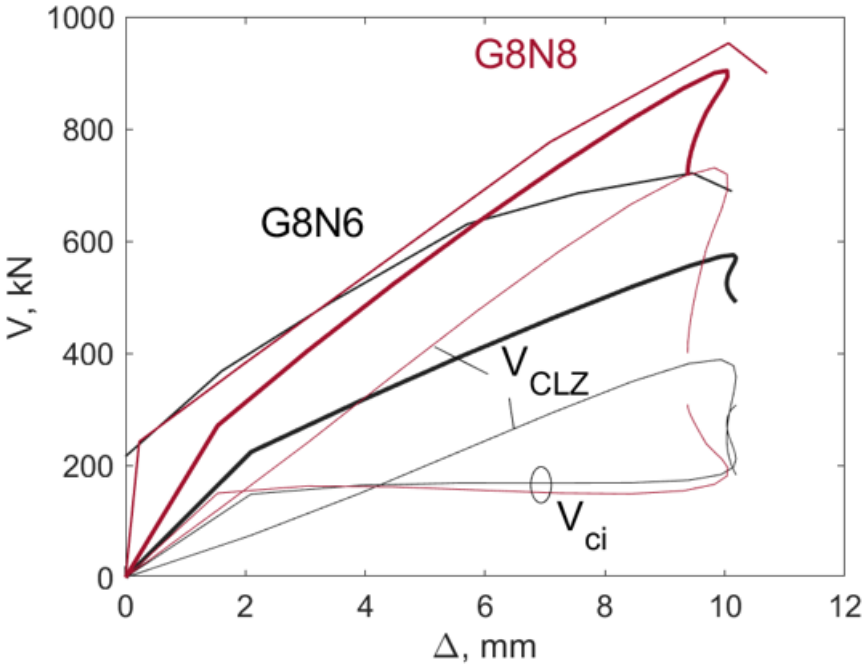

Figure 4.89: Experimental and predicted load-displacement response for specimens G8N6 and G8N8

There can be seen that in the experimental and the predicted results, the increase of the reinforcement ratio lead to an increased shear capacity. Moreover, the stiffness has also increased by increasing the reinforcement ratio. Next, the way shear is carried, is similar in both specimens. The only difference is that in specimen G8N8 the contribution of the CLZ is stiffer and stronger.

Next, the strains in both specimens are compared in Fig. 4.90.

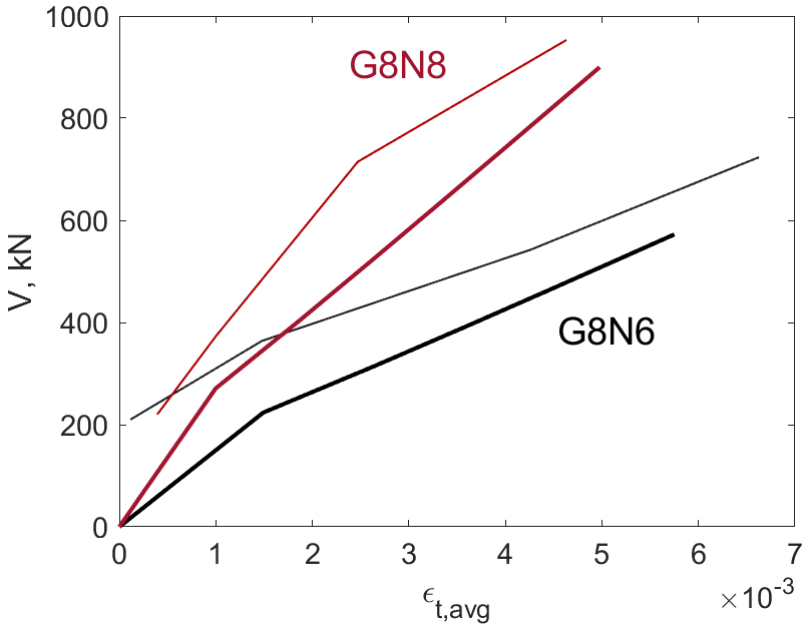

Figure 4.90: Experimental and predicted load-strain responses for specimens G8N6 and G8N8

There can be concluded that the strain in the reinforcement is decreasing when the reinforcement ratio increases. This is in accordance with previously covered discussions. However, this effect is more significantly present in the experimental results than in the predictions.

Finally, the opening of the cracks are compared in Fig. 4.91.

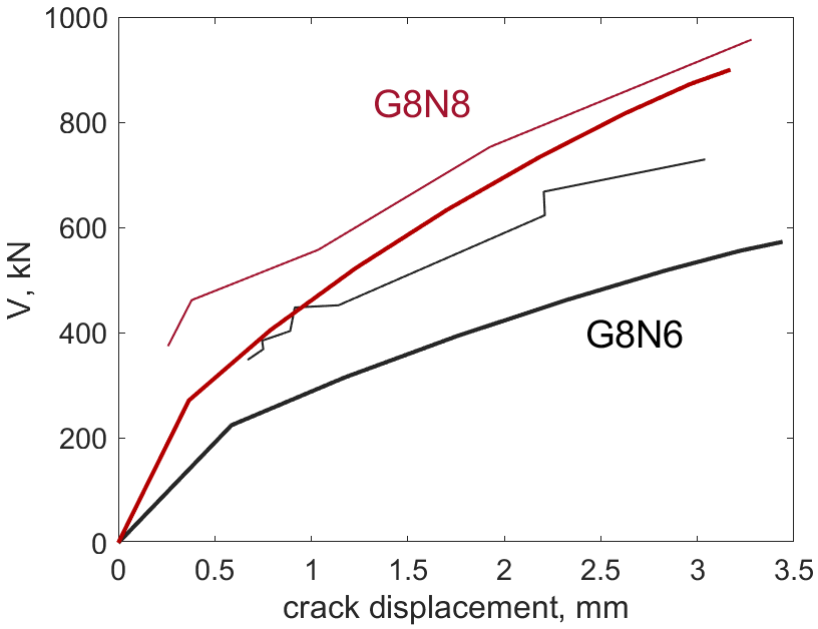

Figure 4.91: Experimental and predicted load-crack displacement response for specimens G8N6 and G8N8

It can be seen that the reinforcement ratio did not affect the final crack width, although the crack widths developed at a later loading stage for the higher reinforced specimen.

Now, another variable to analyse is the effect of the crack geometry. As discussed earlier in this thesis, literature suggested that the crack geometry is affecting the shear capacity of deep beams and, according to the results of Trandafir et al. [12], this effect is accurately taken into account by the crack-based 2PKT. Unfortunately, there are no nominally identical FRP-reinforced deep beams available in our data set.

However, related to this, an interesting hypothetical analysis can be performed on the specimens G8N6 and G8N8, because they have the exact same geometrical properties, but they only differ in terms of reinforcement ratio. There can be investigated how much the shear capacity of a specimen is affected by changing the reinforcement ratio, but for the exact same crack geometry. Although in experimental specimens, the crack geometry is partly influenced by the reinforcement ratio, it is also partly affected by natural randomness of the material properties. Therefore, if the assumption is made that the development of the crack geometry is not influenced by the reinforcement ratio, then it will only be affected by the natural randomness.

If now specimen G8N6 is provided with the reinforcement ratio of specimen G8N8, and, the crack geometry of this modified G8N6 specimen is unchanged, then the model will calculate the difference in capacity due to a change in the reinforcement ratio for this modified specimen. Moreover, a second analysis can be made by comparing the capacity of this modified-G8N6 specimen with the capacity of specimen G8N8. This is justified, because both specimens, the modified specimen and specimen G8N8, have the same reinforcement ratio, but only differ by their developed crack geometry. It must be stated again that this hypothetical analysis is only possible because the assumption is made that the development of the crack geometry is not effected by the reinforcement ratio. The predicted load-displacement response of specimen G8N6, G8N8 and the modified G8N6 are shown in Fig. 4.92.

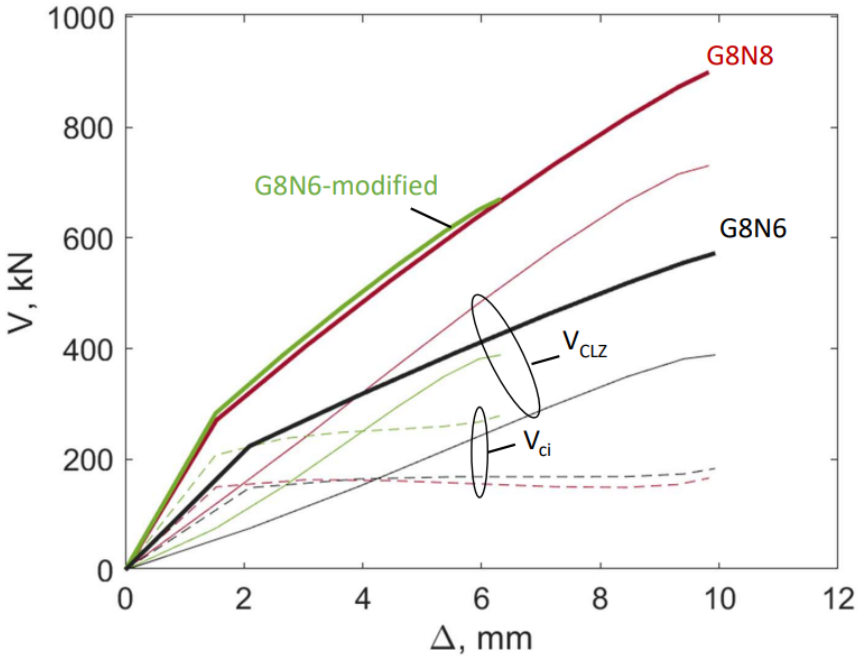

Figure 4.92: Experimental and predicted load-displacement response for specimens G8N6, G8N8 and G8N6-modified

In Fig. 4.92, three different graphs are plotted for each specimens: the shear contribution due to aggregate interlock V_{ci} (dashed line), the shear contribution due to CLZ V_{CLZ} (solid line)

and the load-displacement response (bold line) which is the sum of the two contributions. There can be seen that the original specimen G8N6 has a capacity of 575 kN. Specimen G8N6-modified, which had the same crack geometry as G8N6 but the reinforcement ratio of G8N8, has a capacity of 674 kN. If the behavior of this specimen is further investigated there can be seen that the added shear strength, in comparison to G8N6, is gained completely by V_{ci}. This seems logic, because the increase of reinforcement, leads to smaller crack widths, and, therefore, to larger interlock stresses which results in a larger aggregate interlock shear contribution. Secondly, specimen G8N6-modified can be compared to specimen G8N8. As mentioned earlier, both specimens contain the same reinforcement ratio, but have a different crack geometry. As can be seen in Fig. 4.92, specimen G8N8 has a capacity of 904 kN, compared to 674 kN for G8N6-modified. This difference of 230 kN is, taken into account the assumptions of this hypothetical analysis, due to difference in crack geometry. Moreover, there can be seen that G8N8 has a different contribution of V_{ci} than in G8N6-modified. This shows that the crack geometry is influencing the way the specimen is carrying shear and, thus, influencing the final capacity.

Reinforcement ratio in specimens C12N3 and C12N4

The reinforcement ratio of specimen C12N3 is 0.26% and of specimen C12N4 is 0.46%. The load-displacement responses are presented in Fig. 4.93.

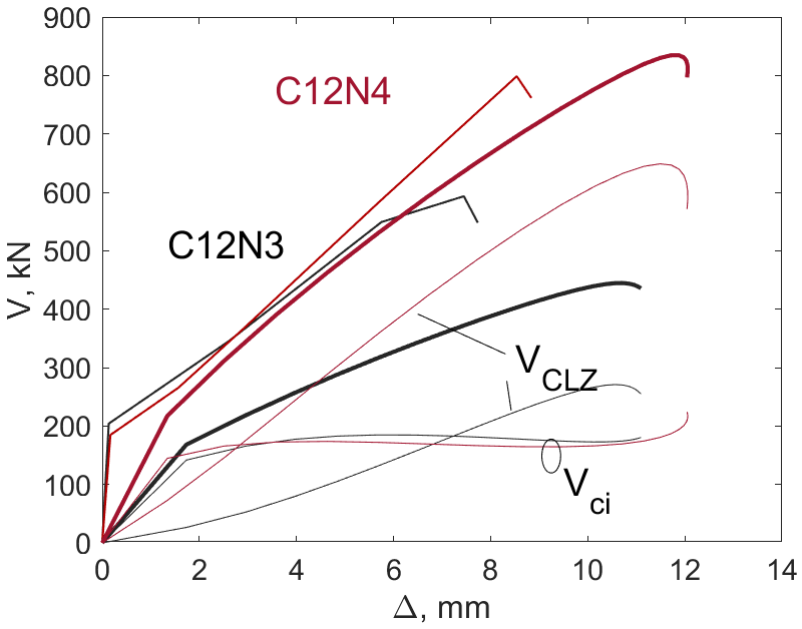

Figure 4.93: Experimental and predicted load-displacement response for specimens C12N3 and C12N4

Both the experimental and the predicted results show an increase of the shear capacity by increasing the reinforcement ratio. Furthermore, the stiffness has also slightly increased by increasing the reinforcement ratio. Once-more, both specimens carry shear in the same way with the only difference that the higher reinforced specimen develops a higher shear contribution by the CLZ. This behavior is similar is previously observed and discussed for specimens G8N6 and G8N8.

Next, the strains in both specimens are compared in Fig. 4.94.

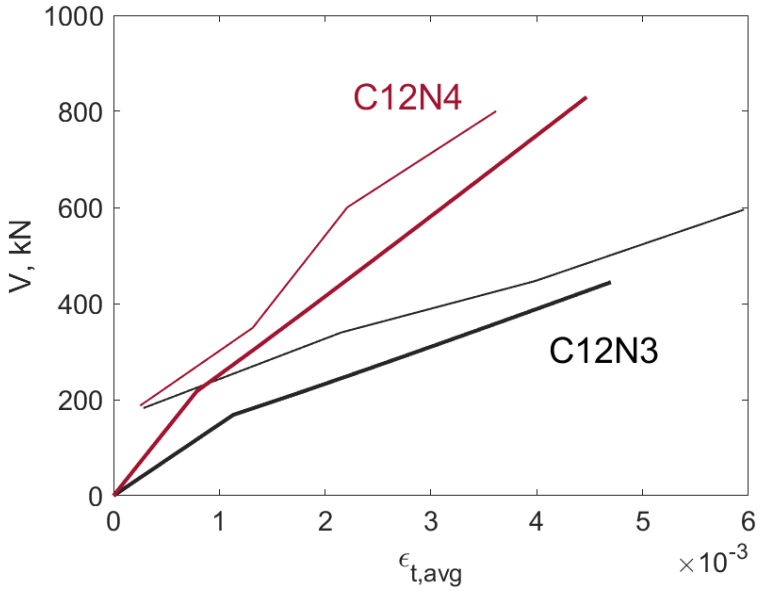

Figure 4.94: Experimental and predicted load-strain responses for specimens C12N3 and C12N4

There can be concluded that due to the increase in reinforcement the strain has decreased, although the difference is bigger in the experiments than was predicted.

Finally, the opening of the cracks are compared in Fig. 4.95.

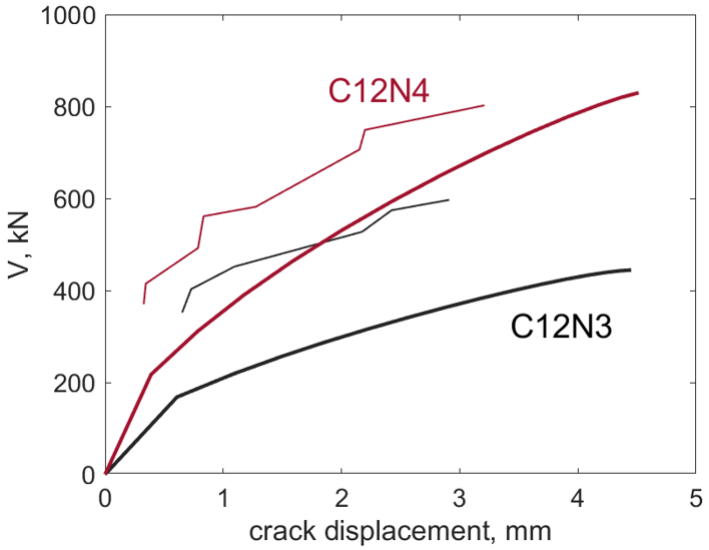

Figure 4.95: Experimental and predicted load-crack displacement responses for specimens C12N3 and C12N4

Both the predicted results and the experimental results show that by changing the reinforcement ratio, the final crack widths did not vary, although the development was delayed.

4.3 Summary of strength predictions

Table 3: Summary of strength predictions for FRP-reinforced deep beam tests

References	Beam name	a/d	b (mm)	d (mm)	ρ_l (%)	E_{FRP} (GPa)	$f_c^{'}$ (MPa)	Observed failure mode	Predicted failure mode	V_{exp} (kN)	V_{pred} (kN)	V_{exp}/V_{pred}
Andermatt and Lubell (2010)	A1N	1.07	310	257	1.49	41.1	40.2	SIFC	SIFC	407.0	355	1.15
	A2N	1.44	310	261	1.47	41.1	45.4	SIFC	SIFC	235.5	234	1.01
	A3N	2.02	310	261	1.47	41.1	41.3	SIFC	SIFC	121.5	114	1.07
	A4H	2.02	310	261	1.47	41.1	64.6	SIFC	SIFC	96.0	78	1.23
	B1N	1.08	300	503	1.70	37.9	40.5	SIFC	SIFC	636.5	677	0.94
	B2N	1.48	300	501	1.71	37.9	39.9	SIFC	SIFC	399.5	414	0.96
	B3N	2.07	300	502	1.71	37.9	41.2	SIFC	SIFC	215.5	208	1.04
	B4N	1.48	300	496	2.13	41.1	40.7	SIFC	CLZ+	415.0	395	1.05
	B5H	1.48	300	497	2.12	41.1	66.4	SIFC	SIFC	531.0	456	1.16
	B6H	2.06	300	505	1.70	37.9	68.5	CLZ+	CLZ+	188.0	194	0.97
	C1N	1.10	301	889	1.58	42.3	51.6	SIFC	SIFC	1134.5	1225	0.93
	C2N	1.49	304	891	1.56	42.3	50.7	SIFC	SIFC	662.0	736	0.90
											Average =	1.03
											COV =	10.5%
Farghaly and Benmokrane (2013)	G8N6	1.14	300	1097	0.69	47.6	49.3	CLZ-	CLZ-	723.5	575	1.26
	G8N8	1.15	300	1088	1.24	51.9	49.3	CLZ-	CLZ-	953.0	904	1.05
	C12N3	1.13	300	1111	0.26	120.0	38.7	CLZ-	CLZ-	595.5	445	1.34
	C12N4	1.13	304	1106	0.46	144.0	38.7	CLZ-	CLZ-	800.5	834	0.96
											Average =	1.15
											COV =	7.5%
											Average all =	1.06
											COV all =	8.5%

Note: SIFC = shear-induced flexural crushing; CLZ+ = cracking of the critical loading zone; CLZ- = crushing of the critial loading zone

5 Conclusions and outlook

5.1 Conclusions

The aim of this study was to develop a kinematics-based model capable of predicting the complete shear behavior of FRP-reinforced deep beams without web reinforcement. The proposed model, extended from the crack-based 2PKT for steel-reinforced deep beams [12], included modelling features for three different failure modes observed in FRP-reinforced deep beams [8, 15]. The first failure mode was similar to the one typically observed in steel-reinforced deep beams: crushing of the critical loading zone (CLZ) due to diagonal compressive stresses. The second failure mode, the shear-induced flexural crushing, is governed by the propagation of the critical shear crack into the pure flexural region, leading to crushing of the concrete under longitudinal compressive stresses. The third failure mode, cracking of the CLZ, is caused by excessive tensile stresses reached at the top face of the beam, near the critical loading zone, which results in cracking from the top side of the beam towards the axis of the beam.

Several remarks could be drawn from this study based on the detailed comparisons done between model predictions and test measurements.

1. For the 16 deep beams considered, the average experimental-to-predicted strength ratio was 1.06 with a coefficient of variation of 8.5%.

2. The crack-based model for FRP-reinforced deep beams predicted for 15 out of 16 specimens the observed failure mode. Only in the case of one specimen, namely B4N, the failure mode was not correctly predicted. However, for specimen B4N the predicted strength of each of the three failure modes was roughly the same. Although the beam was predicted to fail by cracking of the CLZ at 395 kN, the experimental observation suggested a shear-induced flexural failure that corresponds to 415 kN. For the observed failure mode, the crack-based model predicted a shear resistance of 455 kN, which results in a 8% difference from the measured failure load.

3. Only one out of 16 considered tests exhibited a failure due to cracking of the CLZ. Initially, the model predicted a shear-induced flexural failure. However, after an in-depth analysis of the results, it was shown that if the interlocking capacity of the rough crack is not reached, then the member resistance is not governed by shear-induced flexural crushing. Considering the mechanics-based explanation, the initially predicted failure mode is suppressed, and thus the correct failure mode is predicted together with an experimental-to-predicted strength ratio of 0.97.

4. The study highlighted that in FRP-reinforced deep beams without web reinforcement, the shear force is carried mostly by the CLZ. It is worth mentioning that the tests by [8] featured crack widths up to 7 mm that resulted in, most cases, in a reduced contributions of the predicted aggregate interlock to the peak shear resistance. In contrast, the tests by [15] featured crack widths up to 3.5 mm that resulted in interlocking contribution of up to 33% at failure.

5. The crack-based model accurately predicted the average strain in the FRP reinforcement, as well as the shear span deflections and the stiffness after diagonal cracking. The strain in FRP reinforcement increased in some cases up to 1% which is roughly 5 times larger than the yield strain of conventional steel. The relative horizontal crack displacements are accurately predicted, while the relative vertical crack displacements are most slightly underestimated. On average, the predicted horizontal-to-vertical crack displacement ratio is between 2 and 4.

6. Regarding the effects of variables on FRP-reinforced deep beams, a increase of the shear capacity was observed consistently when the a/d ratio was decreased. This behavior, observed in experiments and in predictions, is in accordance with the trend shown in Fig. 2.1.

7. The tests of Farghaly and Benmokrane [15] demonstrated that the type of reinforcement has no consequence on the capacity of a deep beam, as long as the axial stiffness is kept the same. Although this condition was fulfilled in the tests by [15], a difference in capacity was observed, but this may be a consequence of the varying concrete compressive strength.

5.2 Recommendations for future work

This study started from a model developed for steel-reinforced for deep beams and extended this to be useful for the prediction of the behavior of FRP-reinforced deep beams without web reinforcement. Several interesting topics, worthy of further research, came along during this study:

- The bond properties of FRP reinforcement were evaluated based on limited data available in the literature. More research is needed to gain a better understanding on the behavior of FRP reinforcement in deep beams and to assess potential modifications required to the proposed kinematic framework.
- The model is currently developed for FRP-reinforced deep beams without web reinforcement. However, the crack-based 2PKT for steel-reinforced deep beams already contained a shear mechanism for stirrups. Therefore, the current model can be extended to be able to predict the behavior of FRP-reinforced deep beams with web reinforcement.
- The shear contribution by aggregate interlock in the studied beams varied in magnitude from zero to almost half of the total shear capacity. A more in-depth study on aggregate interlock in FRP-reinforced deep beams is proposed.
- This work made use of a data set of sixteen specimens. The developed model may be validated on a larger database.

Nomenclature

Capital Latin letters

$A_{c,eff}$	Concrete area around the reinforcing bars responsible for tension stiffening effect
A_{FRP}	Area of longitudinal FRP bars on the flexural tension side
CDM	Contact density model
CLZ	Critical loading zone
COV	Coefficient of variation
E_c	Modulus of elasticity of concrete
E_{FRP}	Modulus of elasticity of FRP
F_c	Compression force in concrete in SIFC
I	Moment of inertia
I_{cr}	Moment of inertia of cracked section
I_{FRP}	Moment of inertia of longitudinal FRP bars on the flexural tension side
K_d	Stiffness of dowel
M_d	Moment induced by dowel action
M_{SIFC}	Resisting moment due to shear-induced flexural crushing
R	Resultant force
$SIFC$	Shear-induced flexural crushing
T	Tensile force in bottom longitudinal FRP reinforcement
V	Shear force and lateral load
V/P	Reaction force to load ratio
V_{ci}	Shear resisted by aggregate interlock
V_{CLZ}	Shear resisted by critical loading zone
V_d	Shear resisted by dowel action
V_{exp}	Experimental shear strength
V_{pred}	Predicted shear strength
V_{SIFC}	Shear strength due to shear-induced flexural crushing

Small Latin letters

a	Shear span from center of load to center of support
a/d	Shear span-to-depth ratio
a_g	Maximum size of coarse aggregates
b	Width of cross section
c	Depth of concrete compression zone
d	Effective depth of section
d_b	Diameter of bottom longitudinal bars
d_{CLZ}	Depth of the critical loading zone
d_{cs}	Depth of crushed section
e	Eccentricity of applied force
f_{avg}	Average diagonal compressive stress
$f_c^{'}$	Concrete cylinder strength
$f_{c,con}$	Compressive yield strength of CDM springs

$f_{c,eff}$	Concrete effective compressive strength
f_{ct}	Concrete tensile strength
$f_{FRP,u}$	Ultimate strength of FRP longitudinal reinforcement
h	Total depth of section
k	Crack shape factor
l_0	Length of heavily cracked zone at the bottom of the critical diagonal crack
l_{an}	Anchorage length of the bottom reinforcement
l_{b1}	Width of loading plate parallel to longitudinal axis of member
l_{b1e}	Effective width of loading plate parallel to longitudinal axis of member
l_{b2}	Width off bearing plate parallel to longitudinal axis of member
l_{CLZ}	Horizontal length of CLZ
l_f	Length between center of loading plates
l_k	Length of bottom FRP reinforcement whose elongation contributes to the width of the cracks
l_{tr}	Transfer length
n_b	Number of longitudinal bars
n_{ci}	Aggregate interlock normal stress
s_{cr}	Distance between radial cracks along the bottom edge of the member
s_i	Crack slip of crack segment i
v_{ci}	Aggregate interlock shear stress
w_h	Horizontal displacement in crack (relative)
w_i	Crack width of crack segment i
w_v	Vertical displacement in crack (relative)
x_i	Orthogonal horizontal coordinate of crack segment i
y_i	Orthogonal vertical coordinate of crack segment i

Capital Greek letters

Δ	Mid span deflection of beam
Δ_c	Transverse displacement of CLZ
Δ_{cx}	Horizontal displacement of CLZ
$\Delta_{exp,mod}$	Deflection at shear span
Δ_{exp}	Deflection at midspan
Ω_0	Area under stress-strain diagram of concrete

Small Greek letters

α	Angle of the diagonal of the shear span
α_1	Angle of critical diagonal crack
α_{CLZ}	Angle of the crack in the CLZ
$\alpha_{cr,i}$	Angle of a crack segment i
$\varepsilon_{t,avg}$	Average strain along bottom longitudinal reinforcement
η_{fc}	Brittleness factor for concrete
ρ_l	Ratio of bottom longitudinal reinforcement
σ_{con}	Contact stress in CDM

σ_{top}	Stress in top fiber of CLZ
σ_{bottom}	Stress in bottom fiber of CLZ
τ_{FRP}	Bond stress of FRP reinforcement
τ_{steel}	Bond stress of steel reinforcement
ϕ	Curvature of pure flexural region

Abbreviations

$2PKT$	Two-parameter kinematic theory
ACI	American Concrete Institute
$CFRP$	Carbon fiber-reinforced polymers
CLZ	Critical loading zone
CSA	Canadian Standards Association
DOF	Degree of freedom
FEM	Finite elements model
FRP	Fiber-reinforced polymers
$GFRP$	Glass fiber-reinforced polymers
HSC	High strength concrete
NSC	Normal strength concrete
STM	Strut-and-tie model

References

[1] Mihaylov, B. I.; Bentz, E. C.; and Collins, M. P., "Behavior of Large Deep Beams Subjected to Monotonic and Reversed Cyclic Shear," ACI Structural Journal, V. 107, No. 6, Nov.-Dec. 2010, pp. 726–734 (pages 1–3, 10).

[2] Hooke, R., "Lectures de Potentia Restitutiva (Spring Explaining the Power of Springing Bodies)," printed for John Martyn Printer to The Royal Society, at the Bell in St. Paul's Church-Yard, 1678, p. 24 (page 1).

[3] Gurley, C. R., "Concrete Plasticity in Structural Design Practice," The Morley Symposium on Concrete Plasticity and its Application. Cambridge, UK, July 2007, Magazine of Concrete Research, Vol. 60, No. 8, October 2008, pp. 623–632 (page 1).

[4] ACI 440.1R-06, "Guide for the design and construction of concrete reinforced with FRP bars," American Concrete Institute, Farmington Hills, MI, USA, 2006 (pages 1, 6, 7).

[5] CAN/CSA-S806-02, "Design and construction of building components with fibre-reinforced polymers," Canadian Standards Association, Mississauga, ON, Canada, 2002 (pages 1, 7).

[6] Leonhardt, F.; and Walther, R., "The Stuttgart Shear Tests, 1961; Contributions to the Treatment of the Problems of Shear in Reinforced Concrete Construction," Cement and Concrete Association, London, UK, 1964, p. 134 (page 2).

[7] Rogowsky, D. M.; MacGregor, J. G.; and Ong, S. Y., "Tests of Reinforced Concrete Deep Beams," ACI Journal Proceedings, V. 83, No. 4, July-Aug. 1986, pp. 614–623 (page 2).

[8] Andermatt, M. F.; and Lubell, A. S., "Concrete deep beams reinforced with internal FRP," MSc thesis, Dept. of Civil Environmental Engineering, University of Alberta, Edmonton, Alberta, Canada, 2010 (pages 2, 9, 11, 12, 15, 17, 18, 28, 62, 79, 92).

[9] Andermatt, M. F.; and Lubell, A. S., "Behavior of concrete deep beams reinforced with internal fiber-reinforced polymer—Experimental study," ACI Struct. J., 110(4), 2013, pp. 585–594 (pages 2, 8, 20, 24).

[10] Collins, M. P.; Bentz, E. C.; Quach, P. T.; and Proestos, G. T., "The Challenge of Predicting the Shear Strength of Very Thick Slabs," Concrete International, V.37, No.11, 2015, pp. 29–37 (page 3).

[11] Mihaylov, B. I.; Bentz, E. C.; and Collins, M. P., "Two-Parameter Kinematic Theory for Shear Behavior of Deep Beams," ACI Structural Journal, V. 110, No. 3, May-June 2013, pp. 447–456 (pages 3, 16, 17, 21, 22, 32).

[12] Trandafir, A. N.; Palipana, D. K.; Proestos, G. T.; and Mihaylov, B. I., "Framework for Crack-Based Assessment of existing Lightly Reinforced Concrete Deep Members," ACI Structural Journal, V. 119, No. 1, January, 2022, pp. 255–266 (pages 3, 15, 18–20, 22–25, 88, 92).

[13] Collins, M. P.; and Mitchell, D., "Prestressed Concrete Structures," Response Publications, 1997 (page 5).

[14] Liu, J., "Kinematics-Based Modelling of Deep Transfer Girders in Reinforced Concrete Frame Structures," Ph.D. thesis, Dept. of Applied Sciences, Université de Liège, Liège, Liège, Belgium, 2019 (page 5).

[15] Farghaly, A.; and Benmokrane, B., "Shear behavior of FRP-reinforced concrete deep beams without web reinforcement," J. Compo. Const., Vol. 17, No. 6, December 2013 (pages 6, 10, 11, 15, 17, 18, 20, 28, 31, 37, 84, 92, 93).

[16] Meier, U., "External Strengthening and Rehabilitation: Where from–Where to?," FRP International, Volume 1, Issue 2, August 2004, pp. 2–5 (page 6).

[17] Balafas, I.; and Burgoyne, C., "Initial cost considerations on the use of fibre reinforced plastics in reinforced concrete structures," Research leading to the development on design guidelines for the use of FRP in concrete structures, 2nd ConFibreCrete Young Researchers' Seminar, Corfu, Greece, June 2002 (pages 6, 7).

[18] ISIS Canada Research Network, "Reinforcing Concrete Structures with Fibre Reinforced Polymers-Design Manual 3, Version 2". ISIS Canada Corporation, Winnipeg, Manitoba, Canada, 2007, pp. 726–734 (page 7).

[19] El-Sayed, A.; El-Salakawy, E. F.; and Benmokrane, B., "Shear strength of FRP-reinforced concrete deep beams without web reinforcement," Can. J. Civ. Eng., 39(5), 2012, pp. 546–555 (pages 7, 24).

[20] Baena, M.; Torres, L.; Turon, A.; and Barris, C., "Experimental study of bond behaviour between concrete and FRP bars using a pull-out test," Composites Part B: Engineering,Volume 40, Issue 8, 2009, pp. 784–797 (pages 7, 8, 24).

[21] Kuchma, D. A.; and Tjihin, T. N., "Designing Discontinuity Regions in Structural Concrete with Computer-Based Strut-and-Tie Methodology," Transportation Research Record 1814, Paper No. 02-3000, 2002 (page 14).

[22] CSA A23.3-04, "Design of Concrete Structures," Canadian Standards Association, Mississauga, ON, Canada, 2004 (page 15).

[23] Mihaylov, B. I., "Two-Parameter Kinematic Approach for Shear Strength of Deep Concrete Beams with Internal FRP Reinforcement," J. Compos. Constr., 21(2):04016094, 2017 (pages 17, 18, 27).

[24] Enem, J. I.; Ezeh, J.C.; Mbagiorgu, M.S.W.; and Onwuka, D.O., "Analysis of deep beam using Finite Element Method," Int. J. Appl. Sci. ENg. REs., 1, 2012, pp. 348–356 (page 18).

[25] Metwally, I. M., "Three-dimensional nonlinear finite element analysis of concrete deep beam reinforced with GFRP bars," HBRC Journal,13, 2015, pp. 25–38 (page 18).

[26] Li, B.; Maekawa, K.; and Okamura, H., "Contact Density Model for Stress Transfer Across Cracks in Concrete," Journal of Faculty of Engineering, The University of Tokyo, V. 40, 1989, pp. 9–52 (pages 20, 23, 25).

[27] Mihaylov, B. I., "Five-spring model for complete shear behaviour of deep beams," FIB Struct. Concr., 16(1), 2015, pp. 71–83 (pages 20, 21, 27, 35).

[28] CEB-FIP Model Code 1990, "Design Code," Thomas Telford, London, 1993, p. 437 (page 25).

[29] European Commitee for Standardization (CEN), "Design of concrete structures—Part 1-1: General rules and rules for buildings." Eurocode 2, Brussels, Belgium, 2005 (pages 27, 34).

[30] Kotsovos, M. D., "Behavior of Reinforced Concrete Beams with a Shear Span to Depth Ratio Between 1.0 and 2.5," ACI Structural Journal, No. 81-27, May-June 1984, pp. 279–286 (page 28).

[31] Salamy, M. R.; Kobayashi, H.; and Unjoh, Sh., "Experimental and analytical study on RC deep beams". Asian journal of civil engineering (building and housing), Vol. 6, No. 5, 2005, pp. 487–499 (page 29).

[32] Moccia, F.; Ruiz, L. F.; and Muttoni, A., "Efficiency Factors for Plastic Design in Concrete: Influence of Brittleness in Compression," 10.1007/978-3-319-59471-2$_1$43, 2018 (page 30).

[33] Cavagnis, F.; Fernandez Ruiz, M.; and Muttoni, A., "A mechanical model for failures in shear of members without transverse reinforcement based on development of a critical shear crack," Engineering structures, Vol. 157, 2018, pp. 300–315 (pages 32, 34).

[34] Fernandez Ruiz, M.; Muttoni, A.; Sagaseta, J., "Shear strength of concrete members without transverse reinforcement: A mechanical approach to consistently account for size and strain effects," Engineering structures, Vol. 99, 2015, pp. 360–372 (page 32).

[35] Fédération Internationale du Béton (fib), "fib Model Code for Concrete Structures 2010," Ernst&Sohn, 2013, p. 434 (page 34).